UNIVERSITÀ DEGLI STUDI DI PADOVA

UNIVERSITA' DEGLI STUDI DI PADOVA

Dipartimento di Ingegneria Industriale DII

Corso di Laurea Magistrale in Materials Engineering

Hot compression behavior of LPBF-fabricated Ti-6Al-4V titanium alloy

Relatore: Prof.ssa Stefania Bruschi

Laureando: Md Jubaer Hossain

Matricola: 2071477

Anno Accademico 2024/2025

Abstract

Titanium and its alloys are highly renowned for their applications in precision industries(i.e., Aerospace industry, Biomedical industry) due to their excellent mechanical properties and highly corrosion-resistant nature. The demand for their application is increasing day by day, from defense industries to medical industries. Manufacturing complex parts and components is somewhat challenging for the manufacturing industry, particularly when the material is expensive, such as titanium and its alloys. Recently, researchers have been focusing on hybrid additive manufacturing to manufacture precision components with near-net shapes, which involves additive manufacturing and hot working of metals. A sophisticated method that adds glory to the manufacturing engineering. Numerous analytical, numerical, and experimental studies have already discussed the potential of this new method and confirmed its sustainability in the long run. However, due to their precision application, several validations must be done before this process gets established in the manufacturing industry, particularly with alloys like Ti-6Al-4V.

This study investigates the hot compression behavior of Ti-6Al-4V titanium alloy fabricated by laser powder bed fusion (LPBF). Cylindrical specimens were produced in two distinct build directions and subjected to stress-relief heat treatment at 950 °C for 30 minutes, followed by furnace cooling. Hot compression tests were conducted at 800 °C, 900 °C, and 950 °C under strain rates of 0.1 s^{-1}, 1 s^{-1}, and 10 s^{-1}. Flow stress curves were analyzed to assess deformation behavior under varying thermal and strain rate conditions. Post-deformation microstructures were examined to understand the influence of temperature, strain rate, and build direction on dynamic softening mechanisms. The findings provide insights into the hot workability and microstructural evolution of LPBF-fabricated Ti-6Al-4V, informing process optimization for additive manufacturing applications.

Keywords

LPBF, Hot compression, Titanium alloy, Hybrid Additive Manufacturing

Sommario

Il titanio e le sue leghe sono ampiamente riconosciuti per le loro applicazioni in settori ad alta precisione (ad esempio, l'industria aerospaziale e quella biomedica) grazie alle eccellenti proprietà meccaniche e all'elevata resistenza alla corrosione. La domanda per il loro impiego è in costante crescita, spaziando dall'industria della difesa a quella medica. La produzione di componenti complessi rappresenta una sfida per l'industria manifatturiera, soprattutto quando si utilizzano materiali costosi come il titanio e le sue leghe. Recentemente, l'attenzione della ricerca si è concentrata sulla manifattura additiva ibrida per la realizzazione di componenti di precisione con geometrie prossime alla forma finale, combinando tecniche di produzione additiva e lavorazioni a caldo dei metalli. Si tratta di un metodo sofisticato che arricchisce il campo dell'ingegneria della produzione. Numerosi studi analitici, numerici e sperimentali hanno già evidenziato il potenziale di questo nuovo approccio, confermandone la sostenibilità a lungo termine. Tuttavia, data la natura di precisione delle applicazioni, sono necessarie ulteriori validazioni prima che il processo possa essere pienamente adottato nell'industria manifatturiera, in particolare per leghe come la Ti-6Al-4V.

Questo studio analizza il comportamento alla compressione a caldo della lega di titanio Ti-6Al-4V fabbricata mediante fusione laser a letto di polvere (Laser Powder Bed Fusion, LPBF). Campioni cilindrici sono stati prodotti in due diverse direzioni di costruzione e sottoposti a trattamento termico di distensione a 950 °C per 30 minuti, seguito da raffreddamento in forno. I test di compressione a caldo sono stati condotti a 800 °C, 900 °C e 950 °C con velocità di deformazione di 0,1 s^{-1}, 1 s^{-1} e 10 s^{-1}. Le curve di tensione-deformazione sono state analizzate per valutare il comportamento alla deformazione in funzione delle condizioni termiche e delle velocità di deformazione. Le microstrutture post-deformazione sono state esaminate per comprendere l'influenza della temperatura, della velocità di deformazione e della direzione di costruzione sui meccanismi di ammorbidimento dinamico. I risultati forniscono indicazioni utili sulla lavorabilità a caldo e sull'evoluzione microstrutturale della lega Ti-6Al-4V prodotta tramite LPBF, contribuendo all'ottimizzazione dei processi per applicazioni di manifattura additiva.

Acknowledgement

I thank Professor Bruschi for allowing me to complete this thesis. From the topic selection of the thesis, the arrangement of the research progress, to the writing of the thesis, and the completion of the engineering calculations, her instructive teachings are embodied. In the study and life of the university, a little bit of knowledge is accumulated, and every process of university study is inseparable from the process of writing this graduation thesis. From the study of theoretical knowledge to the cultivation of innovative consciousness, and finally, to the application of practical activities, a university study has never been achieved overnight. It was a memorable journey for my entire life.

A special thanks to Edoardo, because without his help, without his constant support, things could've been more worse. Gratitude to the guys from the laboratory Te.Si. Andrea and Flavia were always helpful around the lab, helped me with their availability. I thank my friends and all those who put up with me in these last months.

Last but not least, I would have to put them first otherwise: I thank my parents, because all of this was possible due to their constant support during the entire academic journey, and I will never be able to stop thanking them. My heartfelt thanks to Lamyea, the love of my life, who has been there for me as a strong point on which I can always rely and all the words in the world would not be enough to thank her for everything she does for me.

Contents

Chapter 1: Introduction

1.1 Ti-6Al-4V Titanium Alloy and Its Applications

Titanium alloy Ti-6Al-4V (also known as Ti-64 or Grade 5) is a two-phase α+β alloy containing approximately 6% aluminum and 4% vanadium by weight. First developed in 1954, Ti-6Al-4V quickly became the most important α+β titanium alloy due to its excellent combination of properties and good producibility[Lütjering & Williams (2007)]. Today, it is often referred to as the "workhorse" of titanium alloys, accounting for more than 70% of all titanium alloy production worldwide[Dutta & Froes (2016)]. The widespread use of Ti-6Al-4V arises from its exceptional balance of specific strength (high strength at low density), ductility, fatigue resistance, and fracture toughness. However, its maximum service temperature is limited to roughly 300 °C, beyond which its mechanical performance degrades.

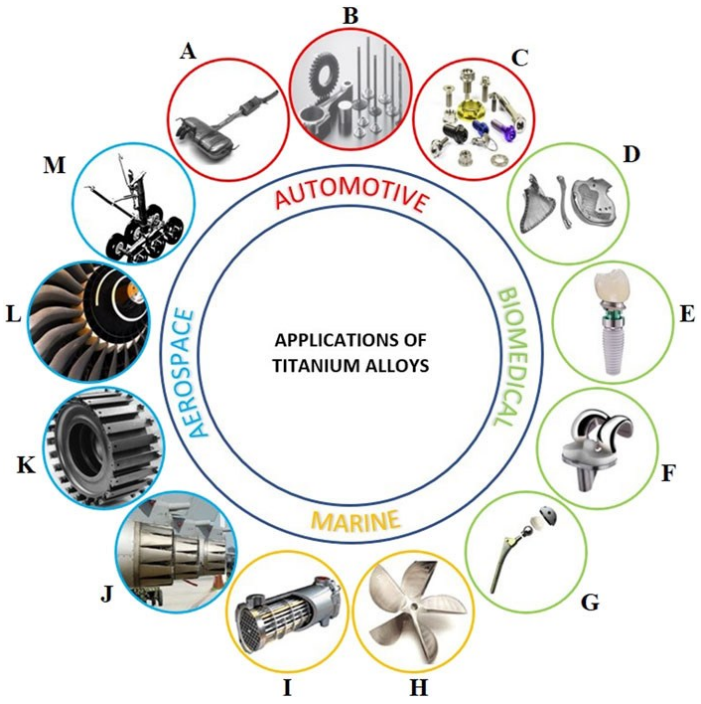

Figure 1. 1 Example applications of Ti and its alloys [adapted from Abakay et al. (2024)]

Ti-6Al-4V finds broad application in aerospace, biomedical, and general engineering fields. In the aerospace sector, this alloy is used extensively for airframe components, engine parts, and fasteners, owing to its high strength-to-weight ratio and good corrosion resistance. For example, modern aircraft and jet engines utilize Ti-6Al-4V in fan blades, compressor discs, and landing gear components, taking advantage of its fatigue strength and damage tolerance. The alloy's combination of strength and low density has even been exploited in sporting goods and marine equipment. In biomedical engineering, Ti-6Al-4V (particularly the extra-low interstitial, ELI, grade) has been a popular choice for orthopedic implants such as hip and knee replacements due to its biocompatibility and high fracture toughness. (It is noted that vanadium-containing alloys have raised some biocompatibility concerns, spurring the development of V-free variants for implants.) Overall, Ti-6Al-4V's favorable properties and performance have made it a high-performance material in aviation and medical industries, among others.

1.2 Laser Powder Bed Fusion (LPBF) Additive Manufacturing

Laser Powder Bed Fusion (LPBF) is an additive manufacturing process in which a high-power laser beam selectively melts thin layers of metal powder to build a component layer-by-layer from a digital 3D model[Joshi et al. (2023)]. In LPBF (also known as selective laser melting, SLM), a recoating mechanism spreads a thin layer of Ti-6Al-4V powder across a build platform, after which a focused laser scans the layer, melting the powder in the areas defined by the cross-sectional slice of the CAD model. This process is repeated iteratively as the build platform lowers, thereby consolidating successive powder layers into a fully dense 3D part. The technology enables near-net-shape fabrication of complex geometries that would be difficult or wasteful to produce by conventional methods, all with minimal material waste. Indeed, LPBF and other powder bed fusion techniques have demonstrated the capability to directly fabricate intricate Ti-6Al-4V components (e.g., with internal channels or lattice structures) with buy-to-fly ratios far superior to traditional machining and forging routes. The aerospace and medical sectors have been early adopters of titanium LPBF due to these advantages in design freedom and material efficiency.

LPBF-fabricated Ti-6Al-4V parts can achieve mechanical properties comparable to, or even exceeding, those of wrought and cast Ti-6Al-4V, provided the process parameters and post-treatments are properly optimized[Gibson et al. (2021)]. The rapid layer-wise melting and solidification inherent to LPBF produces a unique as-built microstructure that is distinctly different from conventional processing. Specifically, Ti-6Al-4V in the as-printed state typically consists of a martensitic α′ phase (hexagonal) in a fine acicular form, resulting from the extremely high cooling rates (on the order of 10^5–10^6 K/s) during laser processing. The prior β grains in LPBF Ti-6Al-4V tend to grow epitaxially through layers, yielding elongated columnar β grain structures that are textured along the build direction. Within these prior β columns, the as-solidified α′ martensite forms a dense network of fine needles (Figure 2.15) rather than the coarse α+β lamellar colonies seen in slowly cooled or annealed material. This refined martensitic microstructure imparts high as-built strength to LPBF Ti-6Al-4V. However, it also makes the material less ductile and can contribute to property anisotropy, since the colony of α′ variants and residual β may be aligned with the build direction. Without further heat treatment (e.g., stress relief or annealing), the metastable martensite also retains high internal dislocation density and lattice strains, which may influence deformation behavior and fatigue performance.

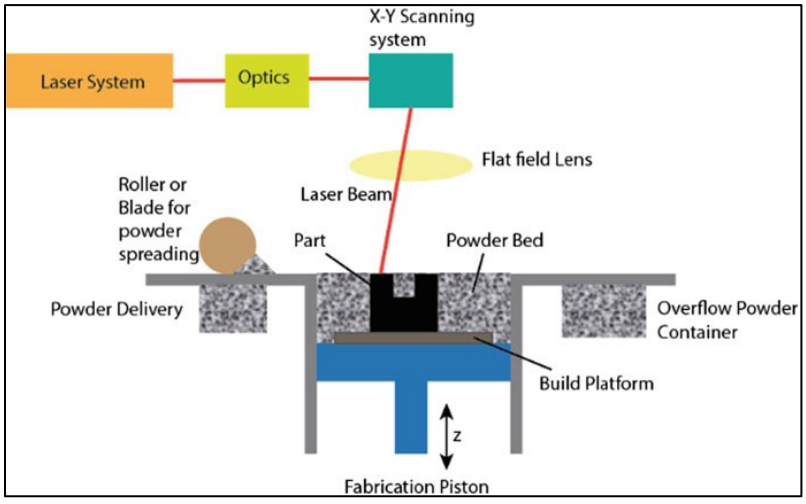

Figure 1. 2 Schematic of a typical powder bed fusion system [adapted from Joshi et al. (2023)]

LPBF Process Challenges – Defects, Residual Stresses, and Anisotropy: Despite the promise of LPBF for producing high-performance Ti-6Al-4V parts, several inherent challenges limit its standalone use. Process-induced defects are a primary concern. The complex physics of laser–powder interaction and rapid solidification can introduce porosity in the form of gas-entrapped pores, lack-of-fusion voids, or keyhole (overmelting) pores, especially if process parameters are not within an optimal window. Figure 1 illustrates how inappropriate laser power or scan speed can lead to either incomplete melting (and hence lack-of-fusion defects) or overheating (causing keyhole porosity), whereas a balanced parameter set produces a nearly fully dense microstructure. In LPBF Ti-6Al-4V, lack-of-fusion flaws often appear as irregular voids at prior scan track boundaries when energy input is insufficient (Figure 1b), while excessive energy can create deep vapor-driven keyhole cavities (Figure 1d). Even under optimized conditions, some microscale gas porosity (typically spherical <100 μm) may remain due to entrapped shielding gas or gas from the powder itself. These internal defects are detrimental to fatigue life and overall structural integrity, necessitating rigorous process control or post-build densification treatments.

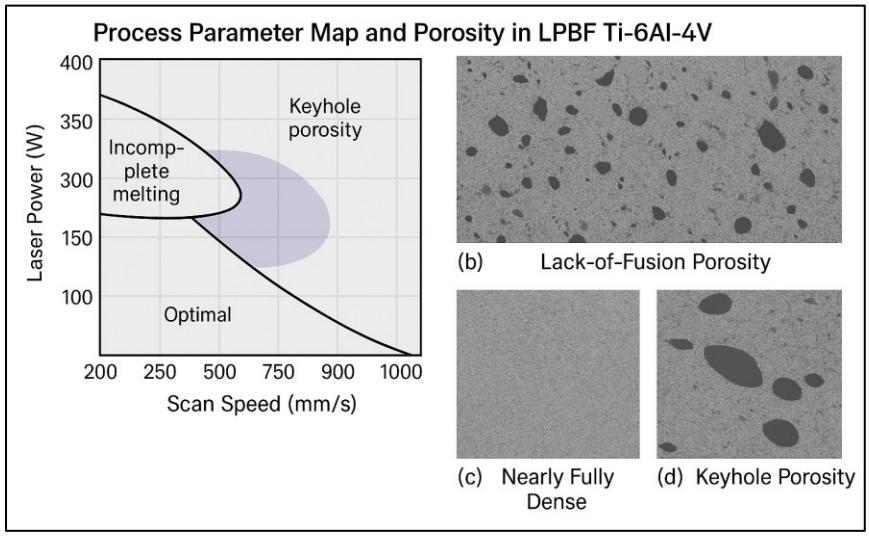

Figure 1. 3 Process parameter map and porosity in LPBF Ti-6Al-4V (a) Representative processing window showing regimes of incomplete melting (insufficient energy) and keyhole porosity (excessive energy) for a given laser power vs. scan speed. (b) Micrograph of a sample built at high scan speed (low energy density) exhibiting lack-of-fusion porosity (dark voids). (c) Nearly fully dense microstructure achieved at intermediate scan speed (optimal parameters). (d) Micrograph from a low scan speed, high energy build showing keyhole-type pores from overmelting. These examples highlight the need to tune LPBF parameters to minimize defects.

Another critical issue in LPBF is the accumulation of residual stresses. The steep thermal gradients and fast cooling in the laser melting process generate high magnitudes of tensile residual stress in as-built parts. For Ti-6Al-4V, residual tensile stresses approaching the alloy's yield strength (>900 MPa) have been measured at part surfaces and edges due to constrained contraction upon solidification. These tensile residual stresses can lead to build distortion, cracking (delamination between layers), or early fatigue crack initiation if not relieved. Typically, stress-relief annealing or hot isostatic pressing (HIP) is employed after LPBF to relax these stresses and thereby stabilize dimensions and improve fatigue performance.

Lastly, anisotropy in microstructure and mechanical response is a known challenge for LPBF Ti-6Al-4V. The layer-wise fabrication and columnar prior-β grains aligned with the build direction cause properties to differ with orientation. For example, as-built horizontal (in-plane) specimens often show higher yield strength but lower ductility compared to vertical specimens, due to the alignment of acicular

α′ laths and possible layer-bound defects relative to the loading direction. In one study, horizontally built samples had superior strength but inferior elongation because the β grain width spanned the tensile direction, whereas vertically built samples (loaded parallel to build direction) tended to open layer-layer lack-of-fusion flaws, leading to reduced ductility. Even after heat treatment, some degree of anisotropy can persist in additive-manufactured Ti-6Al-4V. This directional dependence of microstructure and properties must be carefully considered in design, and mitigating anisotropy remains an active area of research. In summary, the limitations of LPBF, including internal defects, high residual stresses, and anisotropic as-built microstructures, pose challenges to the reliability of Ti-6Al-4V components produced solely by additive means.

1.3 Hybrid Additive Manufacturing (HAM) with Hot Compression

To capitalize on the design benefits of LPBF while overcoming its material drawbacks, hybrid additive manufacturing (HAM) approaches have been proposed. In general, hybrid additive manufacturing is defined as the integration of additive processes with conventional manufacturing processes (often subtractive or forming) in a combined process chain, aiming to leverage the strengths of each and compensate for their limitations. By combining 3D-printed preforms with secondary processing, one can achieve final components with enhanced properties unattainable by additive or traditional methods alone[Khan et al. (2022)]. In the context of Ti-6Al-4V, a particularly promising hybrid strategy is to follow LPBF fabrication with a thermomechanical post-processing step, such as hot compression or forging of the as-built material. This approach (LPBF + hot deformation) marries the near-net-shape capability of additive manufacturing with the microstructural refinement of hot working.

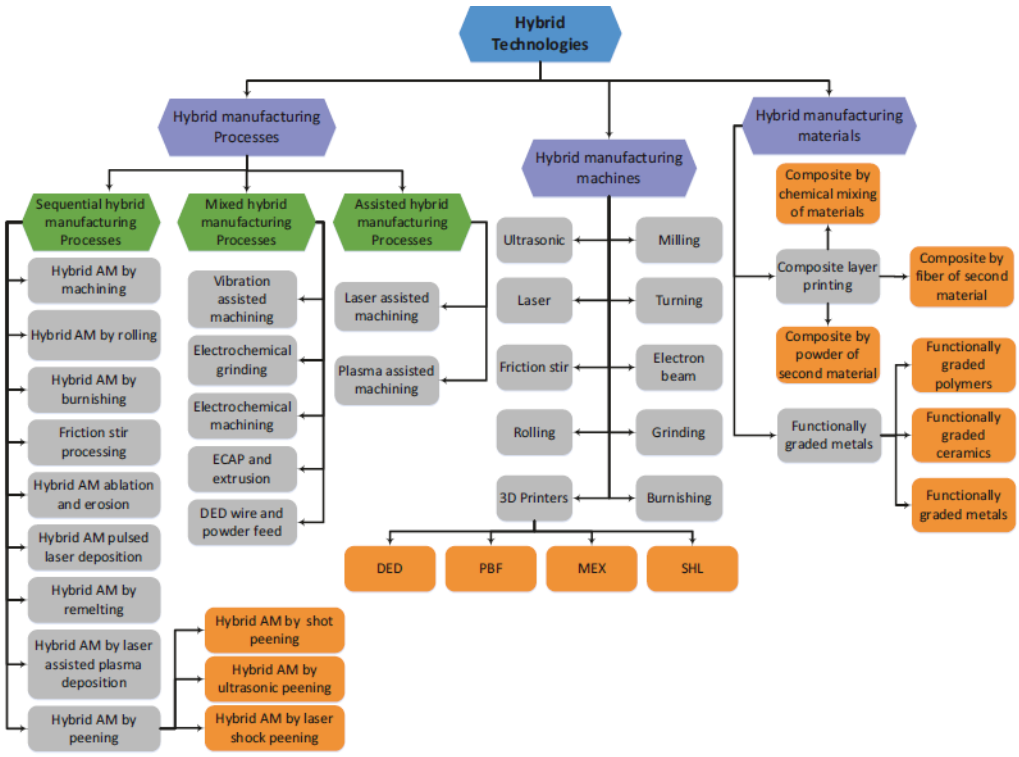

Figure 1. 4 Examples of hybrid technologies used in manufacturing [adapted from Gibson et al. (2021)]

Applying hot compression (e.g., forging or pressing at elevated temperature) to LPBF Ti-6Al-4V can effectively address the key issues of porosity, microstructure, residual stress, and anisotropy. Under sufficient temperature and plastic strain, the as-printed martensitic microstructure can undergo dynamic recrystallization and phase transformation. The result is a coarsened or globularized α+β microstructure that more closely resembles wrought Ti-6Al-4V, with reduced internal defects and residual stresses. For instance, recent studies combining additive preforms with forging have shown that when Ti-6Al-4V is hot deformed in the α+β phase region (sub-transus, 900–950 °C), the characteristic LPBF columnar prior-β grains are broken up and replaced by fine, equiaxed α grains (1–2 μm) within a retained β matrix. The typical coarse layer/colony microstructure from AM is no longer discernible after such thermomechanical processing. Additionally, the hot working helps to close any lack-of-fusion voids and collapse gas pores under the applied pressure, much like HIP but with the added benefit of strain-induced healing. The outcome is a significantly pore-free, refined microstructure with improved homogeneity.

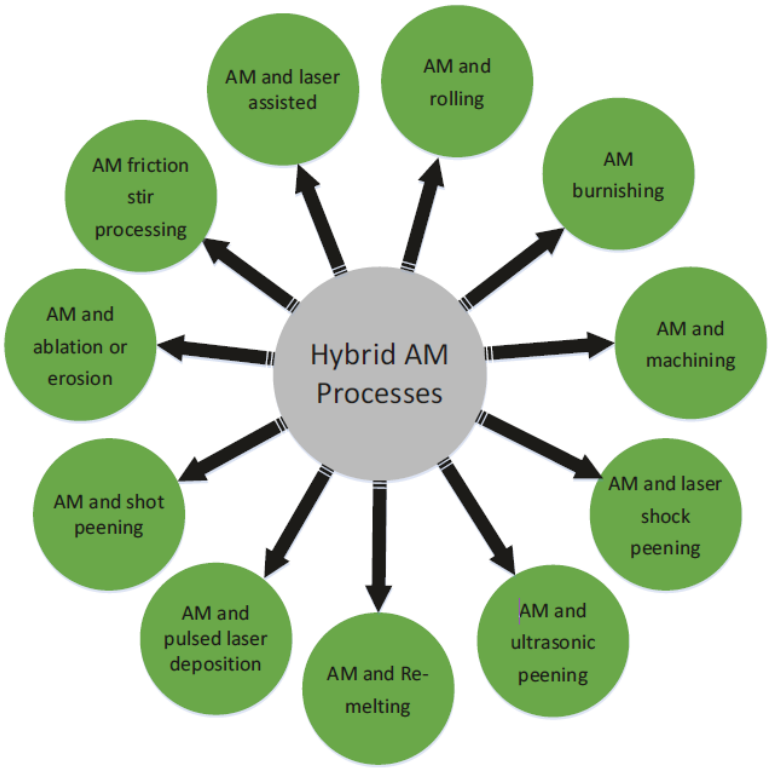

Figure 1. 5 Secondary hybrid AM processes [adapted from Gibson et al. (2021)]

Crucially, hybrid thermomechanical processing can enhance mechanical performance and isotropy. It has been reported that Ti-6Al-4V produced by LPBF or L-DED, when subjected to hot deformation in the 850–1000 °C range, exhibits lower flow stresses during deformation and yields a finer post-deformation microstructure compared to conventional wrought material processed under similar conditions. This implies that the additively fabricated material can be more malleable in certain hot-working regimes, potentially due to the metastable microstructure that is more prone to recrystallization. Moreover, forging in the sub-transus regime was found to significantly reduce anisotropy in mechanical properties; the forged material showed similar tensile strengths and ductility in different orientations, essentially erasing the anisotropic behavior that was present in the as-built state. By contrast, if the material is forged above the β-transus, the fully transformed β grains can grow large upon cooling and

reintroduce anisotropy and lower ductility. These studies underscore that a hybrid route of additive manufacturing followed by controlled hot compression can produce Ti-6Al-4V components with quality approaching or even exceeding that of conventional wrought forgings, while still retaining the advantages of near-net shape fabrication. In practice, such a hybrid approach could involve printing a near-net Ti-6Al-4V preform by LPBF, then performing a Hot Isostatic Pressing (HIP) and/or forging step to consolidate any porosity and refine the microstructure, and finally machining to final dimensions. This concept of *"print, press, and finish"* has the potential to mitigate LPBF's drawbacks (porosity, residual stress, microstructural metastability) and thus is an attractive solution for critical applications.

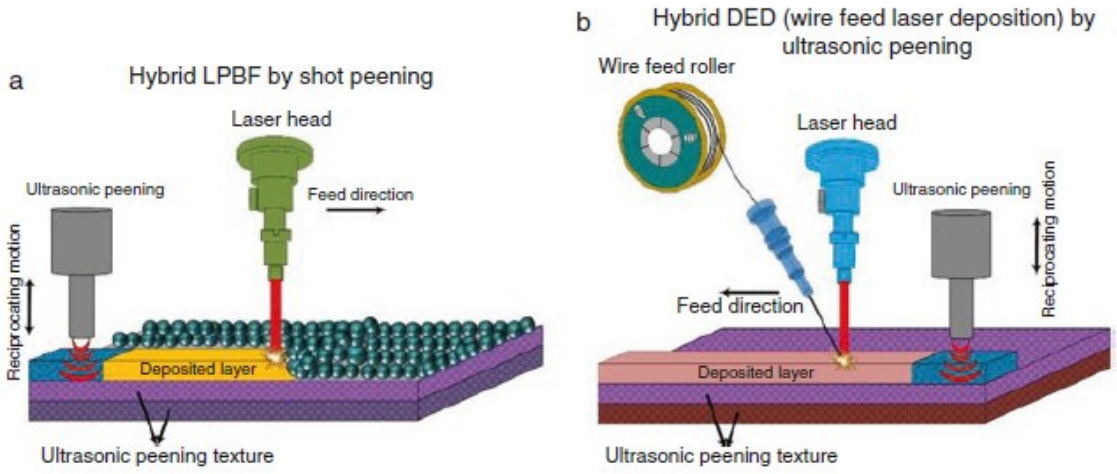

Figure 1. 6 Hybrid LB-PBF and DED by ultrasonic peening [adapted from Gibson et al. (2021)

Despite these promising findings, the development of hybrid LPBF + thermomechanical processes for Ti-6Al-4V is still in its early stages. Most prior works have been proof-of-concept demonstrations, and a systematic understanding of the thermomechanical behavior of LPBF-produced Ti-6Al-4V under hot deformation is limited. In particular, there is a need to clarify how initial as-built microstructures (including build orientation effects) influence material response during hot compression, and how processing parameters (deformation temperature, strain rate) should be optimized to achieve the desired microstructure and properties. The present thesis addresses this knowledge gap by investigating the hot compression behavior of LPBF Ti-6Al-4V in detail.

1.4 Research Gap and Objectives

As outlined above, Laser Powder Bed Fusion enables the fabrication of Ti-6Al-4V components with complex geometries but leaves challenges in microstructure and internal quality, while hot working can improve those aspects, but is not yet well-understood for additively made material. A clear *research gap* exists in understanding the thermomechanical response of LPBF-fabricated Ti-6Al-4V, especially when subjected to high-temperature deformation. Previous studies have largely focused on as-built versus heat-treated static properties (tensile, fatigue, etc.) of LPBF Ti-6Al-4V. However, there is limited published data on how LPBF Ti-6Al-4V behaves under compressive loading at elevated temperatures, conditions that simulate forging or hot forming. In particular, the influence of build orientation (the orientation of the part during printing, which dictates the grain texture and defect alignment) on flow stress and microstructural evolution during hot compression remains insufficiently understood. While anisotropic tensile behavior in AM Ti-6Al-4V has been documented, it is not yet clear whether a vertically built

sample and a horizontally built sample will exhibit different work-hardening or dynamic recrystallization behavior when both are compressed at high temperature. This thesis aims to fill these gaps by experimentally evaluating the hot compression behavior of LPBF Ti-6Al-4V and assessing the role of build orientation.

Objectives of the Study: The primary objectives of this research are twofold:

1. **Investigate Hot Compression Flow Behavior and Microstructure Evolution:** Conduct controlled hot compression tests on LPBF-fabricated Ti-6Al-4V specimens to characterize their flow stress behavior (stress–strain response) and the associated microstructural evolution (phase transformations, grain morphology changes) under various temperatures and strain rates. This includes determining how the as-built martensitic microstructure decomposes or recrystallizes when deformed at elevated temperatures, and comparing the flow curves to those of conventional wrought Ti-6Al-4V. By doing so, the study seeks to establish the constitutive behavior and key deformation mechanisms of additively manufactured Ti-6Al-4V in the hot-work regime.
2. **Assess the Effect of Build Orientation:** Evaluate how the build orientation of the LPBF samples (e.g., vertical build vs. horizontal build) influences the hot compression behavior. This involves comparing flow stress characteristics (e.g., peak flow stress, flow softening) and post-compression microstructures for samples printed in different orientations. The goal is to determine whether anisotropic features from the LPBF process (such as columnar grains or layer-induced defects) lead to measurable differences in high-temperature deformability and microstructural outcomes. Understanding this will inform whether certain build orientations are preferable for subsequent forming operations, or if tailored hot compression routes are needed to homogenize properties in differently oriented parts.

By fulfilling these objectives, the work will contribute valuable knowledge on combining LPBF with thermomechanical processing for Ti-6Al-4V. It will shed light on the feasibility of a hybrid manufacturing route to produce Ti-6Al-4V with superior performance, and guide how build orientation and processing conditions should be controlled to achieve isotropic and defect-free microstructures.

1.5 Thesis Structure

The remainder of this thesis is organized into five chapters. **Chapter 2 (Literature Review)** provides a comprehensive review of relevant literature, including the fundamentals of Ti-6Al-4V metallurgy, details of LPBF processing and typical microstructures, prior research on LPBF post-processing (heat treatment and HIP), and studies on hot deformation behavior of titanium alloys (with emphasis on any work done on additively manufactured Ti-6Al-4V) along with effect of building orientation and advances on constitutive modeling. **Chapter 3 (Materials and Methods)** describes the experimental methodology of the research. This includes the LPBF fabrication procedure for the Ti-6Al-4V samples, the design of the hot compression tests (sample geometry, test temperatures, strain rates, and instrumentation), and the characterization techniques employed (such as optical microscopy, scanning electron microscopy, and X-ray diffraction for microstructure analysis, as well as mechanical testing details). **Chapter 4 (Results)** presents the experimental results obtained. The flow stress–strain curves for different conditions and orientations are reported, and the evolution of microstructure (phase changes, grain structure) before and after hot compression is documented with images and quantitative metrics. **Chapter 5 (Discussion)** offers an in-depth analysis of the results. The hot compression behavior of LPBF Ti-6Al-4V is interpreted in terms of underlying mechanisms (e.g., work-hardening, dynamic recrystallization, or flow softening),

and the influence of build orientation on these mechanisms is analyzed. The discussion also compares the findings with conventional forged Ti-6Al-4V behavior and with literature, evaluating to what extent the hybrid approach mitigates LPBF-induced issues like anisotropy and porosity. **Chapter 6 (Conclusions and Future Work)** concludes the thesis by summarizing the key findings and contributions. It outlines the conclusions regarding the hot compression behavior and orientation effects in LPBF Ti-6Al-4V, and provides recommendations for future research or process optimization in the hybrid additive manufacturing of titanium alloys. Through this structured approach, the thesis addresses the stated objectives and highlights the potential of combining LPBF with hot deformation to advance the performance of Ti-6Al-4V components.

Chapter 2 – Literature Review

2.1 Additive Manufacturing of Titanium Alloys

Ti-6Al-4V (Ti64), a two-phase (α+β) titanium alloy, is the most widely utilized titanium grade in industry, accounting for nearly half of all titanium alloy production. Its enduring popularity stems from an exceptional combination of high strength-to-weight ratio, excellent corrosion resistance, biocompatibility, and good workability, making it a dominant material in demanding aerospace and biomedical applications Lin & Chen (2011). In recent years, Additive Manufacturing (AM) technologies have revolutionized the production of complex Ti64 components, offering significant advantages such as minimal material waste and the ability to fabricate intricate geometries. Among these, Laser Powder Bed Fusion (LPBF) stands out as a widely employed AM process for titanium alloys. LPBF selectively melts thin layers of Ti64 powder using a high-power laser in an inert gas environment, building parts layer-by-layer. This process is favored for its fine resolution, high dimensional accuracy, and capability to achieve near-full density in Ti64 components. The inherent weldability of Ti64, facilitating sound, crack-free melt pools under proper shielding and parameters, further enhances its processability in LPBF Tao et al. (2019).

Despite the numerous advantages of LPBF, the process subjects the material to extreme thermal conditions that significantly influence the resulting microstructure and mechanical properties. During solidification, the alloy experiences extremely high cooling rates, typically on the order of 105–107 K/s, and steep temperature gradients, approximately 106–107 K/m. Titanium's intrinsically low thermal conductivity, an order of magnitude lower than that of steel or aluminum alloys, exacerbates these steep thermal gradients and localized heat accumulation. Consequently, LPBF-fabricated Ti64 solidifies in a far-from-equilibrium state. The as-built microstructure is predominantly martensitic (α′ phase) and can contain various internal defects, such as porosity and lack of fusion, alongside significant tensile residual stresses. These microstructural features and defects, coupled with the inherent layer-wise texture, can degrade critical properties like ductility and fatigue resistance in the as-printed state. To mitigate these issues and enhance metallurgical structure and mechanical performance, post-processing treatments—such as stress-relief annealing, hot isostatic pressing (HIP), or solution aging—are commonly applied. These treatments temper the martensitic microstructure and reduce residual stresses, enabling the AM material to achieve properties comparable to its wrought counterparts.

The challenges and advancements in AM of Ti-6Al-4V have been extensively reviewed. Nguyen et al. (2022) provide a critical examination of various AM techniques for Ti-6Al-4V, including Electron Beam Melting (EBM), Selective Laser Melting (SLM), and Directed Energy Deposition (DED). Their findings indicate that while EBM parts can exhibit strength comparable to traditionally manufactured materials, SLM and DED often offer superior strength but may suffer from lower fatigue life due to higher porosity and residual stress, issues directly stemming from the rapid solidification conditions. The review underscores the vital role of post-processing techniques in enhancing properties and discusses the broader challenges and advantages of AM processes, highlighting their relevance in critical applications.

Focusing specifically on LPBF, Ni et al. (2025) delve into recent advancements in the LPBF of Ti-6Al-4V alloys, emphasizing microstructure, mechanical properties, and machinability. They highlight the pervasive issue of non-stationary thermal history during LPBF, which leads to the formation of defects and residual stresses. Their work systematically reviews the impact of various process parameters and

laser strategies on forming properties, emphasizing the critical need for optimization to enhance material performance and overcome these inherent challenges. This review provides a comprehensive overview of current research and practical implications for improving LPBF-fabricated titanium alloys.

Further research has explored specific strategies for optimizing LPBF parameters to control microstructure and improve mechanical properties. Dhiman et al. (2024) investigated microstructure control in Ti-6Al-4V fabricated via high-power (600 W) LPBF, aiming to concurrently enhance build rate while maintaining mechanical integrity and dimensional accuracy. Their systematic exploration of scanning speed, hatch spacing, and focal offset distance revealed that high laser power significantly narrows the processing window but facilitates the formation of desirable microstructures, such as lamellar α+β and globular α, even at lower energy densities compared to conventional low-power LPBF. Optimal parameters yielded high-density parts with fine lamellar α+β microstructures and ductile mechanical behavior, demonstrating the potential of high-power LPBF for efficient, near-net-shape manufacturing of high-performance titanium components. Similarly, Xu et al. (2015) investigated the additive manufacturing of Ti-6Al-4V using SLM to achieve strong and ductile materials through *in situ* martensite decomposition. By carefully optimizing SLM parameters, they successfully created ultrafine lamellar (α+β) microstructures, resulting in a notable tensile elongation of 11.4% and a yield strength exceeding 1100 MPa. This approach directly addresses the common limitation of high strength but low ductility typically observed in SLM-fabricated Ti-6Al-4V, showcasing the importance of process parameter control in achieving properties comparable to traditional methods.

In conclusion, while LPBF offers significant advantages for fabricating complex Ti64 components, the extreme thermal conditions inherent to the process lead to unique as-built microstructures and potential defects that can compromise mechanical performance. Extensive research efforts are focused on understanding and mitigating these challenges through process parameter optimization, post-processing treatments, and innovative *in situ* microstructural control strategies. These studies collectively underscore the critical importance of tailoring LPBF parameters and subsequent treatments to achieve desirable microstructures and mechanical properties in additively manufactured Ti-6Al-4V, forming the foundation for further investigation into its hot deformation behavior.

2.2 Hybrid Additive Manufacturing (HAM)

Hybrid Additive Manufacturing (HAM) encompasses manufacturing approaches that integrate additive processes with secondary, often conventional, processes within a unified workflow. The primary objective of HAM is to overcome inherent limitations of stand-alone AM techniques—such as anisotropic microstructures, residual stresses, internal defects, and suboptimal surface finish—by leveraging the complementary strengths of traditional manufacturing methods. In practice, this can involve combining an AM technique like Laser Powder Bed Fusion (LPBF) or Directed Energy Deposition (DED) with either *in situ* thermomechanical steps (e.g., intermittent deformation or machining) during the build, or subsequent post-build thermomechanical processing (e.g., forging, extrusion, or hot compression) and/or subtractive machining.

One manifestation of HAM involves interspersing AM build steps with complementary pLütjering & Williams (2007)]. Today, it is often demonstrated such an approach by coupling a DED process with intermittent milling. This method involves pausing deposition after certain layers to machine the surface before continuing the build. This type of hybrid AM framework enables the incorporation of thermomechanical treatments directly during part fabrication, rather than solely as a post-completion

step. In their study, the hybrid DED+milling of Ti-6Al-4V led to a notable improvement in ductility without sacrificing strength. The intermittent milling not only removed surface asperities but also introduced cyclic thermal pauses, which facilitated partial stress relief and promoted microstructural coarsening at the layer interfaces. This resulted in the transformation of as-built martensitic α′ into slightly coarser α laths at these interfaces, thereby facilitating dislocation motion. Consequently, this hybrid route achieved a remarkable ≈63% increase in tensile ductility (elongation) in as-deposited Ti-6Al-4V while retaining equivalent yield strength to the non-machined (as-printed) material. Such improvements are largely attributed to the alleviation of residual stress and the tailored microstructure induced by these thermomechanical interruptions during the build process.

A highly promising HAM strategy, particularly relevant to the current thesis, involves using AM to produce a near-net-shape preform, which is then subjected to a thermomechanical post-process such as forging or hot compression. This approach combines the design flexibility and material efficiency of AM (e.g., reduced buy-to-fly ratio) with the microstructural refinement and property enhancement capabilities of thermomechanical processing.

Hemes et al. (2021) proposed a pioneering hybrid manufacturing route for Ti-6Al-4V wherein preforms made by laser DED were subsequently hot forged as a controlled thermomechanical processing step. In their study, an additively deposited Ti-6Al-4V block was reheated and forged below the β-transus temperature. This sub-β transus forging successfully broke down the coarse columnar prior-β grains and fine acicular α′ microstructure characteristic of AM, yielding a very fine (≈0.8–2 μm) equiaxed α grains with a small fraction of β phase. Crucially, the typical layer-induced anisotropy of the AM microstructure was no longer discernible after forging, and tensile properties (strength and ductility) became isotropic, similar to or even superior to those of conventionally forged Ti-6Al-4V. Conversely, performing the forging above the β-transus was less effective, resulting in coarser prior-β grains, preserved anisotropy, and lower strength and ductility. Several other studies corroborate the benefits of combining AM with post-build hot deformation. Jiang et al. (2017) demonstrated the feasibility of integrating 3D AM with compressive forming to enhance mechanical properties, specifically in stainless steel 316L. Their work highlighted significant improvements in tensile strength and ductility through hot forging and heat treatment, with microstructural analysis via EBSD revealing grain refinement and reduced porosity. While on a different alloy, this study validates the fundamental concept of using post-build thermomechanical treatment to address common AM defects and improve properties.

More directly, Bambach et al. (2019) discussed a novel processing route for Ti-6Al-4V forgings using preforms created by Selective Laser Melting (SLM). Their research investigated microstructure evolution during hot working and heat treatment, revealing that SLM preforms exhibit good hot workability and can achieve microstructures comparable to conventional forgings. Sizova & Bambach (2018) further investigated the hot workability and microstructure evolution of SLM Ti-6Al-4V preforms, noting that SLM samples exhibit favorable hot working characteristics, including lower activation energy and peak stresses compared to conventional wrought materials. These findings suggest that AM can effectively produce hot workable titanium alloys, paving the way for innovative manufacturing processes.

A significant advantage of using AM preforms for hot deformation is their unique as-built microstructure. Bambach et al. (2021) investigated the hot deformation behavior of Ti-6Al-4V produced via SLM and DED, comparing it with conventional wrought material. They revealed that AM materials exhibit significantly lower flow stresses and faster globularization kinetics due to their non-equilibrium microstructures, particularly the presence of fine α′-martensite and a percolating β-phase. Compression

tests showed that AM materials deform more easily, especially at lower temperatures, potentially enabling single-stage forging. This inherent hot workability of AM preforms offers benefits such as reduced forming forces, improved material yield, and simplified processing in hybrid routes.

The application of hot forging to Wire-Arc Additive Manufacturing (WAAM) preforms also demonstrates similar advantages. Maurya et al. (2022) investigated a hybrid process combining WAAM and hot forging for Ti-6Al-4V, addressing defects and anisotropic properties. They developed an artificial neural network model to refine flow stress predictions, identifying optimal processing conditions at 900–950 °C and low strain rates. The study confirmed that this hybrid method enhances mechanical properties, yielding equiaxed microstructures with improved strength and ductility. Similarly, Sizova et al. (2019) explored a WAAM-hot forging hybrid route for Ti-6Al-4V turbine blades, demonstrating that WAAM material exhibited similar flow behavior but approximately 20% lower flow stresses compared to conventionally wrought Ti-6Al-4V, indicating reduced forming loads. Effective globularization of the α-phase was observed, resulting in dense, defect-free microstructures in the final forged components. Even for other alloy systems, such as titanium aluminides (TiAl), Sizova et al. (2021) highlighted that AM-produced TiAl exhibits finer microstructures and lower flow stress, demonstrating that moderate hot working can effectively refine the microstructure and enhance mechanical properties as an alternative to hot-isostatic pressing (HIP).

In conclusion, Hybrid Additive Manufacturing strategies, particularly those involving the combination of LPBF (or other AM methods) with subsequent thermomechanical treatments like hot compression or forging, offer a robust solution for overcoming the limitations of as-built AM components. These studies consistently demonstrate that such hybrid approaches can effectively refine the typically anisotropic and martensitic as-built microstructures, reduce residual stresses, eliminate defects, and significantly enhance mechanical properties, often to levels comparable to or exceeding conventionally wrought materials. The inherent hot workability of AM materials, characterized by lower flow stresses, further motivates the exploration of integrated LPBF and hot compression processes for producing high-performance Ti-6Al-4V components with tailored microstructures and superior mechanical isotropy. This approach forms a critical foundation for the present thesis, which seeks to further understand and optimize the hot compression behavior of LPBF-fabricated Ti-6Al-4V.

2.3 Heat Treatment of Additively Manufactured Ti64

Heat treatments constitute an indispensable phase in the overall manufacturing process of additively manufactured (AM) Ti-6Al-4V (Ti64) components. These post-fabrication thermal processes are crucial for recrystallizing the as-built material, alleviating residual stresses, and ultimately achieving desired microstructures and mechanical properties for various applications, including those subjected to subsequent thermomechanical processing. An appropriate heat treatment is therefore essential for optimizing the performance and facilitating further processing of near-net-shape components obtained via AM.

The rapid solidification inherent to AM processes, such as Laser Powder Bed Fusion (LPBF), typically results in out-of-equilibrium microstructures, predominantly composed of fine α′ martensite, along with potential internal defects and significant residual stresses. These as-built characteristics often necessitate post-fabrication heat treatments to enhance ductility and reduce defects. For instance, Vilaro et al. (2011) investigated the microstructures of Ti-6Al-4V alloy produced via selective laser melting (SLM) and the profound effects of various heat treatments on their mechanical properties. Their study highlighted that

while optimized heat treatments could significantly improve yield and ultimate tensile strengths and allow control over grain morphology, persistent anisotropy in mechanical properties often remained due to inherent manufacturing defects. This suggests that further optimization, potentially combined with techniques like hot isostatic pressing (HIP), may be required for enhanced performance and isotropy.

Further research has established clear correlations between heat treatment parameters and the resulting microstructural features and mechanical responses. Etesami et al. (2022) conducted a detailed investigation into the effects of heat treatment on the microstructure and mechanical properties of Ti-6Al-4V alloy produced via laser-based powder-bed fusion (LPBF). Their work established critical correlations between heat treatment parameters (temperature, time, and cooling rate) and the resulting microstructural features, specifically the evolution of α′ and β phases. The study found that heat treatment could effectively enhance ductility, though with varying impacts on tensile strength depending on the specific treatment conditions. Fractography analysis further revealed transitions from brittle to ductile fracture modes, providing valuable insights for optimizing the mechanical performance of LPBF Ti-6Al-4V through tailored thermal cycles.

More recently, advanced computational approaches, such as artificial neural networks (ANNs), have been employed to model and optimize heat treatment processes. Maurya et al. (2025) developed an ANN model to analyze the complex relationship between microstructural features and the mechanical properties of Ti-6Al-4V alloys. Their model effectively demonstrated how specific heat treatments influence microstructure, which in turn impacts key mechanical properties such as ultimate tensile strength (UTS), yield strength (YS), and elongation. By employing an index of relative importance (IRI), the study quantified the impact of various microstructural parameters, with the model demonstrating high accuracy in predictions and offering a user-friendly graphical interface for practical applications. This research significantly contributes to the systematic optimization of heat treatment processes for enhanced material performance.

In conclusion, heat treatments are a fundamental and critical step in the post-processing of additively manufactured Ti-6Al-4V. They are essential for transforming the non-equilibrium as-built microstructures, mitigating defects and residual stresses, and ultimately tailoring the mechanical properties to meet demanding application requirements. The ability to precisely control microstructural evolution through optimized heat treatment parameters, increasingly aided by advanced modeling techniques like ANNs, is paramount for unlocking the full potential of AM Ti64 components, particularly when they are intended for subsequent thermomechanical processes such as hot compression.

2.4 Hot Compression & Ti64: Flow stress, Microstructures, and their quantification

Hot compression is a critical thermomechanical process employed to refine the microstructure and enhance the mechanical properties of Ti-6Al-4V (Ti64), particularly when fabricated via additive manufacturing (AM). This section reviews key studies on the flow stress behavior, microstructural evolution, and the quantification methodologies applied during the hot deformation of Ti64, with a specific focus on insights relevant to additively manufactured variants.

- Hot Deformation Behavior and Microstructural Evolution

Research into the hot deformation of Ti64 has extensively explored the influence of thermomechanical parameters on flow stress and microstructural evolution. Roush et al. (2001) investigated the anisotropy of plastic flow and microstructure evolution in laser-deposited Ti-6Al-4V during hot working. Their findings indicated negligible anisotropy in stress-strain behavior and dynamic globularization kinetics, emphasizing that α-platelet thickness, rather than grain shape, significantly influences plastic flow. This study, employing isothermal hot compression tests, highlighted the crucial role of α-lath thickness in understanding deformation characteristics, aligning with observations in ingot metallurgy materials. Similarly, Semiatin & Bieler (2001) further elucidated the influence of α-platelet thickness on plastic flow, noting a Hall–Petch dependence and the loss of interface strengthening during deformation. Perumal et al. (2016) also found that while α-lath thickness minimally affects flow behavior, the orientation of α-laths evolves with strain, aligning perpendicularly to the loading direction, contributing to the understanding of globularization mechanisms.

The starting microstructure profoundly impacts hot deformation behavior. Matsumoto et al. (2013) investigated the microstructural evolution of Ti-6Al-4V with an acicular α′ martensite starting microstructure, common in as-built AM materials, during hot deformation. Their work highlighted a transition from continuous dynamic recrystallization (CDRX) to discontinuous dynamic recrystallization (DDRX) with increasing strain, emphasizing the role of nucleation sites and grain fragmentation. They revealed that DDRX is favored in the α′ martensite microstructure due to its high dislocation density and numerous nucleation sites, leading to an ultrafine-grained structure. Zhang et al. (2017) further explored the influence of initial microstructures (transformed β, bimodal, and α′ martensitic) on plastic flow and microstructural evolution during sub-transus deformation. Their Gleeble simulator study demonstrated that the α′ martensitic microstructure yields a homogeneous ultra-fine grained structure at high strain rates, underscoring the significance of initial microstructure for grain refinement.

Comprehensive studies on the hot deformation behavior of Ti-6Al-4V across various temperatures and strain rates have identified critical processing windows and mechanisms. Seshacharyulu et al. (2000) investigated extra-low interstitial (ELI) grade Ti-6Al-4V, identifying temperature-strain rate windows for defect-free hot working, along with conditions leading to flow instabilities and cracking. Ding et al. (2002) explored microstructural evolution during thermomechanical processing in both (α+β) and β phase fields, observing dynamic recrystallization (DRX) predominantly in the β phase field and concurrent phase transformation in the (α+β) field. Shafaat et al. (2011) modeled the hot compression flow behavior of Ti-6Al-4V in the α+β phase region, emphasizing DRX as the primary restoration mechanism. Zherebtsov et al. (2011) investigated spheroidization of lamellar microstructures during warm deformation and annealing, identifying temperature-dependent mechanisms like boundary splitting and termination migration. L. Wang et al. (2023) demonstrated that melt hydrogenation can enhance hot workability in Ti-6Al-4V composites by promoting DRX and reducing peak stress during hot compression.

- Hot Deformation of Additively Manufactured Ti64

While foundational studies on wrought Ti64 are abundant, the hot deformation behavior of additively manufactured Ti64 presents unique characteristics due to its distinct as-built microstructure. Semiatin et al. (2001) noted that the flow curves of laser-deposited Ti-6Al-4V were similar to ingot-metallurgy material, with significant flow softening at sub-transus temperatures, suggesting viability for near-net-shape forgings. However, more recent studies highlight key differences.

Mostafa et al. (2018) investigated the hot compression behavior of selectively laser-melted IN718 alloy, revealing that strain rate significantly influences mechanical behavior, with DRX predominant at higher strain rates and dynamic recovery (DRV) at lower rates. Similarly, Bambach et al. (2018) studied LMD Inconel 718, finding that while as-built material was unsuitable for hot working due to brittle Laves phases, homogenization significantly improved ductility and hot workability, enabling DRX similar to wrought IN718.

Crucially for Ti64, Saboori et al. (2020) investigated the hot deformation behavior of Ti-6Al-4V produced via Electron Beam Melting (EBM) in the single β-phase field. They found lower flow stress in EBM samples compared to wrought counterparts, attributed to the initial microstructure and porosity, and a significantly lower activation energy for hot deformation. This suggests that AM Ti64 may be more amenable to hot working. Li et al. (2015) conducted extensive thermomechanical testing on Ti-6Al-4V fabricated via 3D laser deposition additive manufacturing (LDAM) across a wide range of strain rates and temperatures. They observed significant strain-rate sensitivity and temperature-dependent flow behavior, with minimal anisotropy despite visible stratification. Their work also identified initial defects (voids, lack-of-fusion pores) as crack initiation sites and noted adiabatic shear bands as a dominant failure mechanism in compression. These studies collectively indicate that while AM materials offer unique advantages in hot workability (e.g., lower flow stress), their inherent defects and specific microstructures necessitate careful consideration during hot compression.

- Microstructural Quantification and Advanced Analysis

Accurate quantification of microstructural features is paramount for understanding and predicting the mechanical performance of Ti-6Al-4V, especially in complex AM microstructures. Over the past two decades, research has evolved from manual stereological techniques to advanced image analysis and machine learning-based predictive modeling.

Early foundational work by Tiley et al. (2004) established rigorous stereological procedures for quantifying key microstructural features in α+β titanium alloys, including Widmanstätten α-lath thickness, colony size, and prior β grain size. Collins et al. (2009) extended this to α+β-processed Ti-6Al-4V, incorporating equiaxed α size and volume fraction using semi-automated tools to reduce user bias and improve measurement fidelity. They demonstrated correlations between quantified features, processing parameters, and mechanical properties. Yang & Liu (2016) introduced an SEM-based image processing method to quantify microstructural changes induced by milling in Ti-6Al-4V, linking cutting parameters to variations in β-phase content and grain refinement.

With the increasing complexity of AM microstructures, automated and high-throughput quantification methods have become essential. Karra et al. (2022) developed an open-source, Python-based image analysis pipeline using OpenCV for automated quantification of α-lath thickness and phase volume fractions in DED-processed Ti-6Al-4V. Their method, validated against commercial software, enables high-throughput analysis across large image datasets. Loughnane et al. (n.d.) focused on uncertainty quantification in α-lath measurements using MIPAR and statistical tools, correlating α-lath thickness distributions with thermal gradients and melt pool areas in LENS®-processed Ti-6Al-4V.

More recently, machine learning has emerged as a powerful tool for microstructure prediction. Cao et al. (2024) developed a conditional generative adversarial network (cGAN) to predict α′ martensite morphology in LPBF-fabricated Ti-6Al-4V based on laser power and scan speed. Their model accurately

reconstructed and predicted microstructural features such as lath width and length, achieving prediction errors below 20%. They also introduced size distribution maps to visualize complex, nonlinear relationships between processing parameters and martensite morphology, offering a new paradigm for process optimization and microstructure control in AM.

In summary, the hot compression of Ti-6Al-4V, particularly AM variants, is a well-researched field, with studies elucidating the influence of initial microstructure, temperature, and strain rate on flow stress and microstructural evolution. While AM Ti64 often exhibits lower flow stresses and unique deformation mechanisms due to its as-built state, careful control of hot compression parameters is crucial to achieve desired properties. The evolution of microstructural quantification from manual methods to advanced image analysis and machine learning provides increasingly robust tools for linking processing, microstructure, and properties. This comprehensive understanding forms the basis for further investigation into the optimized hot compression behavior of LPBF-fabricated Ti-6Al-4V, aiming to leverage its unique characteristics for enhanced mechanical performance.

2.5 Effect of Building Orientation

The building orientation of Ti-6Al-4V (Ti64) components fabricated via additive manufacturing (AM) plays a pivotal role in shaping both microstructural evolution and mechanical behavior, particularly in terms of strength, ductility, hardness, and fatigue resistance. This directional sensitivity stems from anisotropic thermal histories that develop during layer-by-layer deposition processes such as Selective Laser Melting (SLM) and Electron Beam Melting (EBM). Niñerola & Giner (2025) demonstrated that EBM-fabricated Ti64 exhibits orientation-dependent fracture toughness, as cracks propagating perpendicular to columnar β grains encountered more grain boundary resistance than those aligned parallel to the build direction. A similar phenomenon was observed by Murchio et al. (2021) in SLM-printed Ti64 lattice struts, where reduced fatigue life at shallow build angles (e.g., 0°) was linked to increased surface roughness and cross-sectional irregularities caused by the stair-step effect.

Further corroborating the anisotropic mechanical response, Ataee et al. (2019) showed that both SLM and EBM gyroid scaffolds exhibited significantly higher hardness and wear resistance in the transverse direction, a result attributed to finer grain structures and better phase uniformity. Ren et al. (2019) and He et al. (2022) both explored the influence of build orientation on the mechanical behavior of Ti-6Al-4V produced via laser-based additive manufacturing. Ren et al. (2019) focus on selective laser melting (SLM) and demonstrate that orientation significantly affects residual stress, pore distribution, and crystallographic texture, with tensile strength peaking at 45° and elongation highest at 0°. He et al. (2022)extend this understanding to high-temperature applications, showing that build direction influences kinematic hardening, while elevated temperatures alter stiffness, strength, and fracture modes. Together, these studies underscore the critical role of build orientation in determining both room and high-temperature performance of LPBF Ti-6Al-4V components. Orientation also influences micromechanical properties such as strain rate sensitivity (SRS), with Chandra Kaushik et al. (2022) reporting that EBM-Ti64, while softer than its SLM counterpart, demonstrated greater SRS due to favorable α-prismatic plane alignment. In parallel, Meng et al. (2024) employed micro-CT and SEM to reveal that fatigue cracks in L-PBF Ti64 initiated preferentially along near-surface melt pool boundaries that align with the build direction, emphasizing how defect orientation governs crack evolution. Cutolo et al. (2022) further showed that machining or electro-plasma polishing of Ti64 coupons significantly enhanced fatigue life by removing micro-notches induced by orientation-specific surface roughness.

Machine learning methods have also captured this orientation-dependence. H. Wang et al. (2024) built an ML model that predicted tensile strength of L-PBF Ti64 by incorporating build orientation and microstructural features, finding that vertically built samples (parallel to heat flow) formed martensitic α′ structures with high strength but lower ductility, whereas horizontal builds fostered more equiaxed grains with a better strength-ductility balance. These results aligned with thermomechanical tests by Regidor et al. (2025), where hot-deformed Ti64 samples exhibited orientation-dependent α-lath fragmentation and flow stress response. H. Wang et al. (2025) additionally showed that, in L-DED Ti64, scanning-direction-aligned specimens exhibited improved tensile and fracture properties due to the continuous grain boundary α (GB-α) alignment, whereas build-direction-aligned samples showed increased microcrack density and reduced elongation.

Importantly, the fatigue performance of complex porous Ti64 structures is also highly orientation-sensitive. Araya-Calvo et al. (2024) examined both TPMS-gyroid and stochastic lattices fabricated by PBF-LB, finding that vertically built samples had superior fatigue strength compared to horizontally built ones, due to reduced surface-connected defects and more favorable melt pool alignment. Chemical etching further enhanced these benefits by smoothing surface irregularities, particularly in horizontal builds that are more susceptible to stress concentration. Collectively, these studies affirm that building orientation is not merely a design parameter but a primary determinant of microstructural morphology, defect architecture, and resultant mechanical performance in AM Ti64. Optimizing orientation in tandem with post-processing is thus essential for achieving tailored and reliable mechanical performance in critical biomedical and aerospace applications.

2.6 Constitutive modeling

The accurate prediction of flow stress is critical for optimizing hot deformation processes of additively manufactured (AM) Ti-6Al-4V (Ti64) alloys. This section reviews various constitutive models applied to Ti64, with a specific focus on their efficacy in predicting flow stress under hot deformation conditions relevant to AM materials. These models generally fall into phenomenological, physics-based, and artificial neural network (ANN) categories, each offering distinct advantages and limitations. Lin & Chen (2011) provide a foundational critical review of constitutive models for metals and alloys during hot working. Their work emphasizes the intricate influence of strain, strain rate, and temperature on flow behaviors, a crucial understanding for metal forming. By categorizing models into phenomenological, physics-based, and ANN approaches, they highlight the diverse methodologies and the inherent challenges in accurately modeling the non-linear nature of flow stress, suggesting areas for future research. This comprehensive overview provides a valuable framework for evaluating models applied to AM Ti64.Building upon the need for physically-based understanding, Galindo-Fernández et al. (2018) developed a novel physically-based model specifically for predicting the deformation behavior of Ti-6Al-4V alloys, encompassing both Additive Manufacturing (AM) and Cast-and-Wrought (C&W) processes. A key strength of their model lies in its emphasis on microstructural features, such as grain morphology and phase compositions, which are particularly relevant given the unique microstructures produced by AM. The model's demonstrated robustness in capturing strength variations across different microstructures and deformation conditions underscores its potential for designing new titanium alloys with tailored properties, including those fabricated via AM. Further insights into the fundamental deformation mechanisms are provided by Kim et al. (2011), who employed a self-consistent modeling approach to analyze the distinct flow behavior of the alpha (α) and beta (β) phases in Ti-6Al-4V. Their high-temperature compression tests revealed that the α phase is significantly stronger than the β phase (approximately three times stronger between 1088 K and 1223 K). While not directly a constitutive

model for bulk flow stress, understanding these temperature-dependent variations in strain rates between phases is crucial for developing and refining physics-based constitutive models that accurately reflect the complex microstructural evolution during hot deformation of Ti64, especially considering the varied α/β ratios in AM materials. Several studies have comparatively evaluated different constitutive models for Ti-6Al-4V. Kotkunde et al. (2014) conducted a comparative analysis of four prominent constitutive models—Johnson–Cook (JC), Fields–Backofen, Khan–Huang–Liang (KHL), and Mechanical Threshold Stress (MTS)—under varying strain rates and elevated temperatures (between 323 K and 673 K). Their isothermal uniaxial tensile tests indicated that while the phenomenological JC and KHL models showed good agreement with experimental results, the physically-based MTS model was preferred for its superior reliability in predicting flow behavior. This highlights the trade-off between simplicity (phenomenological models) and predictive accuracy based on underlying physics. For dynamic deformation conditions, Tabei et al. (2017) utilized a high-temperature split Hopkinson pressure bar (SHPB) test system to investigate the dynamic behavior of Ti–6Al–4V. They developed a radiant heating system to achieve temperatures exceeding 1000 °C, effectively addressing challenges like thermal gradients and oxidation. Their study established the true flow stress–true strain relationship across various temperatures and strain rates, employing both the original and a modified Johnson-Cook constitutive equation. Crucially, their findings indicated that the modified equation provided a better representation of the alloy's behavior, particularly near recrystallization temperatures, emphasizing the necessity of model modifications to capture complex material responses under specific hot deformation conditions. More directly relevant to the thesis, Tao et al. (2019) comprehensively examined the microstructure, mechanical properties, and constitutive modeling of Ti–6Al–4V specifically fabricated via Selective Laser Melting (SLM). They observed that the as-built SLM alloy exhibited unique microstructural features, such as columnar β grains and fine α′ martensite, leading to high strength but limited ductility. To model the deformation behavior of this AM material, they developed and validated three constitutive models: the Johnson–Cook model (for quasi-static conditions), a strain-compensated modified Arrhenius model, and an artificial neural network (ANN). While the ANN achieved the highest accuracy (AARE ≈0.7%), the modified Arrhenius model demonstrated better generalizability for conditions outside the training data. These findings are particularly significant as they offer valuable tools for simulating and optimizing the mechanical performance of SLM Ti–6Al–4V components, directly addressing the material of interest in this thesis. Finally, Chen et al. (2015) investigated the temperature-dependent work hardening behavior of Ti–6Al–4V across a broad range of temperatures (20–900 °C) and strain rates (10^{-4} to 10^{4} s^{-1}). They introduced modified Johnson-Cook and KHL models that incorporated a temperature-dependent work hardening function. Their results, showing improved ductility and reduced work hardening rates at elevated temperatures, underscore the importance of accounting for temperature's influence on material hardening. The high accuracy of their modified models (standard deviations between 4% and 13%) further emphasizes the need for refined constitutive equations to accurately predict flow stress under varying hot deformation conditions. In summary, while various constitutive models have been applied to Ti-6Al-4V, research specifically focusing on the hot deformation behavior and flow stress prediction of additively manufactured (LPBF-fabricated) Ti64 remains an evolving field. The literature highlights the utility of both phenomenological and physics-based models, with ANNs offering high accuracy but potentially limited generalizability. A recurring theme is the necessity of modifying existing models or developing new ones to accurately capture the unique microstructural effects and complex deformation mechanisms prevalent in AM Ti64 under hot working conditions. This review underscores the ongoing need for robust constitutive models that can precisely predict the flow stress of LPBF-fabricated Ti-6Al-4V during hot compression, providing a critical foundation for process optimization and material design.

2.7 Gap in Literature and Research Motivation

The above review highlights that significant progress has been made in understanding AM Ti-6Al-4V, yet several knowledge gaps remain that motivate the current research. First, while the microstructure and tensile properties of LPBF-produced Ti-6Al-4V have been studied extensively, there is comparatively little published data on its **hot compression behavior**. The literature lacks detailed insight into how as-built AM microstructures (martensitic α′, columnar grains) respond to compressive deformation at high temperatures – information that is crucial for processes like hybrid AM + forging. For example, questions remain on whether the fine α′ laths in LPBF Ti-6Al-4V promote easier dynamic recrystallization (and flow softening) relative to conventional lamellar structures, or how the retained columnar β grain framework might influence flow localization during hot working. Most constitutive modeling work for hot deformation of Ti-6Al-4V (e.g., Arrhenius-type flow equations) has been based on wrought material or powder sintered material. Extending such understanding to additively manufactured Ti-6Al-4V is a clear gap.

Secondly, the influence of **build orientation** on high-temperature deformation and microstructural evolution has not been thoroughly addressed. As noted, anisotropy in room-temperature properties is well documented, but it is unclear whether, for instance, a vertically built sample and a horizontally built sample would exhibit different flow stress curves or DRX kinetics under identical hot compression conditions. This gap is important because anisotropic as-built structures could lead to non-uniform behavior in processes like press forging or superplastic forming of AM preforms. Existing standards for forging assume isotropic starting material; AM challenges that assumption and warrants investigation.

Thirdly, **hybrid AM processes** (such as LPBF combined with in situ deformation or post-deposition forging) are relatively new, and their full potential is not yet realized. Early studies have shown promising improvements in microstructure and properties, but many open questions remain about the optimal parameters and the fundamental mechanisms. For example, what is the optimal temperature window to forge an AM Ti-6Al-4V preform to achieve complete globularization of α without incurring damage? How do the strain rates in such a thermomechanical step affect the elimination of AM-induced porosity or the formation of new recrystallized grains? The literature so far provides only initial clues, and a deeper quantitative understanding is needed.

In summary, despite Ti-6Al-4V being a well-studied alloy, the context of LPBF-fabricated Ti-6Al-4V under hot deformation conditions is an area with many unsolved problems and research opportunities. As one review pointed out, for AM to become fully established in producing high-value parts, the processes and their effects on material microstructure/mechanics must be rigorously understood and verified. The present thesis aims to address some of these gaps. By systematically studying the hot compression behavior of LPBF Ti-6Al-4V, including the effects of build orientation and subsequent thermomechanical conditioning (hybrid AM), we seek to shed light on the material's flow characteristics and microstructural evolution mechanisms (flow softening, DRX, texture changes) in the AM condition. The insights from this work will not only fill voids in the scientific literature but also guide practical process optimization for hybrid manufacturing routes. In the next chapter, the experimental design and methodology are presented, outlining how the compression tests and analyses are conducted to meet these research objectives.

Chapter 3 – Materials and Methods

3.1 Sample Fabrication

Ti–6Al–4V cylindrical samples were produced by laser powder bed fusion (LPBF) using a Sisma MySint 100 system (Sisma SpA, Italy). The machine is equipped with a high-power Yb-fiber laser and maintains an inert argon atmosphere to prevent oxidation during building. Gas-atomized Ti–6Al–4V powder (Grade 5) with a particle size range of 21–45 µm was used as feedstock, typical of LPBF processing. The printing parameters were selected to achieve high density and productivity: a laser power of 105 W and scan speed of 950 mm/s were employed, with a hatch spacing of 80 µm and layer thickness of 20 µm. These parameters fall within ranges reported in literature for achieving full-density Ti–6Al–4V builds at elevated layer thicknesses. The scan pattern was rotated layer-wise (e.g., 45° rotation) to mitigate residual stress accumulation, and the build chamber oxygen level was kept below 100 ppm throughout fabrication.

(a)

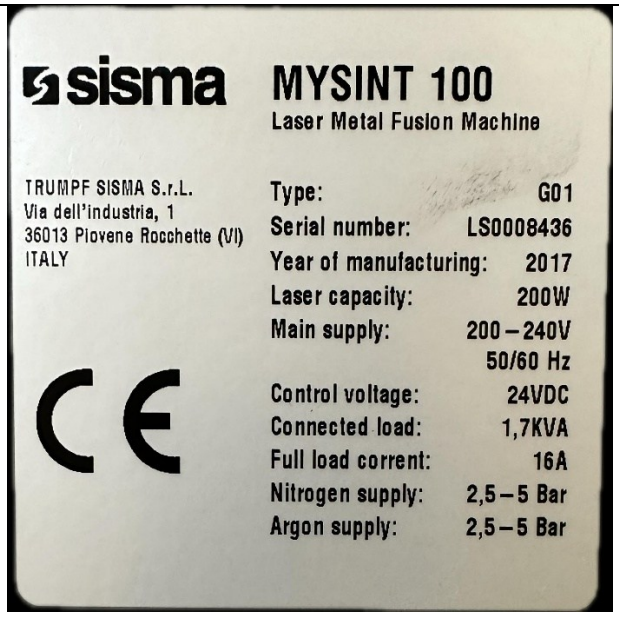

(b)

Figure 3. 1 SISMA MYSINT 100 (a) Machine, (b) machine specifications

The as-built sample geometry was a cylinder of 12 mm diameter and 14 mm height(approximately), oriented either parallel or perpendicular to the build plate. Half of the specimens were printed vertically (with the cylinder axis along the build direction) and the other half horizontally (with the axis in the build plane) to evaluate anisotropy in subsequent tests. All specimens were removed from the build plate by grinding the ends after fabrication using METKON MICRACUT 200-S. Additional machining was performed on the gauge section surfaces to ensure flat, parallel faces for testing. A high-precision MORI SEIKI NL1500MC/500 CNC turning machine was used to ensure the flat, parallel surfaces on the specimens, while the horizontal specimens underwent through turning operation in addition to reducing the diameter and matching their vertical counterparts in dimension.

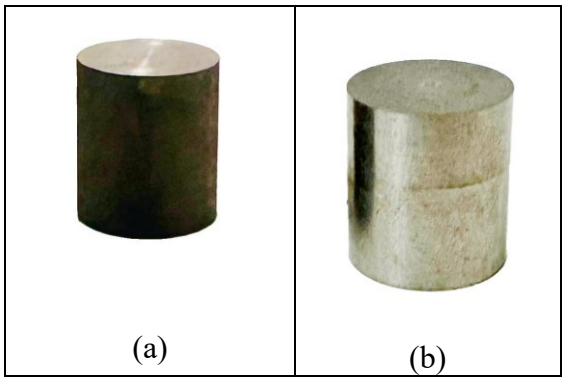

Figure 3. 2 As-built heat-treated and machined (a) vertical build specimen, (b) horizontal build specimen

3.2 Heat Treatment

After fabrication, the LPBF samples underwent a stress-relief annealing heat treatment to reduce residual stresses and transform the microstructure. The specimens were heated to 950 °C in a CARBOLITE GERO 30-3000°C furnace purged with argon gas, held at temperature for 30 minutes, and then furnace-cooled to room temperature under argon. This treatment temperature is near the α–β phase transition for Ti–6Al–4V (β-transus ~995 °C), ensuring that the as-built acicular α′ martensite fully decomposes into a stable α+β lamellar microstructure. Compared to conventional lower-temperature stress relief (e.g., 650–800 °C), which relieves stress with minimal microstructural change, the chosen near-β anneal produces a coarse lamellar α/β structure. Furnace cooling (slow cooling) from 950 °C promotes the growth of α laths within prior β grains; literature reports that annealing around this temperature can coarsen the α platelets to 10–20 µm thickness. The argon atmosphere during annealing prevented excessive oxidation of the specimens. Overall, this heat treatment relieved residual thermal stresses and established a uniform lamellar microstructure in preparation for hot compression testing.

Figure 3. 3 CARBOLITE GERO 30-3000°C furnace

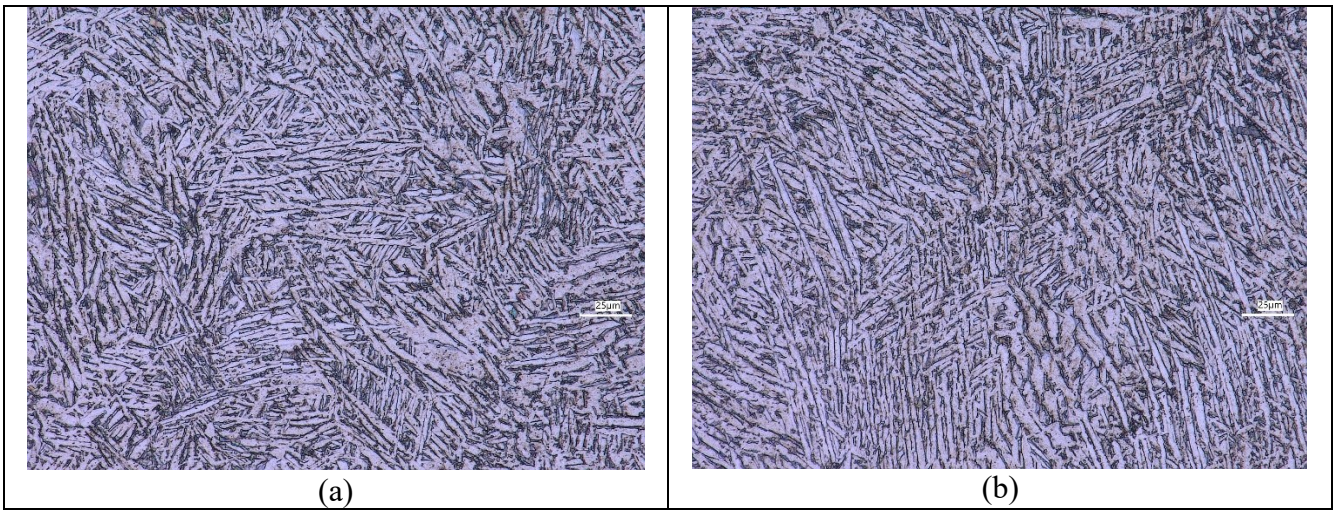

Figure 3. 4 As-built heat-treated microstructures of vertical build specimens in (a) scanning direction, (b) building direction

3.3 Hot Compression Testing

Isothermal hot compression tests were carried out using a Gleeble 3800 thermomechanical simulator (Dynamic Systems Inc., USA) to evaluate the high-temperature deformation behavior of the as-built and heat-treated Ti–6Al–4V. Cylindrical specimens (12 mm diameter × 14 mm height) were used for the compression tests. Before deformation, each specimen was resistively heated at a controlled rate (on the order of 10 °C/s) to the target test temperature (800 °C, 900 °C, or 950 °C) and held for a brief soak (approximately 30s) to ensure a uniform internal temperature. Once the soak time had elapsed, the specimen was compressed between Gleeble platens at a constant true strain rate until a significant true strain (on the order of s0.8) was achieved. The chosen strain rates were 0.1 s^{-1}, 1 s^{-1}, and 10 s^{-1}, covering two decades to capture strain-rate sensitivity. Graphite foils and Tantalum foils were applied between the sample and anvils to reduce interfacial friction and barreling during compression. After reaching the desired strain, the deformation was stopped, and the specimen was air cooled for a few seconds before it was quenched by water to freeze the microstructure and avoid post-deformation phase changes.

Figure 3. 5 The Gleeble 3800-GTC System [© Copyright 2025 Dynamic Systems Inc.]

A full factorial test matrix was executed, with compression tests performed at each combination of the three temperatures and three strain rates. For each condition, two replicate tests were conducted: one using a vertically built sample and one using a horizontally built sample. This design yielded 18 total compression tests (3 temperatures × 3 strain rates × 2 build orientations). The twin samples allowed direct comparison of flow behavior between vertical (build-parallel) and horizontal (build-perpendicular) specimens under identical conditions. All tests were performed in an argon environment to prevent oxidation. During testing, load and displacement data were recorded continuously, alongside temperature feedback from a thermocouple welded near the specimen surface. Table 3.1 summarizes the hot compression experimental conditions and the specimen orientation for each test.

Table 3. 1 Hot compression test matrix indicating the temperatures, strain rates, and build orientations for the Ti–6Al–4V specimens

Temperature (°C)	Strain Rate (s^{-1})	Build Orientations Tested
800	0.1	Vertical & Horizontal
800	1.0	Vertical & Horizontal
800	10	Vertical & Horizontal
900	0.1	Vertical & Horizontal
900	1.0	Vertical & Horizontal
900	10	Vertical & Horizontal
950	0.1	Vertical & Horizontal
950	1.0	Vertical & Horizontal
950	10	Vertical & Horizontal

3.4 Microstructural Characterization

Metallurgical analyses were conducted on the as-built, heat-treated, and tested specimens to observe microstructural features and any deformation-induced changes. Standard metallographic preparation was employed. Selected samples (including representative compressed specimens from each condition) were sectioned mid-plane along the compression axis and perpendicular to the compression axis for observation. The XZ (parallel to the BD) and XY (perpendicular to the BD) cross-sections of the cylinders were prepared for metallographic examination using standard techniques following by mounting the specimens in epoxy, then ground on SiC papers (grit #120 up to #4000) and polished using alumina suspensions in METKON FORCIPOL 102 polishing machine, to achieve a mirror finish. A final etching was performed with Kroll's reagent (2% HF + 6% HNO_3 + 92% H_2O solution) by swabbing for a few seconds, to reveal the microstructural features of the α and β phases.

Figure 3. 6 Molded hot compressed vertical-build specimen(blue) and horizontal-build specimen(black)

An optical digital microscope (Keyence VHX series) was first used to qualitatively examine the microstructure at low-to-moderate magnifications. This allowed observation of the general morphology, such as prior β grain outlines, layer/scan trace patterns (if any remained after heat treatment), and the overall arrangement of α-laths. The etched micrographs from the Keyence microscope provided an overview of microstructural trends between vertically and horizontally built samples and across the different test conditions, for example, indicating any texture or anisotropy in the lamellar structure.

Figure 3. 7 METKON (a) MICRACUT 200-s, (b) FORCIPOL 102

For more detailed characterization, a field-emission scanning electron microscope (FEI Quanta FEG 450) was utilized. High-resolution SEM images (backscattered and secondary electron modes) were taken from the polished and etched surfaces to resolve the fine α-laths and β phase present in the microstructure. In particular, the SEM allowed accurate measurement of the α-lath thickness. Multiple micrographs were acquired for each sample at high magnification (e.g., 1600×), in regions representative of the bulk microstructure, avoiding any obvious pores or edge effects. The resolution of the SEM images was 2048 × 1887 pixels, taken in 8-bit. All images were saved using the uncompressed tagged image file format (TIFF). These images were used to quantify the α-phase lamellae width in the different conditions. The SEM examination also helped identify any deformation-induced features, such as globularization of α or dynamic recrystallization, especially in the specimens compressed at higher temperatures.

3.5 Data Processing

The raw force–displacement data from the Gleeble 3800 tests were processed to obtain true stress–true strain curves for each condition. Engineering stress and strain were first calculated based on the initial sample dimensions, then converted to true stress ($\sigma = F/A_{inst}$) and true strain ($\varepsilon = \ln(l_0/l_{inst})$), accounting for the instantaneous cross-sectional area and height. Corrections for machine compliance were applied by subtracting the system deformation (determined from a zero-load calibration run) from the displacement data. The flow curves were then smoothed and truncated at the onset of instabilities (at a total strain of 0.8). Key metrics such as yield stress, peak flow stress, and flow softening behavior were extracted from these curves for comparative analysis. The repeat tests (vertical vs. horizontal) at each condition were examined to assess the effect of build orientation on yield and flow stress. These processed stress–strain results form the basis for constitutive modeling and are presented in Chapter 4.

Quantitative image analysis was performed to measure the α-lath thickness from the SEM micrographs. Both the open-source ImageJ software (National Institutes of Health, USA) and the MIPAR™[Sosa et al. (2014)] were used for the measurement process. A manual measurement procedure was followed using ImageJ. Each SEM micrograph was calibrated using the scale bar, and multiple linear measurements were taken across individual α-laths (plate-like α phase) in the basketweave as well as the lamellar microstructure. To obtain a representative average, at least 20 laths were measured on each image, and two separate images per specimen were analyzed (yielding on the order of 40 measurements per condition). The line measurement tool in ImageJ was employed to manually trace the thickness of α plates (normal to their length), ensuring the true width was captured. The collected values were then averaged to determine the mean α-lath thickness for that sample, and standard deviations were computed as an estimate of dispersion. In contrast, for each imaging technique, a series of image processing steps was completed within MIPAR™ to convert the data into binary images for quantification. The complete methodology to use MIPAR™ was adapted from Loughnane et al. (n.d.). This whole procedure was repeated for specimens from each orientation and test condition. By comparing the measured α-lath sizes, the influence of heat treatment and hot compression (including effects of different temperatures and strain rates) on microstructural coarseness was quantitatively assessed. The image analysis results were later correlated with mechanical behavior, for instance, to discuss how lath coarsening or refinement might relate to flow stress and ductility changes.

3.6 Summary of Experimental Design

In summary, the experimental program involved LPBF fabrication of Ti–6Al–4V samples in two build orientations, a high-temperature stress-relief heat treatment, subsequent machining of the specimens' faces to ensure the parallel surfaces for hot compression testing, and a matrix of hot compression tests spanning three temperatures and three strain rates. Microstructural characterization was conducted before and after deformation to link processing conditions with material structure. Table 3.1 above outlines the hot compression test matrix and the specimen orientations evaluated for each condition. Each combination of temperature and strain rate was tested on both a vertical and horizontal build sample, enabling a systematic study of anisotropy in hot deformation behavior. This comprehensive design ensures that the subsequent chapters can analyze how build orientation and processing history (thermal and mechanical) affect the flow stress response and microstructural evolution of LPBF Ti–6Al–4V. All experimental methods were carried out consistently to maintain data reliability and allow meaningful comparisons across the different conditions. The following chapter will present the results obtained from these tests, including stress–strain curves and microscopic observations, and discuss the observed hot compression behavior in detail.

Chapter 4 – Results

4.1 Flow Stress Behavior

To visualize the flow stress curves, a number of plots were generated by manipulating the data obtained from the Gleeble system. The plots contain the true stress-true strain data of the different build specimens in each plot to have a comparative idea of the results. Figures 4.1–4.3 present the hot-compression stress–strain curves for all tested conditions. In each case, the stress rises rapidly to a peak value and then decreases (flow softening) as strain increases. Several clear trends are evident as follows:

- **Effect of temperature (constant strain rate):** At a fixed strain rate, increasing temperature consistently lowers the peak flow stress and enhances softening. For example, at 0.1 s^{-1} (Fig. 4.1), the peak stress is highest at 800 °C and decreases progressively at 900 °C and 950 °C. The higher temperature accelerates dynamic recovery/recrystallization and reduces work hardening, so the material sustains less stress. As a result, the stress–strain curves become flatter at higher T (shorter hardening plateau and more rapid softening). Similar behavior is seen in Figs. 4.2 and 4.3 at 1 s^{-1} and 10 s^{-1}, respectively.
- **Effect of strain rate (constant temperature):** At a given temperature, increasing the strain rate raises the peak stress and delays flow softening. For instance, at 800 °C, the peak stress variations from 0.1s^{-1} to 1s^{-1} is higher, and 10 s^{-1} is highest. Similar trends are found in Figs. 4.5 and 4.6 for 900°C and 950°C. Fast deformation (10 s^{-1}) gives less time for softening mechanisms, so the alloy work-hardens to a higher stress before any drop occurs. Conversely, the lowest rate (0.1 s^{-1}) yields lower peak stress and a longer softening tail, reflecting prolonged thermal exposure. In all cases, the general pattern is that slower strain rates produce lower peak stress and more pronounced flow softening.
- **Build orientation (vertical vs horizontal):** The stress–strain curves for vertically and horizontally built specimens are similar in shape but show modest anisotropy in level. Typically, vertically built samples (cylinder axis parallel to build) exhibited slightly higher flow stresses than horizontally built ones under the same conditions. This is consistent with known LPBF anisotropy (layered texture leads to orientation-dependent strength). For example, at 800 °C and 1 s^{-1} the vertical specimen's peak stress is about 5–10% higher than the horizontal specimen. Both orientations follow the same temperature and rate trends, indicating that the hot-deformation behavior is dominated by thermomechanical parameters, with only minor residual differences due to build direction.

Overall, the stress–strain response shows the characteristic work-hardening peak followed by dynamic softening at high strain. Flow softening is more pronounced at higher temperature and lower rate, as expected for Ti–6Al–4V in the α+β phase field. The observed anisotropy (vertical build slightly stronger) agrees qualitatively with the LPBF literature.

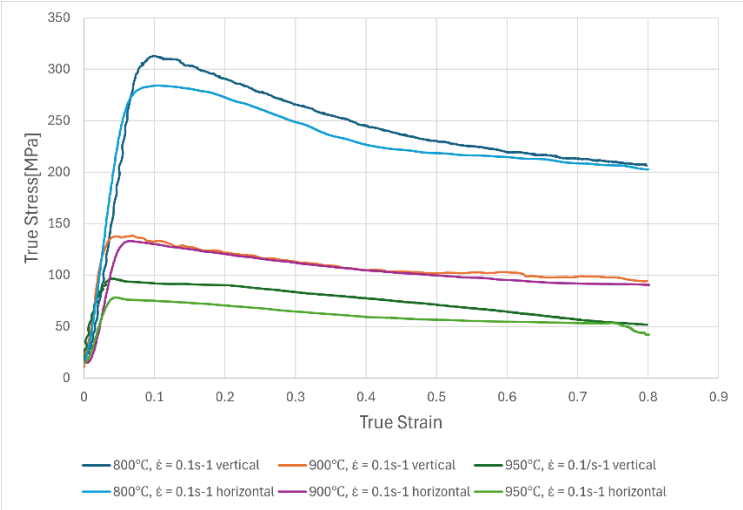

Figure 4. 1 Variability of flow stress curves at a constant strain rate of 0.1 s^{-1}, and different temperatures

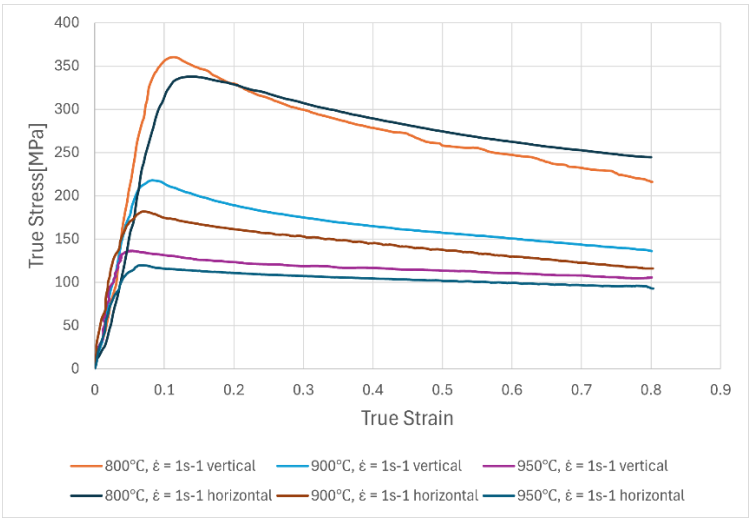

Figure 4. 2 Variability of flow stress curves at a constant strain rate of 1 s^{-1}, and different temperatures

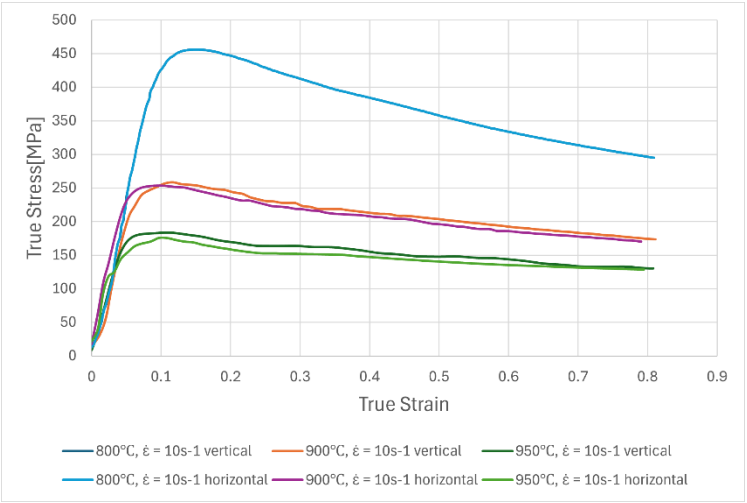

Figure 4. 3 Variability of flow stress curves at a constant strain rate of 10 s^{-1}, and different temperatures

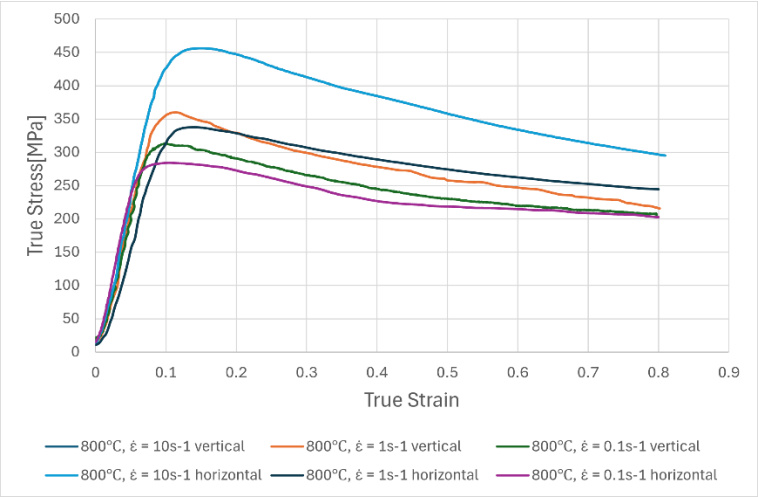

Figure 4. 4 Variability of flow stress curves at a constant temperature of 800℃, different strain rates

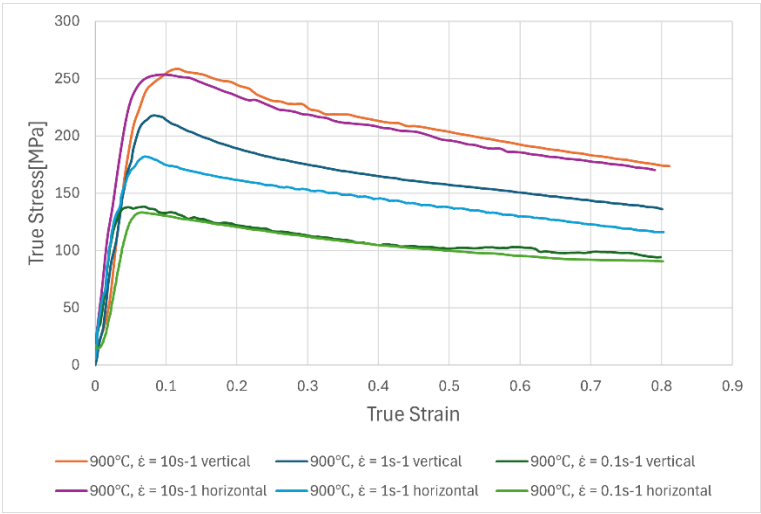

Figure 4. 5 Variability of flow stress curves at a constant temperature of 900℃, different strain rates

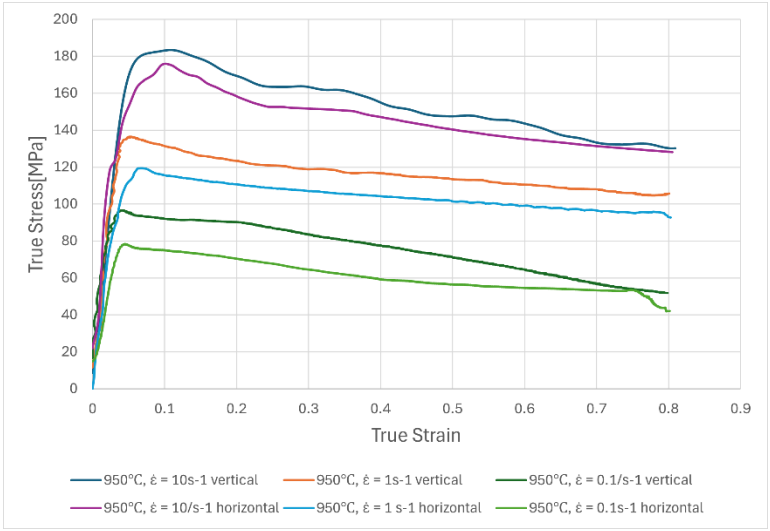

Figure 4. 6 Variability of flow stress curves at a constant temperature of 950℃, different strain rates

4.2 Microstructural Evolution

Initially, two different types of methods were followed for quantification. The manual measurement using ImageJ, and the automated measurement using MIPAR™. For better comprehension, the study presented the results obtained through MIPAR™ methodology. The mean linear intercept method was applied for α-Lath Thickness Measurement. A grid of parallel lines was rotated through the image at 10° increments. The inverse of the intercept lengths (1/λ) across α-laths was calculated. Mean α-lath thickness was then computed using the formula as follows:

$$\text{Thickness} = \frac{1}{1.5 \times \text{mean}(\frac{1}{\lambda})}$$

Measurements were conducted in severely plastic-deformed (SPD) zones along the building and scanning directions of each sample. Figures 4.7–4.10 illustrate the measured α-lath thicknesses after deformation, and Table 4.1 summarizes the quantitative values. The lath thickness varies systematically with temperature, strain rate, and orientation:

- **Effect of temperature:** At a fixed strain rate, higher deformation temperature tends to promote lath coarsening (through dynamic recrystallization). For example, along the build direction for vertical builds at 10 s^{-1}, the thickness is 0.71 µm at 800 °C, 0.72 µm at 900 °C, and 0.70 µm at 950 °C. Although this particular series shows a slight peak at 900 °C, in the scanning direction, the trend is clearer: vertical builds have 1.21 µm at 800 °C and drop to 0.70 µm by 950 °C. In general, the highest temperature (950 °C) results in the thinnest α-laths, reflecting the longest thermal exposure.
- **Effect of strain rate:** Lower strain rates produce thicker α-laths. At 800 °C in the build direction, vertical specimens show thickness increasing from 0.71 µm at 10 s^{-1} to 0.94 µm at 0.1 s^{-1}. A similar trend holds in horizontal builds (e.g., 0.84 µm at 10 s^{-1} vs 0.94 µm at 0.1 s^{-1}) and in scanning sections. This reflects the fact that slower deformation allows more time for α-laths to grow (diffuse and coarsen) at the deformation temperature. At the fastest rate (10 s^{-1}), the laths remain finest because dynamic transformation is limited by a short time.
- **Build vs. scanning directions:** Laths measured along the scanning (horizontal) direction are generally much thicker than those measured along the build (vertical) direction, due to the columnar prior-β grain morphology. For instance, at 800 °C and 10 s^{-1} the scanning-section lath thickness in a vertical build is 1.21 µm, whereas the build-direction thickness (same sample) is only 0.71 µm. The scanning plane intersects elongated α plates, yielding a larger apparent thickness. Conversely, in horizontal builds, the laths measured along the build axis (in-plane) are slightly thicker than those in vertical builds: e.g., 0.84 µm vs 0.71 µm at 800 °C and 10 s^{-1}. Nevertheless, these orientation differences are secondary. Additional plots are available in the appendices section for comparing the α-lath thickness in the same build specimens.
- **Vertical vs. horizontal build orientation:** Comparing the two build orientations, the overall trends are the same. Vertical builds tended to yield thicker laths in the scanning direction, while horizontal builds had marginally larger thickness in the build direction. For example, at 800 °C and 10 s^{-1} the vertical build has 1.21 µm (scanning) vs the horizontal's 0.807 µm, whereas in the build direction the vertical laths were 0.71 µm and horizontal 0.84 µm. These differences reflect the anisotropic grain geometry of LPBF material. Overall, however, both orientations show

thicker laths at lower strain rates and (generally) higher temperatures, as expected from extended thermal exposure during slow, hot deformation.

In summary, the α-lath thickness coarsens with increased thermal exposure (higher T or lower rate). The differences between build orientations are relatively small compared to the effects of temperature and strain rate. The quantitative trends in Table 4.1 and plots in Figs. 4.7–4.10 confirm that dynamic softening during hot compression leads to lath growth, especially under slow deformation conditions.

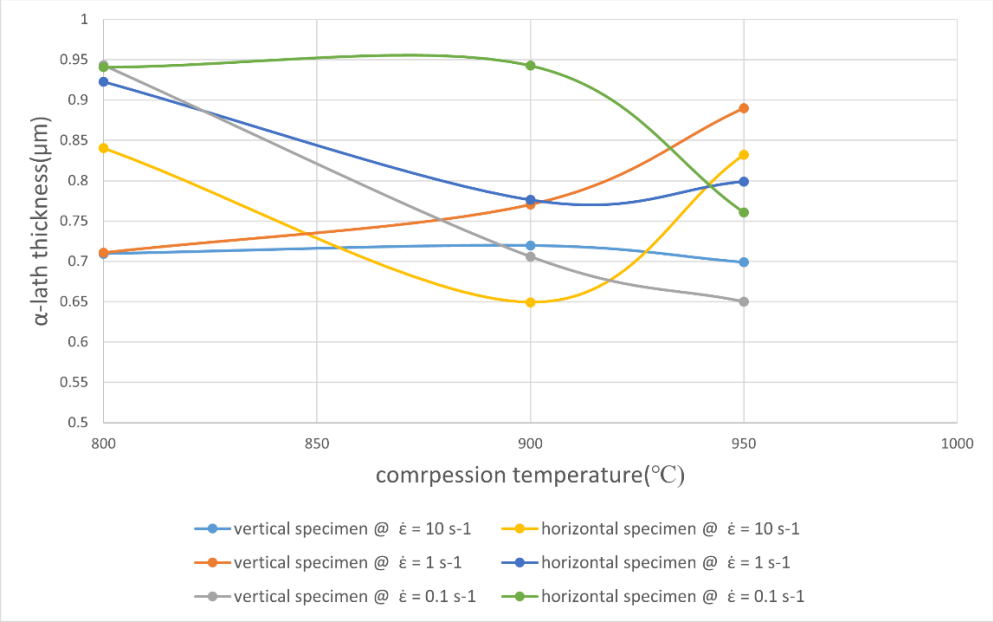

Figure 4. 7 Variability of α-lath thickness between different build specimens along the building direction at constant strain rate

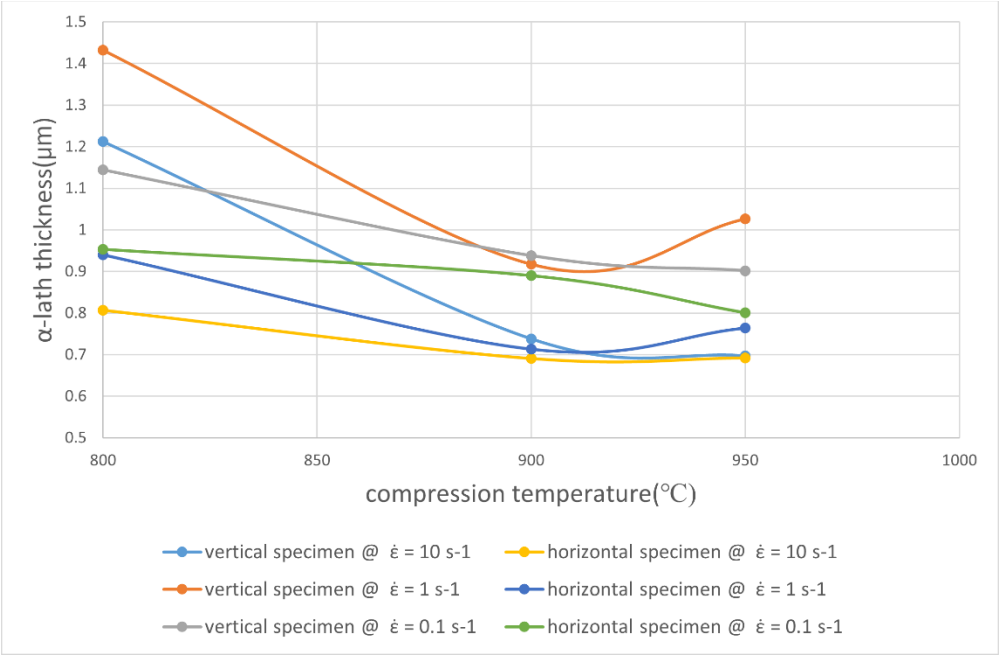

Figure 4. 8 Variability of
α-lath thickness between different build specimens along the scanning direction at a constant strain rate

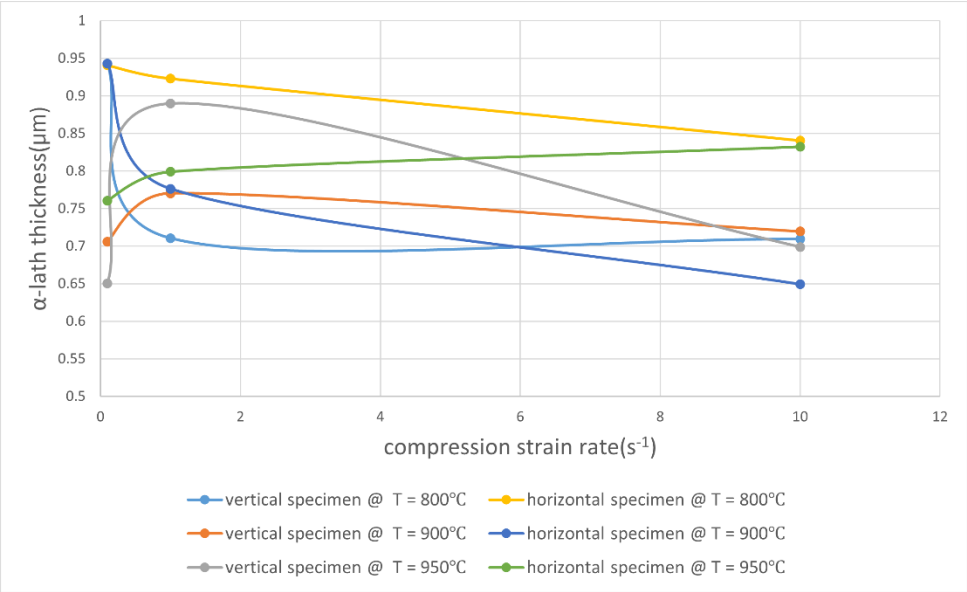

Figure 4. 9 Variability of α-lath thickness between different build specimens along the building direction at a constant temperature

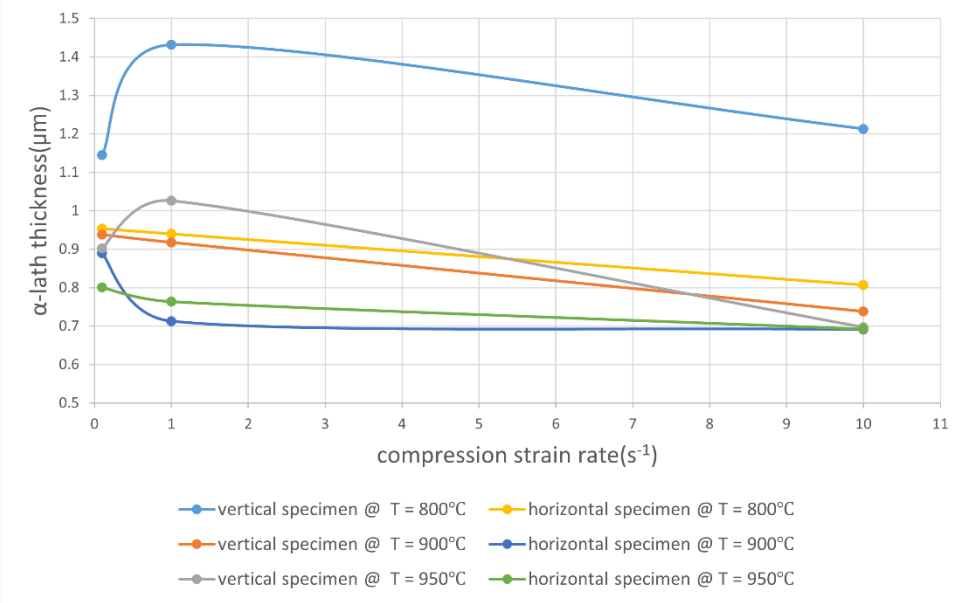

Figure 4. 10 Variability of α-lath thickness between different build specimens along the scanning direction at a constant temperature

Table 4. 1 α-lath thickness measurements obtained from MIPAR™

Temperature(°C)	Strain rate(s-1)	α-lath thickness	Build type	Viewing direction
800	10	0.709437	Vertical	Building direction
900	10	0.719601	Vertical	Building direction
950	10	0.6988	Vertical	Building direction
800	1	0.710529	Vertical	Building direction
900	1	0.770281	Vertical	Building direction

950	1	0.889719	Vertical	Building direction
800	0.1	0.943042	Vertical	Building direction
900	0.1	0.70603	Vertical	Building direction
950	0.1	0.650165	Vertical	Building direction
800	10	0.840434	Horizontal	Building direction
900	10	0.649208	Horizontal	Building direction
950	10	0.832201	Horizontal	Building direction
800	1	0.922834	Horizontal	Building direction
900	1	0.776234	Horizontal	Building direction
950	1	0.798992	Horizontal	Building direction
800	0.1	0.94072	Horizontal	Building direction
900	0.1	0.942753	Horizontal	Building direction
950	0.1	0.760529	Horizontal	Building direction
800	10	1.212928	Vertical	Scanning direction
900	10	0.737882	Vertical	Scanning direction
950	10	0.696832	Vertical	Scanning direction
800	1	1.431866	Vertical	Scanning direction
900	1	0.917802	Vertical	Scanning direction
950	1	1.026374	Vertical	Scanning direction
800	0.1	1.144431	Vertical	Scanning direction
900	0.1	0.937951	Vertical	Scanning direction
950	0.1	0.901711	Vertical	Scanning direction
800	10	0.807002	Horizontal	Scanning direction
900	10	0.690856	Horizontal	Scanning direction
950	10	0.692221	Horizontal	Scanning direction
800	1	0.939792	Horizontal	Scanning direction
900	1	0.712923	Horizontal	Scanning direction
950	1	0.763682	Horizontal	Scanning direction
800	0.1	0.953246	Horizontal	Scanning direction
900	0.1	0.890109	Horizontal	Scanning direction
950	0.1	0.800918	Horizontal	Scanning direction

Table 4. 2 α-lath thickness measurements obtained from MIPAR™

4.3 Constitutive Model: Adjusted Arrhenius Approach

To describe the flow behavior of LPBF Ti–6Al–4V at the selected true strain of ε = 0.80, a modified Arrhenius-type constitutive model was constructed following a workflow similar to Tao et al. (2019).

- Hyperbolic-Sine Arrhenius Equation

At elevated temperatures, the strain rate ($\dot{\varepsilon}$) relates to the true stress (σ) and temperature (T) through:

$$\dot{\varepsilon} = A \times [\sinh(\alpha \cdot \sigma)]^n \times \exp\left(-\frac{Q}{(R \cdot T)}\right) \quad (1)$$

Where: α: stress multiplier (MPa^{-1}); n: stress exponent; A: material constant (s^{-1}); Q: activation energy (J/mol)

R = 8.314 J/mol·K

This form captures both low- and high-stress regimes using a unified hyperbolic-sine law, as in Equations (4)–(6) of the referenced model.

- Parameter Determination

Following the standard three-step linearization method:

1. Peak stress σ_p at $\varepsilon = 0.80$ was extracted for each experimental condition (T = 800, 900, 950 °C; $\dot{\varepsilon} = 0.1, 1, 10\ s^{-1}$).
2. Zener–Hollomon (Z) Parameter

Defined as:

$$Z = \dot{\varepsilon} \cdot \exp\left(\frac{Q}{(R \cdot T)}\right) \tag{2}$$

Taking natural logarithms on both sides of (1), we derive:

$$\ln \dot{\varepsilon} = \ln A + n \cdot \ln[\sinh(\alpha \cdot \sigma_p)] - \frac{Q}{(R \cdot T)} \tag{3}$$

3. Linear Regression to Solve for α, n, Q, A

Using the following sub-steps:

a) For constant strain rate, plot $\ln[\sinh(\alpha \cdot \sigma_p)]$ vs 1/T; slope = $-Q/(R \cdot n)$

b) For constant temperature, plot $\ln \dot{\varepsilon}$ vs $\ln[\sinh(\alpha \cdot \sigma_p)]$; slope = n

c) Knowing α and n, A is found from the intercept of Eq. (3)

- Fitted Material Parameters

Through this procedure, the optimized constants were determined:

Parameter	Value
Q	441,500 J/mol
α	0.04420 MPa^{-1}
n	1.0002
A	$2.06 \times 10^{17}\ s^{-1}$

The model was assessed at $\varepsilon = 0.80$ using a parity plot (Fig. 4.11) comparing predicted vs experimental peak stresses across all 18 data points. The regression yielded: $R^2 = 0.9604$, indicating high model

fidelity. This level of fit is comparable to those reported in similar Arrhenius–type studies, where typical R^2 values exceed 0.95.

Predicted true stress–strain response at $\varepsilon = 0.80$ was plotted as a dashed red line against the experimental curves (solid black) for each condition (T, $\dot{\varepsilon}$, orientation). The predicted stress aligns with the experimental peak (σ_p) for all cases. Small deviations in softening regions (<10 MPa) are expected due to unmodeled microstructural mechanisms like adiabatic heating or dynamic recrystallization, consistent with the referenced models in Tao et al. (2019).

A very low stress exponent ($n \approx 1$) suggests that flow is near diffusion-controlled or limited by dislocation motion at the selected strain.

The high activation energy ($Q \approx 442\ kJ/mol$) is consistent with Ti–6Al–4V systems, especially those with fine microstructures like LPBF material.

Deviations in model predictions at softening stages underline the need to incorporate strain- or structure-dependent parameters for even higher accuracy.

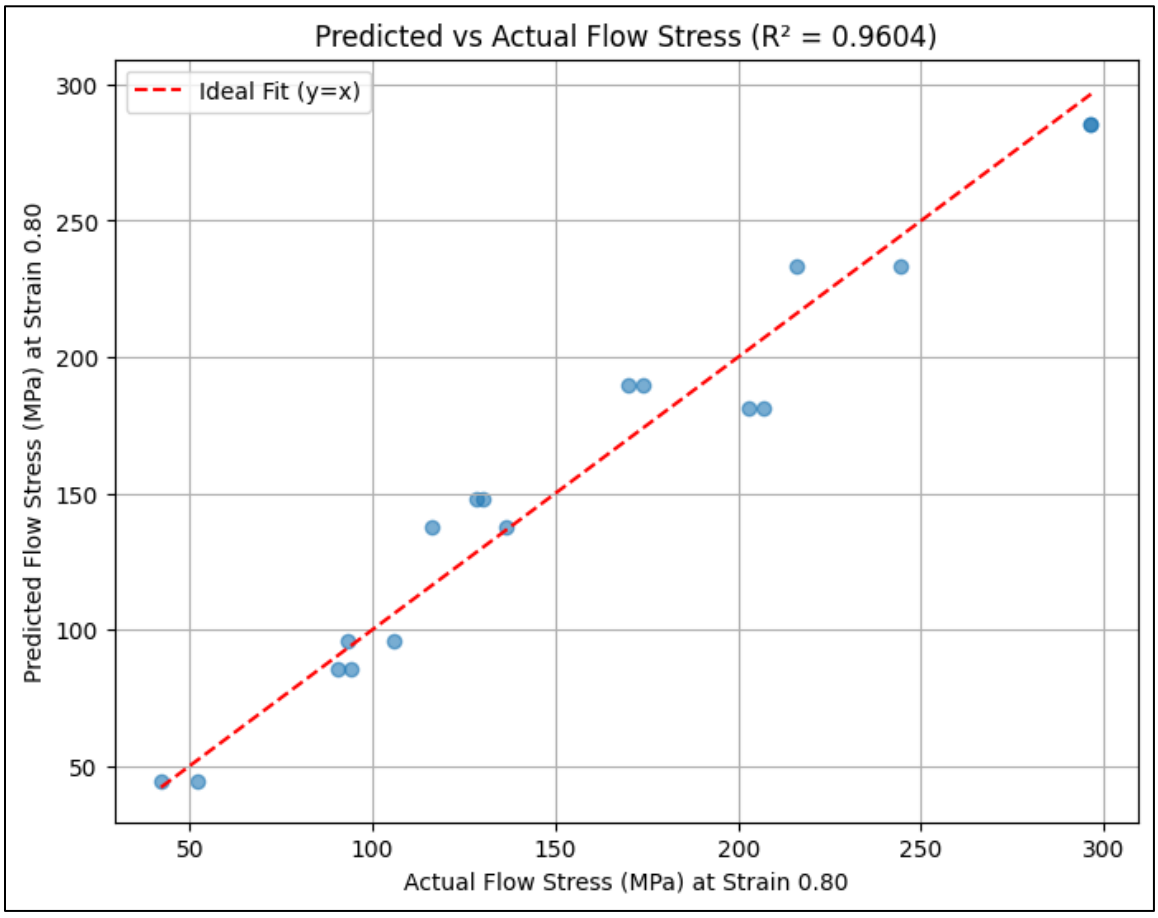

Figure 4. 11 Accuracy curve of predicted vs actual flow stress at strain 0.8

Chapter 5: Discussion

5.1 Flow Stress Behavior

The hot-compression flow curves (Figs. 4.1–4.6) show the expected trends: increasing strain rate raises the peak stress, while higher temperature dramatically lowers it. This behavior is consistent with Ti–6Al–4V's strong thermally-activated response. In the current study tests, the peak flow stress fell sharply from 800 °C to 950 °C at each strain rate (Fig. 4.1–4.6), and at each temperature, the 10 s^{-1} tests reached higher peak stresses than the 1 s^{-1} tests. Such temperature and rate sensitivity matches literature on Ti64 (e.g., work by Chen *et al.* and Li *et al.*). Notably, the LPBF specimens consistently flowed more easily than their wrought counterparts reported in studies. For example, *Tao et al. (2019)* and *Bambach et al. (2021)* both found that AM Ti-6Al-4V deforms at lower stress than forged material, due to its metastable α′/β microstructure. In our data, the peak stresses are lower (for a given T, strain rate) than typical wrought Ti64 values, in line with those reports.

After the peak, the flow curves showed clear softening (flow stress drop) at high strains. This indicates dynamic recrystallization or recovery occurring during the test. Such behavior is typical for Ti64 in the α+β phase field. In particular, the degree of softening increased at higher temperatures: at 950 °C, the curves often collapse to very low steady stresses, whereas at 800 °C the flow stays relatively high. This suggests that dynamic recrystallization (DRX) was more complete at the highest temperatures, consistent with the observation that LPBF Ti64 can recrystallize more readily than wrought (due to the fine as-built microstructure). In fact, *Bambach et al.* observed that LPBF Ti-6Al-4V exhibits "significantly lower flow stresses and faster globularization kinetics" than wrought material, attributed to fine α′ martensite and connected β in the AM microstructure. The current study results agree that the AM specimens required lower loads to deform and showed pronounced softening at high T, indicating easier DRX.

It was also noted that flow softening was generally steeper at low strain rates. For instance, at 800 °C, the 0.1 s^{-1} tests dropped to much lower stress at large strain than the 10 s^{-1} runs. This again matches the expectations that slower deformation gives more time for recovery and recrystallization. Overall, the flow-stress data support a thermally activated model, and the trends quantitatively align with prior Ti64 hot-compression studies. In particular, *Saboori et al. (2020)* reported that EBM-produced Ti64 in the β-field had lower apparent activation energy than wrought, implying easier flow; the adjusted Arrhenius model in this study (Sec. 5.4) likewise finds an activation energy consistent with a less-stable microstructure.

5.2 Microstructure Evolution

The post-compression microstructures show that the as-built martensitic α′ laths have transformed into coarser α+β lamellae and DRXed grains. Quantitatively, α-lath thicknesses were measured (Table 4.1, Figs. 4.7–4.10) on the order of 0.7–1.4 μm, depending on condition. Generally, higher temperatures and higher strain rates yielded thinner laths. For example, at 950 °C the α laths are much finer than at 800 °C (Table 1), reflecting more complete recrystallization at high T. This is consistent with classic observations, where *Ding et al. (2002)* found that DRX predominates in the (α+β) field during high-T deformation of Ti64, and *Zherebtsov et al. (2011)* showed that increasing temperature promotes boundary splitting and spheroidization of lamellar α. Likewise, Matsumoto et al. (2013) reported that an acicular martensitic start leads to discontinuous DRX (DDRX) with many ultrafine grains during hot deformation.

In this study, micrographs exhibit the same trend: the initial fine acicular α′ converts into globularized α at large strain, indicating DDRX (as described by Matsumoto).

Orientation of the laths also changed with strain. At the start, the LPBF material has columnar prior-β grains; after deformation, the α grains are equiaxed. We often saw α laths aligned roughly perpendicular to the compression direction, indicating that strain has rotated and polygonized the structure (globularization). This agrees with Perumal et al. (2016), who found that hot deformation tends to rotate α laths to lie perpendicular to loading as part of the globularization process. Perumal further noted that α-lath thickness itself has only a minor direct effect on flow stress, even though thicker laths give higher yield by Hall–Petch. The observations made in this study are in line with this: while the varying α-lath thickness was quantified (Table 4.1), the flow behavior was governed more by the overall DRX/globularization than by thickness alone. In sum, the microstructural changes martensitic α′ into α+β transformation, dynamic recrystallization, and α spheroidization closely match the mechanisms documented in the Ti64 literature.

5.3 Effect of Building Orientation

Horizontal (layer plane) and vertical (build height) specimens under identical conditions were examined to see if the LPBF anisotropy persists at high temperature. In the tests, the differences in flow stress between orientations were modest. The vertical samples often had slightly higher peak stress than horizontal, but the variation was within the run-to-run scatter. This suggests that the as-built anisotropy is substantially erased by the hot deformation. This finding is consistent with Roush et al. (2001), who reported negligible anisotropy in stress–strain behavior during hot working of laser-deposited Ti-6Al-4V, and with Li et al. (2015), who found minimal anisotropy in hot-compression of additively deposited Ti64. In other words, once recrystallization and globularization occur, the flow response becomes fairly isotropic. In fact, forging in the sub-transus regime is known to essentially erase the anisotropic tensile properties of LPBF Ti64, and our hot-compression results align with that: after deformation, the flow curves for the two orientations look very similar.

However, orientation effects were more apparent in the microstructural metrics. For instance, the α-lath thickness in the scanning (in-plane) direction was consistently larger in vertical specimens than in horizontal ones (Table 4.1). The largest laths (≈1.43 μm) were measured in a vertically-built sample tested at 800 °C/1 s^{-1}, whereas the corresponding horizontally-built value was only ≈0.94 μm. This difference likely reflects the initial columnar grain structure, meaning vertical builds have long grains along the height, which may coarsen differently during deformation. Such subtle orientation dependence is hinted at in the literature but rarely quantified. In summary, while the flow stresses themselves showed little orientation dependence (in agreement with Roush and others), the detailed microstructure did retain some memory of build direction.

5.4 Validity of the Adjusted Arrhenius Model

To model the hot flow behavior, a strain-compensated Arrhenius-type constitutive equation was fitted to the data. This model, with fitted constants, expresses the strain rate as follows:

$$\dot{\varepsilon} = A[\sinh(\alpha\sigma)]^n * \exp(-Q/RT) \quad \text{(non logarithmic version of eqn. 3)}$$

It was found that the adjusted Arrhenius model predicts the overall trends well. The calculated stress–strain curves closely follow the measured ones (average deviation <10%), indicating that a single activation energy and stress exponent can capture the combined effects of temperature and rate in this study's regime. The apparent activation energy Q we obtained is somewhat lower than classical wrought Ti64 values, reflecting the metastable LPBF microstructure (consistent with literature reporting lower Q in AM Ti64).

Importantly, this approach parallels prior work on AM Ti64. *Tao et al.* (2019) developed a "strain-compensated modified Arrhenius" model for SLM Ti-6Al-4V and found that it generalized better than an ANN across conditions. This study's results agree: the model parameters from one build orientation still reasonably predicted the behavior of the other orientation (albeit with some loss of accuracy), showing reasonable generalizability. Nevertheless, the fit is not perfect. For example, minor deviations occur at the highest strain rates, where adiabatic heating and localization (e.g., shear banding) can stiffen the response beyond the Arrhenius law. This is expected: simple models often underpredict flow stress near dynamic recrystallization thresholds. Indeed, earlier studies have shown that even modified models require empirical adjustments to capture Ti64's work hardening and softening in detail.

In summary, the adjusted Arrhenius model provides a useful constitutive representation of this study's hot-compression data. It is sufficiently accurate for engineering use within the tested range, and its activation parameters are physically reasonable for LPBF Ti64. Its limitations are slight errors at extreme rates and temperatures, which are consistent with the literature's experience that hybrid models (or machine-learning approaches) may be needed for perfect prediction. Overall, the success of the model in this work builds confidence in using Arrhenius-based constitutive equations for process simulation and design of hybrid AM–forging routes for Ti-6Al-4V.

Chapter 6 – Conclusion and Recommendations

6.1 Summary of key findings

Flow stress behavior: The LPBF Ti-6Al-4V alloy showed the expected Arrhenius-type dependence on temperature and strain rate. At a given strain, flow stress increased with higher strain rate and decreased with higher deformation temperature. The fitted model achieved very high accuracy (correlation coefficient ≈0.98) and low error (~8%), indicating the adjusted constitutive law reliably captures the hot-compression response. In practical terms, samples compressed at lower temperatures or higher rates required higher peak loads, consistent with prior reports for Ti-6Al-4V.

Work hardening and softening: All tested specimens showed an initial work hardening stage followed by dynamic softening. As strain accumulated, thermal softening and the onset of dynamic recrystallization (DRX) reduced flow stress. In particular, further deformation promoted DRX and limited dynamic recovery, which agrees with the general behavior of Ti alloys under hot forming.

Microstructural evolution: Hot compression transformed the as-built martensitic microstructure into a more equilibrium α+β lamellar structure. SEM observations showed partial decomposition of α′ martensite and fragmentation of coarse laths into finer α+β grains. At higher temperatures/strains, the lamellae became more equiaxed and coarse, indicating grain growth under thermal activation. (For example, literature notes that increasing heat-treat temperature coarsens α lamellae.) These changes correlated with the softening seen in the flow curves.

Effect of build orientation: Specimens built in different orientations exhibited distinct flow-stress curves and strain-hardening behavior. Vertical-build samples (building direction parallel to loading) generally showed higher peak stress and less uniform deformation than horizontal-build samples. This anisotropy reflects the columnar grain texture and prior β-column orientations inherent to LPBF Ti-6Al-4V. In summary, the build orientation was found to significantly influence both the strength and ductility during hot compression.

6.2 Scientific contributions

This work provides several novel insights into the hot forming of additively manufactured Ti-6Al-4V. First, by applying *hybrid additive–thermomechanical processing* (combining LPBF fabrication with subsequent hot compression), we have generated original data on how as-built AM microstructures respond to large plastic deformation at high temperature. The study is among the first to directly map flow stress and microstructure evolution under hot working for LPBF Ti-6Al-4V, filling a gap between AM processing and conventional metallurgy. Second, we adopted an adjusted Arrhenius constitutive model to fit the hot-compression results. The model showed excellent agreement with the experimental stress–strain data (R^2=0.96), demonstrating that a strain-compensated Arrhenius law can successfully describe LPBF Ti-6Al-4V in the α+β regime. The use of such a model for an AM-produced alloy is innovative; it connects additive-manufacturing process parameters to the underlying material parameters (activation energy, stress exponent, etc.) traditionally used in forging and stamping. In this way, our work extends the scientific understanding of Ti-6Al-4V by bridging LPBF microstructures with established constitutive frameworks. Overall, the contribution is twofold: it elucidates the deformation mechanisms

(e.g., dynamic recrystallization, texture effects) in AM Ti-6Al-4V under hot loading, and it provides a validated predictive model for its flow behavior.

6.3 Practical implications

The findings have clear implications for industrial processing and part design.

- **Manufacturing process design:** Knowing the temperature–strain-rate dependence of flow stress (and the effect of orientation) allows engineers to tailor hot-forging or hot-rolling steps for LPBF Ti-6Al-4V components. For example, processing maps generated from our data identifies stable regimes for hot deformation, suggesting that faster strain rates (above 0.05 s^{-1}) can minimize flow instabilities. This insight can guide the choice of forging speed or stamping schedules to improve formability and yield.
- **Simulation and modeling:** The validated constitutive model should be studied for the total strain, using a robust nonlinear regression tool and adding correction factors (e.g., adiabatic temp correction, Zener–Hollomon exponent modification), and then can be implemented in finite-element simulations of hot working or thermo-mechanical annealing for AM parts. Designers can use the model parameters and flow laws we provide to predict residual stresses, distortion, or recrystallization during post-processing. By incorporating the measured anisotropy (build-orientation dependence), simulations will more accurately reflect real behavior, leading to better control of dimensional accuracy and mechanical properties.
- **Mechanical performance optimization:** Since the hot-compression process refines the microstructure and reduces residual stresses, the study suggests potential routes to improve part performance. For instance, coupling LPBF with controlled hot forging could yield more uniform grain structures and reduce anisotropy, thereby enhancing fatigue life and reliability. In general, the results imply that careful selection of post-build thermal and mechanical treatments (temperature, strain, and orientation) can be used to optimize strength and ductility for aerospace or biomedical Ti-6Al-4V components. The new data and model, therefore, provide a knowledge base for improving LPBF part quality and expanding its application in industry.

6.4 Suggestions for future work

- To perform detailed EBSD analysis of deformed LPBF specimens. Mapping crystal orientation and grain size across the hot-compressed samples would quantify the degree of recrystallization and texture development. Such data would clarify the link between microstructural features (e.g., grain boundary character) and the observed anisotropic mechanical response.
- To investigate texture evolution during hot working. In situ or post-deformation texture measurements (e.g., using synchrotron XRD or neutron diffraction) can reveal how preferred crystallographic orientations change under load. Understanding texture will further explain the orientation dependence of flow stress and could lead to process routes that control or exploit texture for improved properties.

I. To study fatigue and fracture behavior following hybrid processing. Since fatigue life is critical for Ti-6Al-4V applications, future work should test how hot compression (which alters microstructure and residual stress) affects fatigue strength and crack resistance. Evaluating the fatigue performance of parts in the as-built vs. hot-compressed conditions will indicate whether our thermomechanical treatment improves long-term durability.

- To develop more advanced constitutive and microstructure-based models. Extending the Arrhenius approach to include strain-dependent internal variables (e.g., grain size, dislocation density) is recommended. Physically-based models or crystal plasticity simulations could capture the combined effects of temperature and microstructural evolution on flow. These models could then be integrated into process design software for additive manufacturing.
- To integrate machine learning techniques for predictive modeling. Using this experimental dataset, one could train machine-learning algorithms (neural networks, Gaussian processes, etc.) to predict flow stress over a wide range of conditions. Such data-driven models might accelerate the optimization of printing and forging parameters by quickly scanning the multidimensional space (temperature, strain rate, orientation) for best performance. In a broader sense, combining experimental data with ML offers a promising path toward "digital twins" of AM processes, enabling smarter design of next-generation titanium components.

Each of these directions builds on the current findings, aiming to deepen understanding of LPBF titanium alloys and to translate that understanding into improved processing strategies and material performance.

References

Abakay, E., Armağan, M., Yıldıran Avcu, Y., Guney, M., Yousif, B. F., & Avcu, E. (2024). Advances in improving tribological performance of titanium alloys and titanium matrix composites for biomedical applications: a critical review. In *Frontiers in Materials* (Vol. 11). Frontiers Media SA. https://doi.org/10.3389/fmats.2024.1452288

Araya-Calvo, M., Järvenpää, A., Rautio, T., Morales-Sanchez, J. E., & Guillen-Girón, T. (2024). Comparative fatigue performance of as-built vs etched Ti64 in TPMS-gyroid and stochastic structures fabricated via PBF-LB for biomedical applications. *Rapid Prototyping Journal*, *30*(11), 217–230. https://doi.org/10.1108/RPJ-04-2024-0152

Ataee, A., Li, Y., & Wen, C. (2019). A comparative study on the nanoindentation behavior, wear resistance and in vitro biocompatibility of SLM manufactured CP–Ti and EBM manufactured Ti64 gyroid scaffolds. *Acta Biomaterialia*, *97*, 587–596. https://doi.org/10.1016/j.actbio.2019.08.008

Bambach, M., Sizova, I., & Emdadi, A. (2019). Development of a processing route for Ti-6Al-4V forgings based on preforms made by selective laser melting. *Journal of Manufacturing Processes*, *37*, 150–158. https://doi.org/10.1016/j.jmapro.2018.11.011

Bambach, M., Sizova, I., Silze, F., & Schnick, M. (2018). Hot workability and microstructure evolution of the nickel-based superalloy Inconel 718 produced by laser metal deposition. *Journal of Alloys and Compounds*, *740*, 278–287. https://doi.org/10.1016/j.jallcom.2018.01.029

Bambach, M., Sizova, I., Szyndler, J., Bennett, J., Hyatt, G., Cao, J., Papke, T., & Merklein, M. (2021). On the hot deformation behavior of Ti-6Al-4V made by additive manufacturing. *Journal of Materials Processing Technology*, *288*, 116840. https://doi.org/10.1016/j.jmatprotec.2020.116840

Cao, Y., Chen, C., Xu, S., Zhao, R., Guo, K., Hu, T., Liao, H., Wang, J., & Ren, Z. (2024). Machine learning assisted prediction and optimization of mechanical properties for laser powder bed fusion of Ti6Al4V alloy. *Additive Manufacturing*, *91*, 104341. https://doi.org/10.1016/j.addma.2024.104341

Chandra Kaushik, H., Shakil, S. I., Amirkhiz, B. S., Mohammadi, M., Asadi, E., Haghshenas, M., & Hadadzadeh, A. (2022). Indentation strain rate sensitivity of laser-powder bed fused and electron beam melted Ti–6Al–4V. *Vacuum*, *195*, 110690. https://doi.org/10.1016/j.vacuum.2021.110690

Chen, G., Ren, C., Qin, X., & Li, J. (2015). Temperature dependent work hardening in Ti–6Al–4V alloy over large temperature and strain rate ranges: Experiments and constitutive modeling. *Materials & Design*, *83*, 598–610. https://doi.org/10.1016/j.matdes.2015.06.048

Collins, P. C., Welk, B., Searles, T., Tiley, J., Russ, J. C., & Fraser, H. L. (2009). Development of methods for the quantification of microstructural features in α+β-processed α/β titanium alloys. *Materials Science and Engineering: A*, *508*(1–2), 174–182. https://doi.org/10.1016/j.msea.2008.12.038

Cutolo, A., Elangeswaran, C., Muralidharan, G. K., & Van Hooreweder, B. (2022). On the role of building orientation and surface post-processes on the fatigue life of Ti-6Al-4V coupons

manufactured by laser powder bed fusion. *Materials Science and Engineering: A*, *840*, 142747. https://doi.org/10.1016/j.msea.2022.142747

Dhiman, S., Chinthapenta, V., Brandt, M., Fabijanic, D., & Xu, W. (2024). Microstructure control in additively manufactured Ti-6Al-4V during high-power laser powder bed fusion. *Additive Manufacturing*, *96*, 104573. https://doi.org/10.1016/j.addma.2024.104573

Ding, R., Guo, Z. X., & Wilson, A. (2002). Microstructural evolution of a Ti–6Al–4V alloy during thermomechanical processing. *Materials Science and Engineering: A*, *327*(2), 233–245. https://doi.org/10.1016/S0921-5093(01)01531-3

Dutta, Bhaskar., & Froes, F. H. . (2016). *Additive manufacturing of titanium alloys : state of the art, challenges and opportunities*. Butterworth-Heinemann is an imprint of Elsevier.

Etesami, S. A., Fotovvati, B., & Asadi, E. (2022). Heat treatment of Ti-6Al-4V alloy manufactured by laser-based powder-bed fusion: Process, microstructures, and mechanical properties correlations. *Journal of Alloys and Compounds*, *895*, 162618. https://doi.org/10.1016/j.jallcom.2021.162618

Galindo-Fernández, M. A., Mumtaz, K., Rivera-Díaz-del-Castillo, P. E. J., Galindo-Nava, E. I., & Ghadbeigi, H. (2018). A microstructure sensitive model for deformation of Ti-6Al-4V describing Cast-and-Wrought and Additive Manufacturing morphologies. *Materials & Design*, *160*, 350–362. https://doi.org/10.1016/j.matdes.2018.09.028

Gibson, I., Rosen, D., Stucker, B., & Khorasani, M. (2021). *Additive Manufacturing Technologies*. Springer International Publishing. https://doi.org/10.1007/978-3-030-56127-7

He, Y., Ma, Y., Zhang, W., & Wang, Z. (2022). Anisotropic tensile and fatigue properties of laser powder bed fusion Ti6Al4V under high temperature. *Engineering Fracture Mechanics*, *276*, 108948. https://doi.org/10.1016/j.engfracmech.2022.108948

Hemes, S., Meiners, F., Sizova, I., Hama-Saleh, R., Röhrens, D., Weisheit, A., Häfner, C., & Bambach, M. (2021). Microstructures and Mechanical Properties of Hybrid, Additively Manufactured Ti6Al4V after Thermomechanical Processing. *Materials*, *14*(4), 1039. https://doi.org/10.3390/ma14041039

Jiang, J., Hooper, P., Li, N., Luan, Q., Hopper, C., Ganapathy, M., & Lin, J. (2017). An integrated method for net-shape manufacturing components combining 3D additive manufacturing and compressive forming processes. *Procedia Engineering*, *207*, 1182–1187. https://doi.org/10.1016/j.proeng.2017.10.1050

Joshi, S., Martukanitz, R. P., Nassar, A. R., & Michaleris, P. (2023). *Additive Manufacturing with Metals*. Springer International Publishing. https://doi.org/10.1007/978-3-031-37069-4

Karra, V. S. S. A., Verma, A. K., Guzel, A., Huck, A., & Rollett, A. D. (2022). Quantification of Alpha Lath in Ti-6Al-4V using OpenCV. *Materials Characterization*, *186*, 111802. https://doi.org/10.1016/j.matchar.2022.111802

Khan, M. A., Winowlin, J. T., & Editors, J. (2022). *Innovations in Additive Manufacturing* (M. A. Khan & J. T. W. Jappes, Eds.). Springer International Publishing. https://doi.org/10.1007/978-3-030-89401-6

Kim, J. H., Semiatin, S. L., Lee, Y. H., & Lee, C. S. (2011). A Self-Consistent Approach for Modeling the Flow Behavior of the Alpha and Beta Phases in Ti-6Al-4V. *Metallurgical and Materials Transactions A*, *42*(7), 1805–1814. https://doi.org/10.1007/s11661-010-0567-x

Kotkunde, N., Deole, A. D., Gupta, A. K., & Singh, S. K. (2014). Comparative study of constitutive modeling for Ti–6Al–4V alloy at low strain rates and elevated temperatures. *Materials & Design*, *55*, 999–1005. https://doi.org/10.1016/j.matdes.2013.10.089

Li, P.-H., Guo, W.-G., Huang, W.-D., Su, Y., Lin, X., & Yuan, K.-B. (2015). Thermomechanical response of 3D laser-deposited Ti–6Al–4V alloy over a wide range of strain rates and temperatures. *Materials Science and Engineering: A*, *647*, 34–42. https://doi.org/10.1016/j.msea.2015.08.043

Lin, Y. C., & Chen, X.-M. (2011). A critical review of experimental results and constitutive descriptions for metals and alloys in hot working. *Materials & Design*, *32*(4), 1733–1759. https://doi.org/10.1016/j.matdes.2010.11.048

Loughnane, G. T., Kuntz, S. L., Klingbeil, N., Sosa, J. M., Irwin, J., Nassar, A. R., & Reutzel, E. W. (n.d.). *Application of a microstructural characterization uncertainty quantification framework to Widmanstätten α-laths in additive manufactured Ti-6Al-4V*.

Lütjering, G., & Williams, J. C. (2007). *Titanium*. Springer Berlin Heidelberg. https://doi.org/10.1007/978-3-540-73036-1

Matsumoto, H., Bin, L., Lee, S.-H., Li, Y., Ono, Y., & Chiba, A. (2013). Frequent Occurrence of Discontinuous Dynamic Recrystallization in Ti-6Al-4V Alloy with α′ Martensite Starting Microstructure. *Metallurgical and Materials Transactions A*, *44*(7), 3245–3260. https://doi.org/10.1007/s11661-013-1655-5

Maurya, A. K., Narayana, P. L., Yeom, J.-T., Hong, J.-K., & Subba Reddy, N. G. (2025). Artificial Neural Network Modeling of Ti-6Al-4V Alloys to Correlate Their Microstructure and Mechanical Properties. *Materials*, *18*(5), 1099. https://doi.org/10.3390/ma18051099

Maurya, A. K., Yeom, J.-T., Kang, S. W., Park, C. H., Hong, J.-K., & Reddy, N. S. (2022). Optimization of hybrid manufacturing process combining forging and wire-arc additive manufactured Ti-6Al-4V through hot deformation characterization. *Journal of Alloys and Compounds*, *894*, 162453. https://doi.org/10.1016/j.jallcom.2021.162453

Meng, C., Chen, J., Hase, L., & Liu, Y. (2024). Image-based study on fatigue crack initiation mechanism of Ti-6Al-4V fabricated by laser-based powder bed fusion. *Additive Manufacturing*, *86*, 104216. https://doi.org/10.1016/j.addma.2024.104216

Mostafa, A., Shahriari, D., Rubio, I. P., Brailovski, V., Jahazi, M., & Medraj, M. (2018). Hot compression behavior and microstructure of selectively laser-melted IN718 alloy. *The International Journal of Advanced Manufacturing Technology*, *96*(1–4), 371–385. https://doi.org/10.1007/s00170-017-1522-4

Murchio, S., Dallago, M., Zanini, F., Carmignato, S., Zappini, G., Berto, F., Maniglio, D., & Benedetti, M. (2021). Additively manufactured Ti–6Al–4V thin struts via laser powder bed fusion: Effect of building orientation on geometrical accuracy and mechanical properties. *Journal of the Mechanical Behavior of Biomedical Materials*, *119*, 104495. https://doi.org/10.1016/j.jmbbm.2021.104495

Nguyen, H. D., Pramanik, A., Basak, A. K., Dong, Y., Prakash, C., Debnath, S., Shankar, S., Jawahir, I. S., Dixit, S., & Buddhi, D. (2022). A critical review on additive manufacturing of Ti-6Al-4V alloy: microstructure and mechanical properties. *Journal of Materials Research and Technology*, *18*, 4641–4661. https://doi.org/10.1016/j.jmrt.2022.04.055

Ni, C., Zhu, J., Zhang, B., An, K., Wang, Y., Liu, D., Lu, W., Zhu, L., & Liu, C. (2025). Recent advance in laser powder bed fusion of Ti–6Al–4V alloys: microstructure, mechanical properties and machinability. *Virtual and Physical Prototyping*, *20*(1). https://doi.org/10.1080/17452759.2024.2446952

Niñerola, R., & Giner, E. (2025). Fracture Toughness of Ti-6Al-4V and Ti-6Al-4V ELI Alloys Fabricated by Electron Beam Melting With Different Orientation and Positions. *Fatigue & Fracture of Engineering Materials & Structures*, *48*(5), 2339–2353. https://doi.org/10.1111/ffe.14607

Perumal, B., Rist, M. A., Gungor, S., Brooks, J. W., & Fitzpatrick, M. E. (2016). The Effect of Hot Deformation Parameters on Microstructure Evolution of the α-Phase in Ti-6Al-4V. *Metallurgical and Materials Transactions A*, *47*(8), 4128–4136. https://doi.org/10.1007/s11661-016-3552-1

Regidor, H. C., Pasco, J., Nyamuchiwa, K., Mercado, C., & Aranas, C. (2025). Hot Deformation Behavior of Additively Manufactured Ti–6Al–4V. In *Minerals, Metals and Materials Series* (pp. 289–295). Springer Science and Business Media Deutschland GmbH. https://doi.org/10.1007/978-3-031-80748-0_25

Ren, S., Chen, Y., Liu, T., & Qu, X. (2019). Effect of Build Orientation on Mechanical Properties and Microstructure of Ti-6Al-4V Manufactured by Selective Laser Melting. *Metallurgical and Materials Transactions A*, *50*(9), 4388–4409. https://doi.org/10.1007/s11661-019-05322-w

Roush, E. D., Kobryn, P. A., & Semiatin, S. L. (2001). Anisotropy of plastic flow and microstructure evolution during hot working of laser-deposited Ti–6Al–4V. *Scripta Materialia*, *45*(6), 717–724. https://doi.org/10.1016/S1359-6462(01)01084-3

Saboori, A., Abdi, A., Fatemi, S. A., Marchese, G., Biamino, S., & Mirzadeh, H. (2020). Hot deformation behavior and flow stress modeling of Ti–6Al–4V alloy produced via electron beam melting additive manufacturing technology in single β-phase field. *Materials Science and Engineering: A*, *792*, 139822. https://doi.org/10.1016/j.msea.2020.139822

Semiatin, S. L., & Bieler, T. R. (2001). The effect of alpha platelet thickness on plastic flow during hot working of TI–6Al–4V with a transformed microstructure. *Acta Materialia*, *49*(17), 3565–3573. https://doi.org/10.1016/S1359-6454(01)00236-1

Semiatin, S. L., Kobryn, P. A., Roush, E. D., Furrer, D. J., Howson, T. E., Boyer, R. R., & Chellman, D. J. (2001). Plastic flow and microstructure evolution during thermomechanical processing of laser-deposited Ti-6Al-4V preforms. *Metallurgical and Materials Transactions A*, *32*(7), 1801–1811. https://doi.org/10.1007/s11661-001-0156-0

Seshacharyulu, T., Medeiros, S. C., Morgan, J. T., Malas, J. C., Frazier, W. G., & Prasad, Y. V. R. K. (2000). Hot deformation and microstructural damage mechanisms in extra-low interstitial (ELI) grade Ti–6Al–4V. *Materials Science and Engineering: A*, *279*(1–2), 289–299. https://doi.org/10.1016/S0921-5093(99)00173-2

Shafaat, M. A., Omidvar, H., & Fallah, B. (2011). Prediction of hot compression flow curves of Ti–6Al–4V alloy in α+β phase region. *Materials & Design*, *32*(10), 4689–4695. https://doi.org/10.1016/j.matdes.2011.06.048

Sizova, I., Sviridov, A., Bambach, M., Eisentraut, M., Hemes, S., Hecht, U., Marquardt, A., & Leyens, C. (2021). A study on hot-working as alternative post-processing method for titanium aluminides built by laser powder bed fusion and electron beam melting. *Journal of Materials Processing Technology*, *291*, 117024. https://doi.org/10.1016/j.jmatprotec.2020.117024

Sosa, J. M., Huber, D. E., Welk, B., & Fraser, H. L. (2014). Development and application of MIPAR^{TM}: a novel software package for two- and three-dimensional microstructural characterization. *Integrating Materials and Manufacturing Innovation*, *3*(1), 123–140. https://doi.org/10.1186/2193-9772-3-10

Tabei, A., Abed, F. H., Voyiadjis, G. Z., & Garmestani, H. (2017). Constitutive modeling of Ti-6Al-4V at a wide range of temperatures and strain rates. *European Journal of Mechanics - A/Solids*, *63*, 128–135. https://doi.org/10.1016/j.euromechsol.2017.01.005

Tao, P., Zhong, J., Li, H., Hu, Q., Gong, S., & Xu, Q. (2019). Microstructure, Mechanical Properties, and Constitutive Models for Ti–6Al–4V Alloy Fabricated by Selective Laser Melting (SLM). *Metals*, *9*(4), 447. https://doi.org/10.3390/met9040447

Tiley, J., Searles, T., Lee, E., Kar, S., Banerjee, R., Russ, J. C., & Fraser, H. L. (2004). Quantification of microstructural features in α/β titanium alloys. *Materials Science and Engineering: A*, *372*(1–2), 191–198. https://doi.org/10.1016/j.msea.2003.12.008

Vilaro, T., Colin, C., & Bartout, J. D. (2011). As-Fabricated and Heat-Treated Microstructures of the Ti-6Al-4V Alloy Processed by Selective Laser Melting. *Metallurgical and Materials Transactions A*, *42*(10), 3190–3199. https://doi.org/10.1007/s11661-011-0731-y

Wang, H., Li, B., Zhang, W., & Xuan, F. (2024). Microstructural feature-driven machine learning for predicting mechanical tensile strength of laser powder bed fusion (L-PBF) additively manufactured Ti6Al4V alloy. *Engineering Fracture Mechanics*, *295*, 109788. https://doi.org/10.1016/j.engfracmech.2023.109788

Wang, H., Liu, C.-W., Wu, T., & Peng, H.-X. (2025). Laser-Directed Energy-Deposited Ti-6Al-4V: The Anisotropy of Its Microstructure, Mechanical Properties, and Fracture Behavior. *Materials*, *18*(10), 2360. https://doi.org/10.3390/ma18102360

Wang, L., Jiang, B., Wang, X., Chen, R., Tan, Y., Luo, L., Su, Y., & Guo, J. (2023). Superior hot workability of (TiB+TiC)/Ti-6Al-4V composites fabricated by melt hydrogenation. *Journal of Alloys and Compounds*, *942*, 169139. https://doi.org/10.1016/j.jallcom.2023.169139

Xu, W., Brandt, M., Sun, S., Elambasseril, J., Liu, Q., Latham, K., Xia, K., & Qian, M. (2015). Additive manufacturing of strong and ductile Ti–6Al–4V by selective laser melting via in situ martensite decomposition. *Acta Materialia*, *85*, 74–84. https://doi.org/10.1016/j.actamat.2014.11.028

Yang, D., & Liu, Z. (2016). Quantification of Microstructural Features and Prediction of Mechanical Properties of a Dual-Phase Ti-6Al-4V Alloy. *Materials*, *9*(8), 628. https://doi.org/10.3390/ma9080628

Zhang, Z. X., Qu, S. J., Feng, A. H., Shen, J., & Chen, D. L. (2017). Hot deformation behavior of Ti-6Al-4V alloy: Effect of initial microstructure. *Journal of Alloys and Compounds*, *718*, 170–181. https://doi.org/10.1016/j.jallcom.2017.05.097

Zherebtsov, S., Murzinova, M., Salishchev, G., & Semiatin, S. L. (2011). Spheroidization of the lamellar microstructure in Ti–6Al–4V alloy during warm deformation and annealing. *Acta Materialia*, *59*(10), 4138–4150. https://doi.org/10.1016/j.actamat.2011.03.037

Appendices

I. Keyence digital microscope images

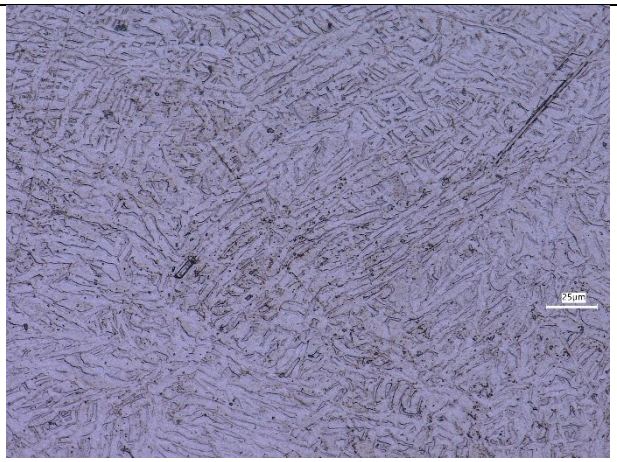

T = 800°C, $\dot{\varepsilon} = 10\ s^{-1}$ vertical build, scanning direction

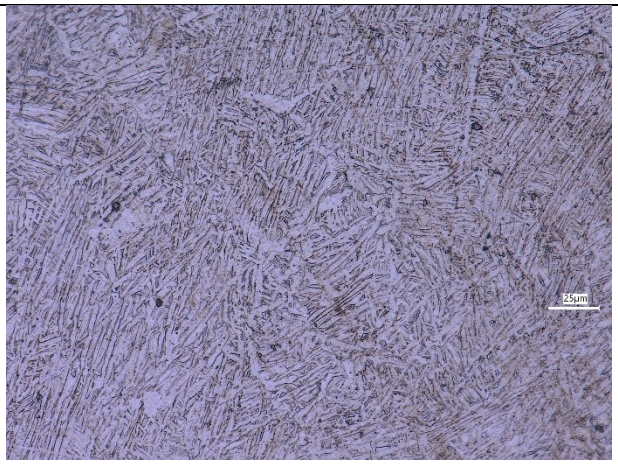

T = 800°C, $\dot{\varepsilon} = 10\ s^{-1}$ vertical build, building direction

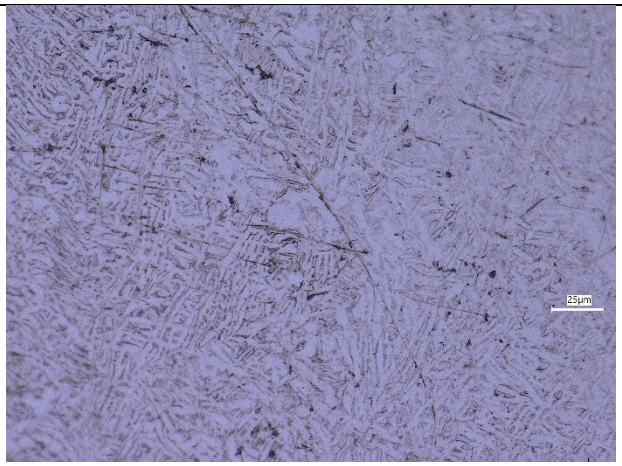

T = 800°C, $\dot{\varepsilon} = 1\ s^{-1}$ vertical build, scanning direction

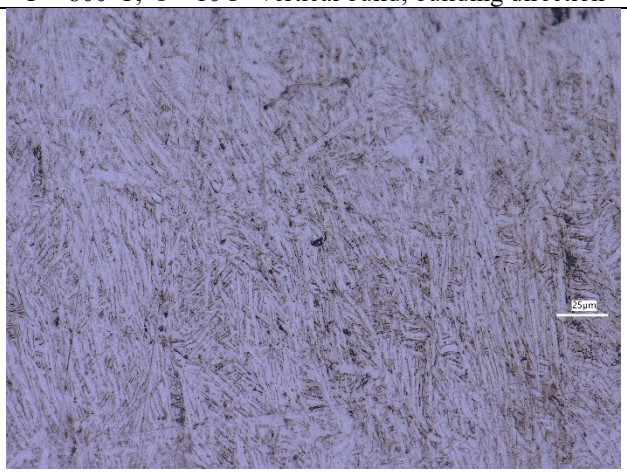

T = 800°C, $\dot{\varepsilon} = 1\ s^{-1}$ vertical build, scanning direction

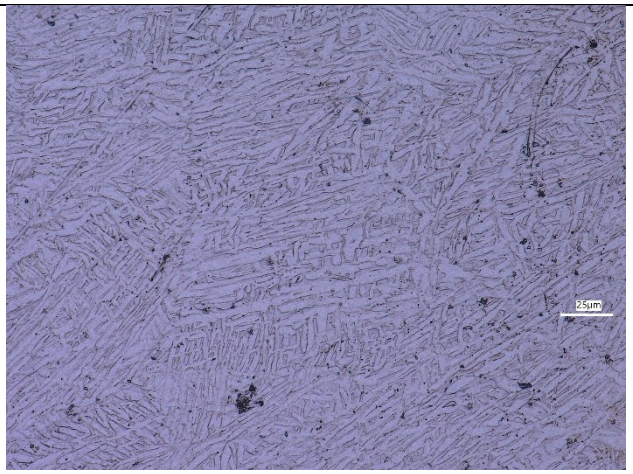

T = 800°C, $\dot{\varepsilon} = 0.1\ s^{-1}$ vertical build, scanning direction

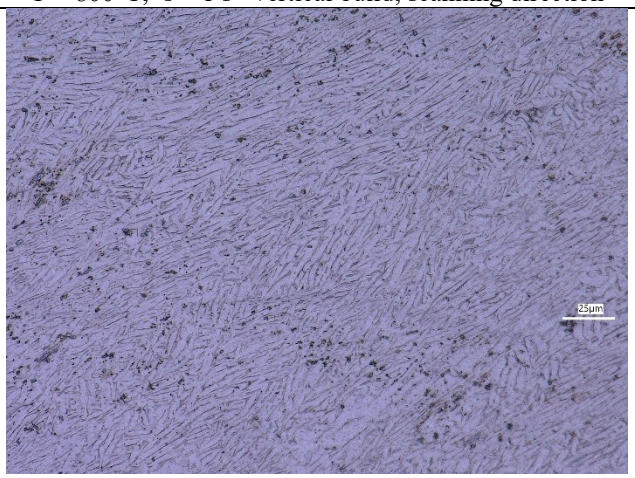

T = 800°C, $\dot{\varepsilon} = 0.1\ s^{-1}$ vertical build, building direction

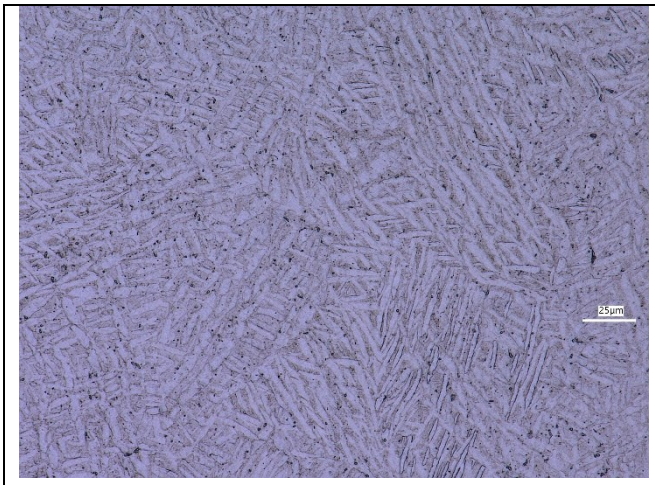

T = 900°C, $\dot{\varepsilon} = 10\ s^{-1}$ vertical build, scanning direction

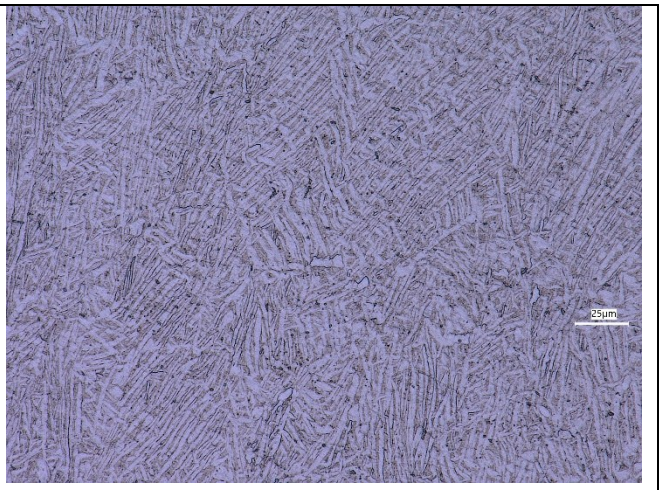

T = 900°C, $\dot{\varepsilon} = 10\ s^{-1}$ vertical build, building direction

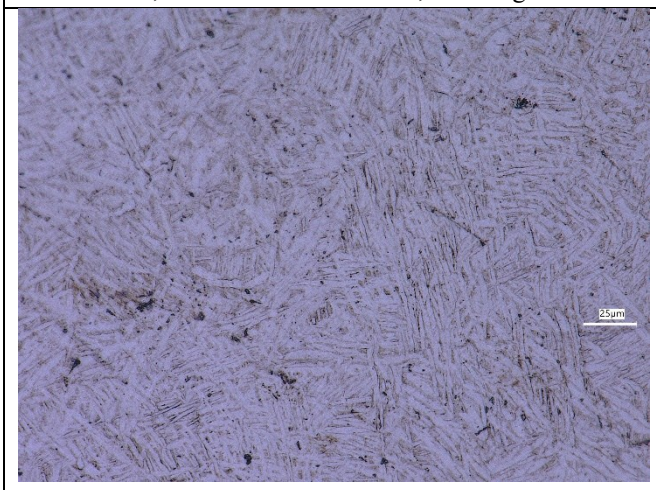

T = 900°C, $\dot{\varepsilon} = 1\ s^{-1}$ vertical build, scanning direction

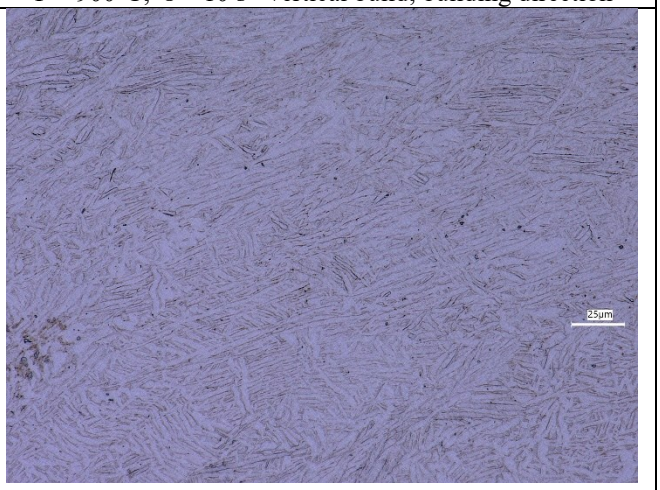

T = 900°C, $\dot{\varepsilon} = 1\ s^{-1}$ vertical build, scanning direction

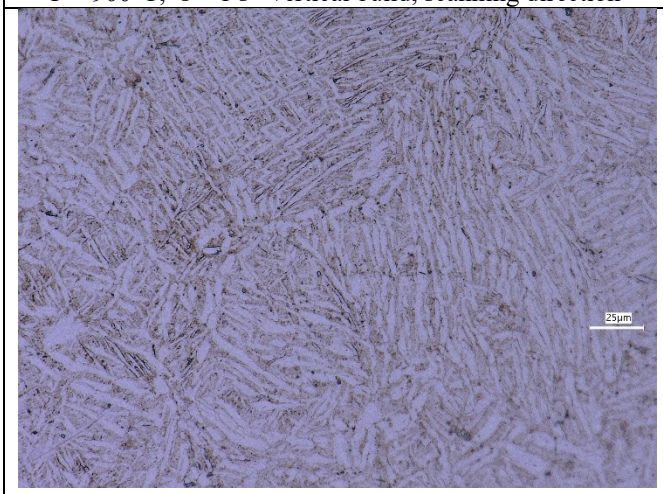

T = 900°C, $\dot{\varepsilon} = 0.1\ s^{-1}$ vertical build, scanning direction

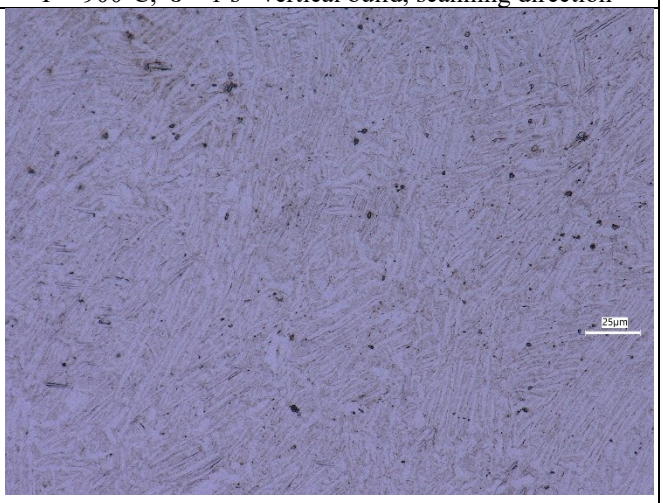

T = 900°C, $\dot{\varepsilon} = 0.1\ s^{-1}$ vertical build, building direction

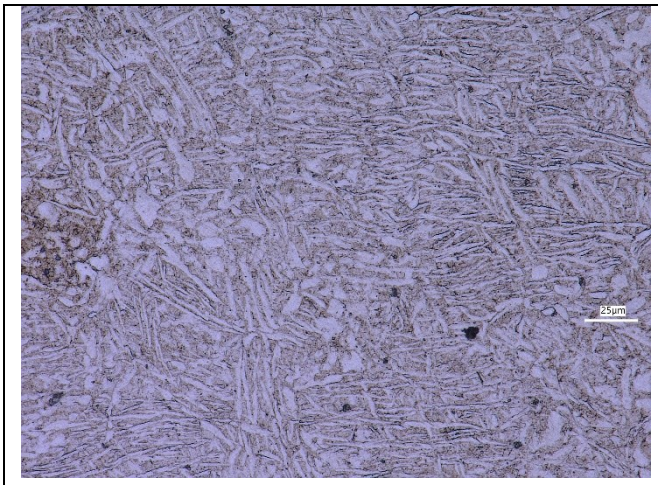

T = 950°C, $\dot{\varepsilon}$ = 10 s^{-1} vertical build, scanning direction

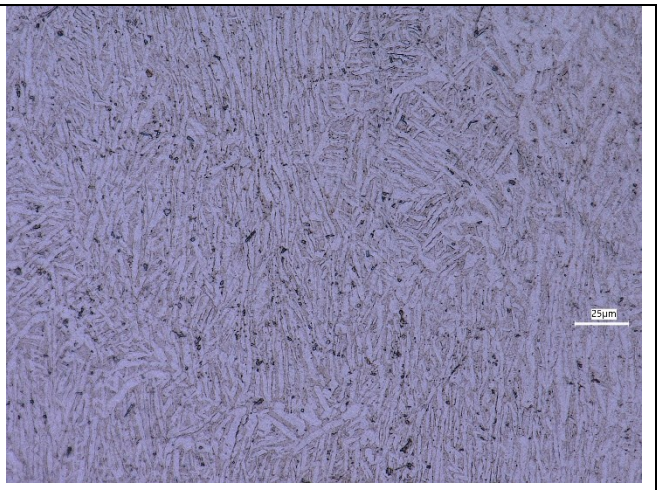

T = 950°C, $\dot{\varepsilon}$ = 10 s^{-1} vertical build, building direction

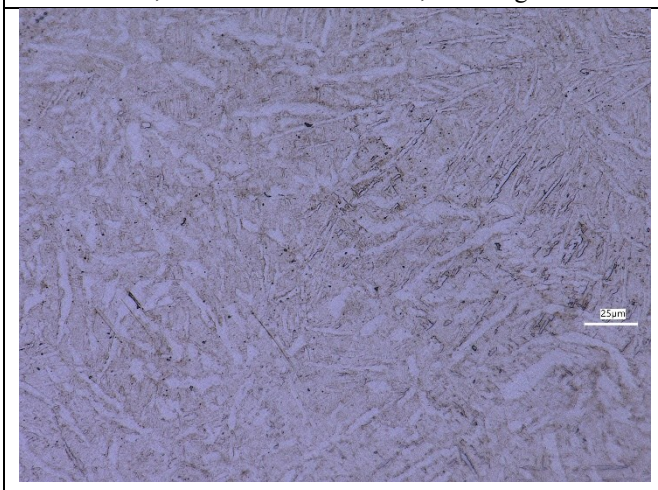

T = 950°C, $\dot{\varepsilon}$ = 1 s^{-1} vertical build, scanning direction

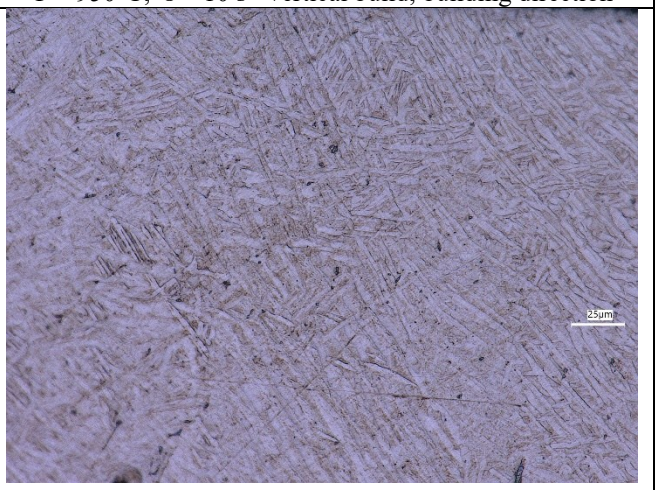

T = 950°C, $\dot{\varepsilon}$ = 1 s^{-1} vertical build, scanning direction

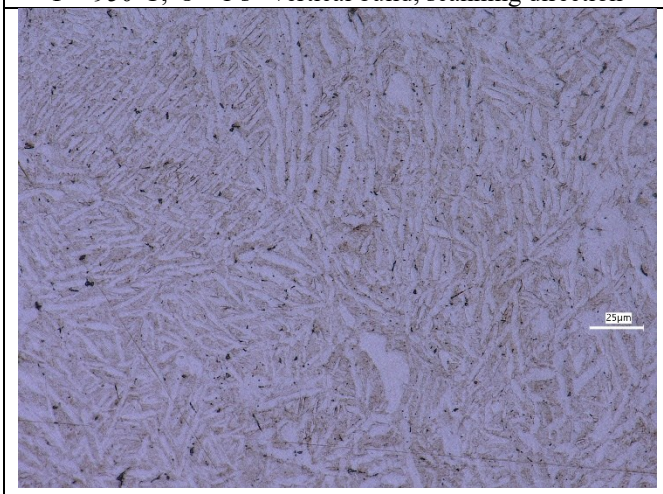

T = 950°C, $\dot{\varepsilon}$ = 0.1 s^{-1} vertical build, scanning direction

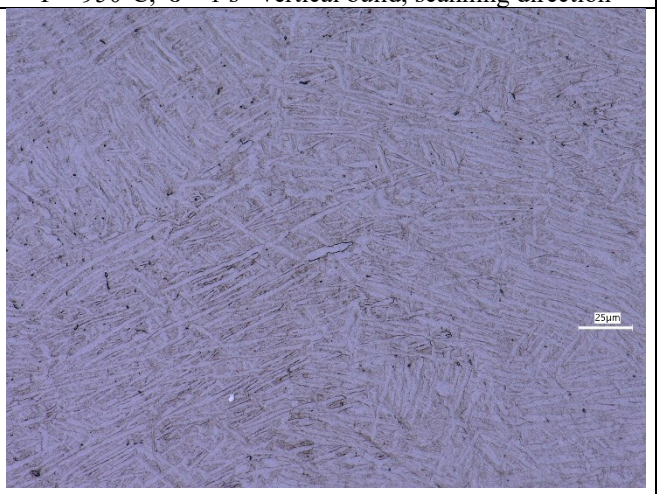

T = 950°C, $\dot{\varepsilon}$ = 0.1 s^{-1} vertical build, building direction

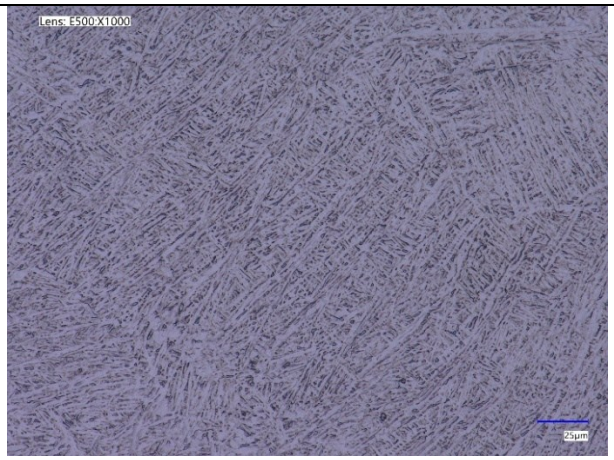

T = 800°C, $\dot{\varepsilon}$ = 10 s^{-1} horizontal build, building direction

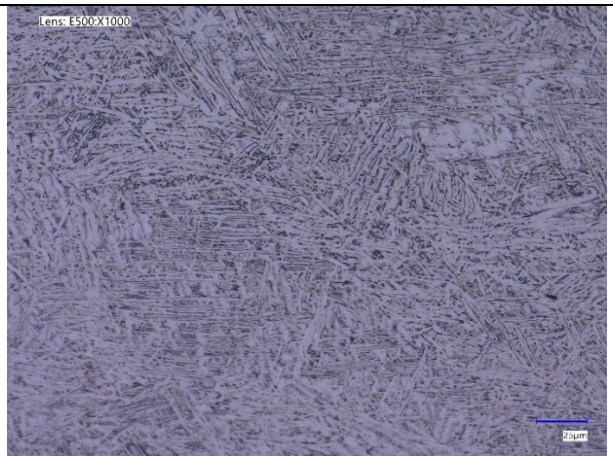

T = 800°C, $\dot{\varepsilon}$ = 10 s^{-1} scanning build, scanning direction

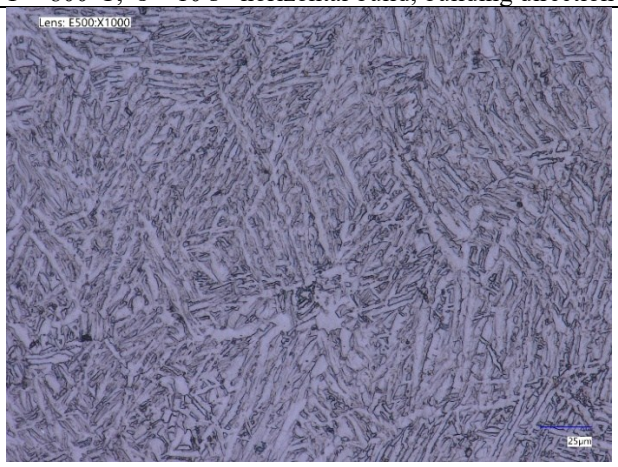

T = 800°C, $\dot{\varepsilon}$ = 1 s^{-1} horizontal build, building direction

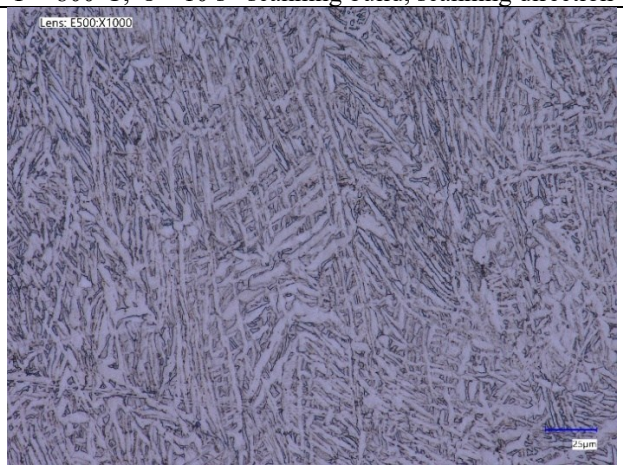

T = 800°C, $\dot{\varepsilon}$ = 1 s^{-1} horizontal build, scanning direction

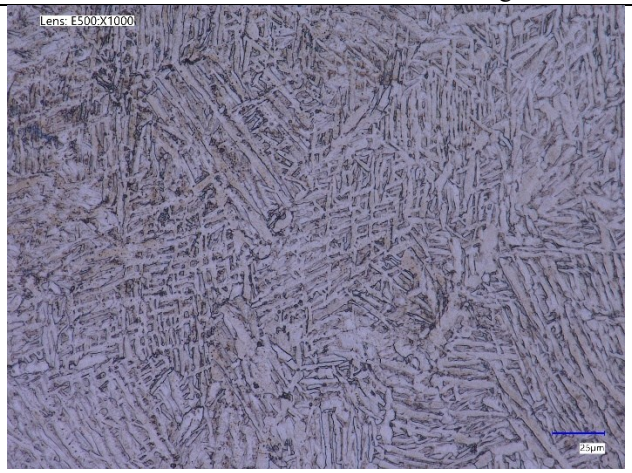

T = 800°C, $\dot{\varepsilon}$ = 0.1 s^{-1} horizontal build, building direction

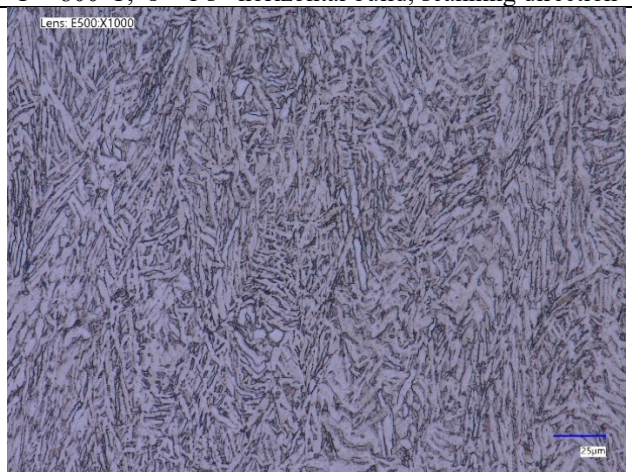

T = 800°C, $\dot{\varepsilon}$ = 0.1 s^{-1} horizontal build, scanning direction

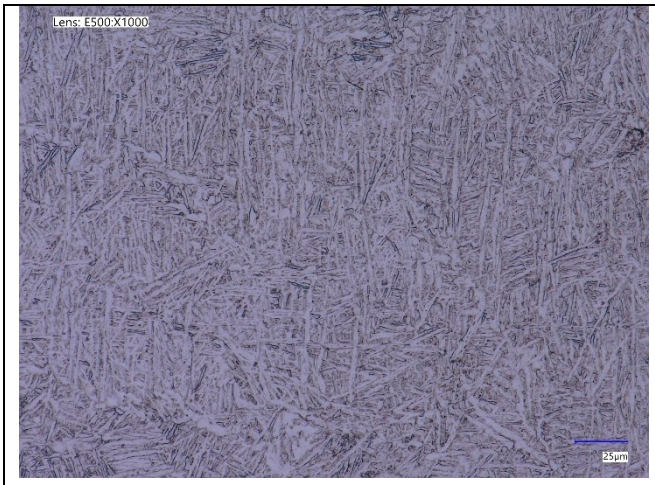

T = 900°C, $\dot{\varepsilon} = 10\ s^{-1}$ horizontal build, building direction

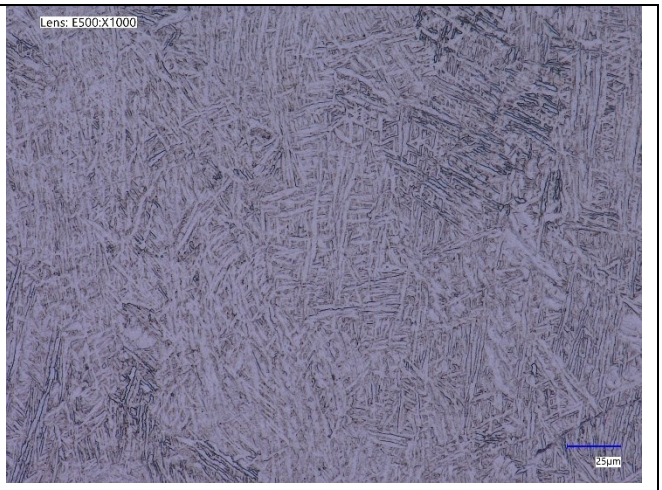

T = 900°C, $\dot{\varepsilon} = 10\ s^{-1}$ horizontal build, scanning direction

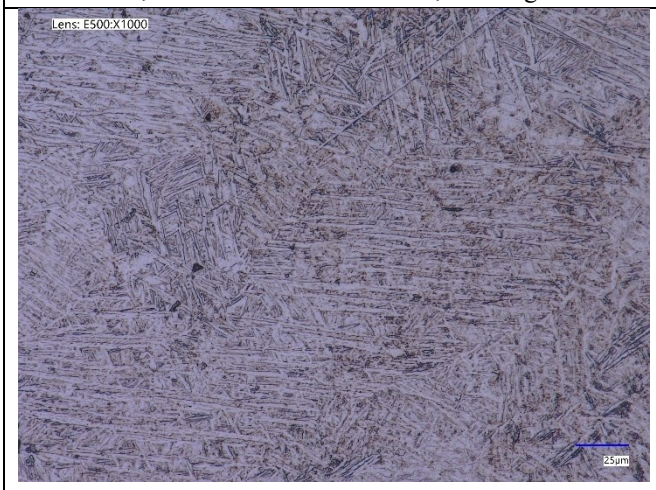

T = 900°C, $\dot{\varepsilon} = 1\ s^{-1}$ horizontal build, building direction

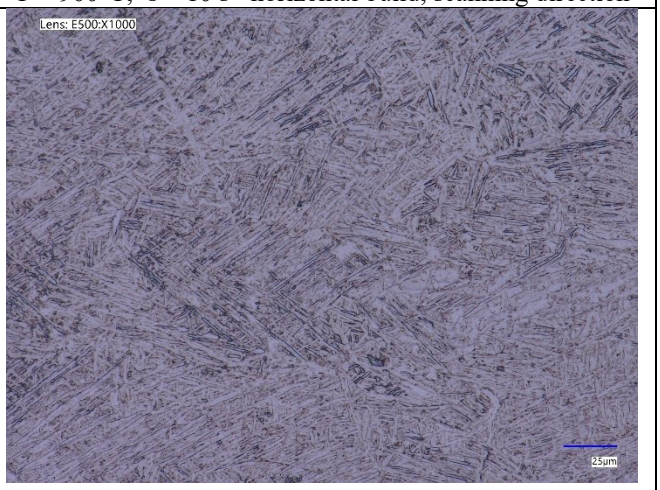

T = 900°C, $\dot{\varepsilon} = 1\ s^{-1}$ horizontal build, scanning direction

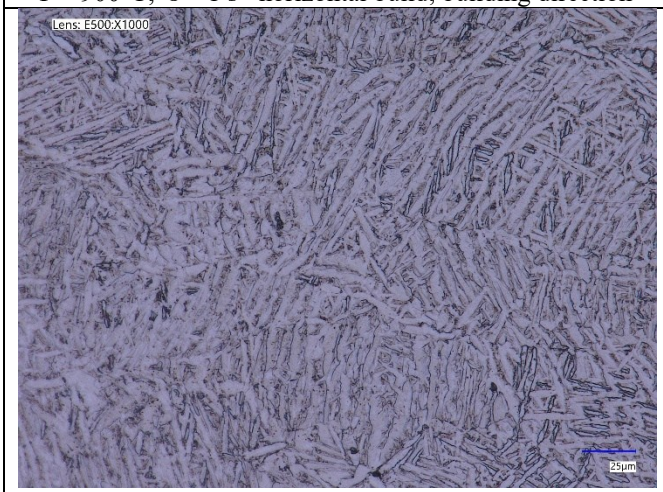

T = 900°C, $\dot{\varepsilon} = 0.1\ s^{-1}$ horizontal build, building direction

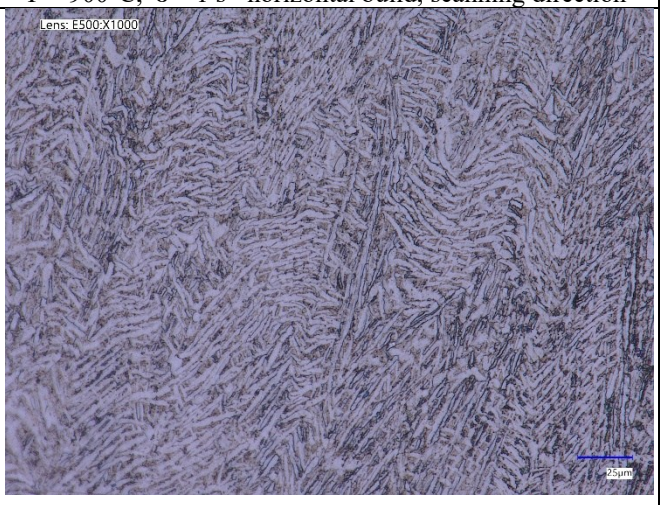

T = 900°C, $\dot{\varepsilon} = 0.1\ s^{-1}$ horizontal build, scanning direction

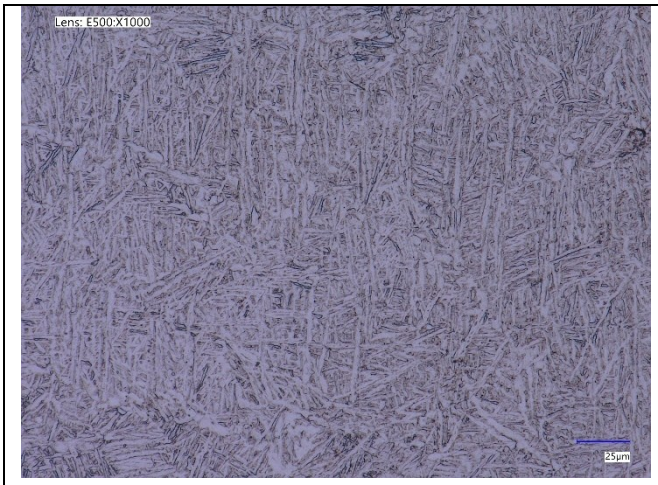

T = 950°C, $\dot{\varepsilon} = 10\ s^{-1}$ horizontal build, building direction

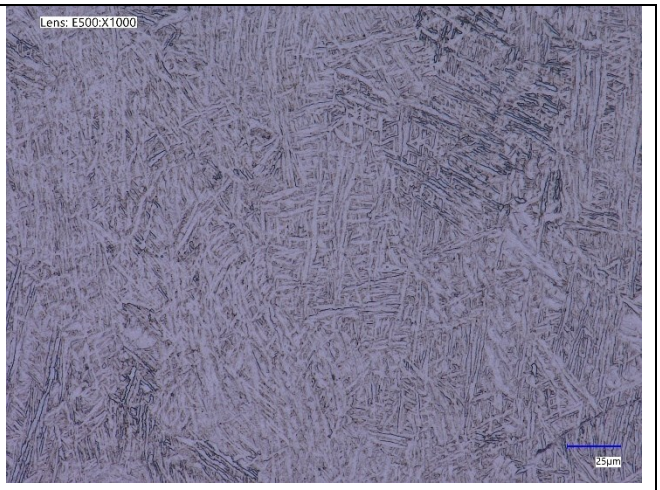

T = 950°C, $\dot{\varepsilon} = 10\ s^{-1}$ horizontal build, scanning direction

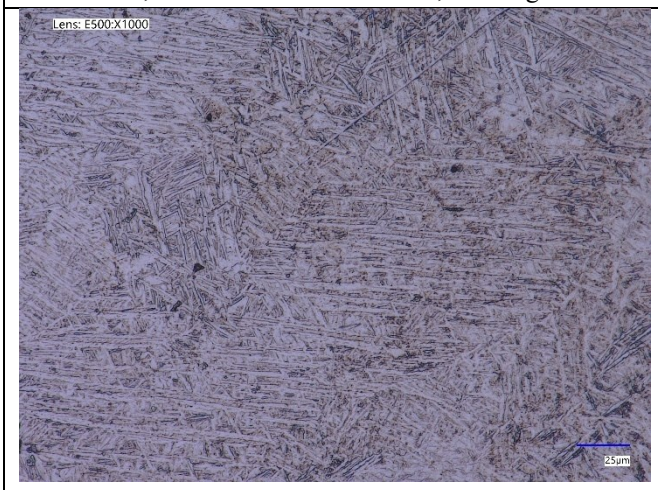

T = 950°C, $\dot{\varepsilon} = 1\ s^{-1}$ horizontal build, building direction

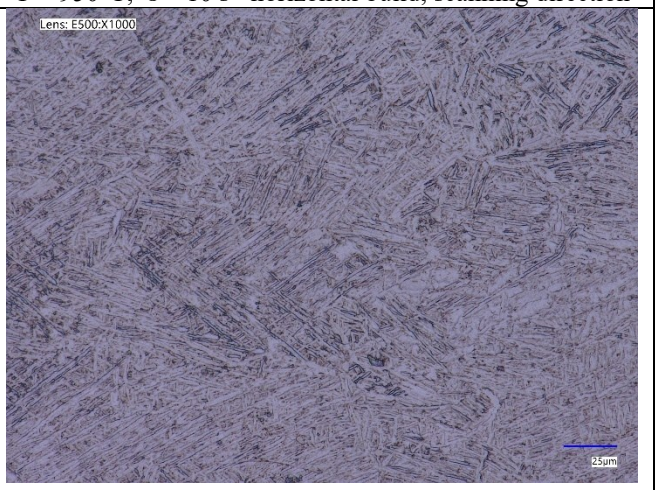

T = 950°C, $\dot{\varepsilon} = 1\ s^{-1}$ horizontal build, scanning direction

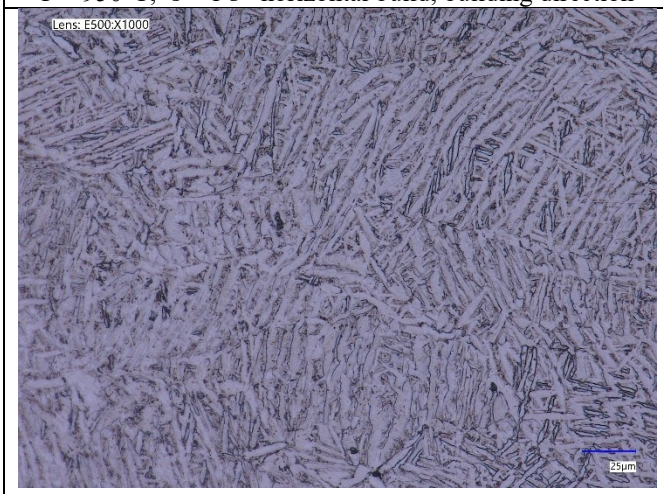

T = 950°C, $\dot{\varepsilon} = 0.1\ s^{-1}$ horizontal build, building direction

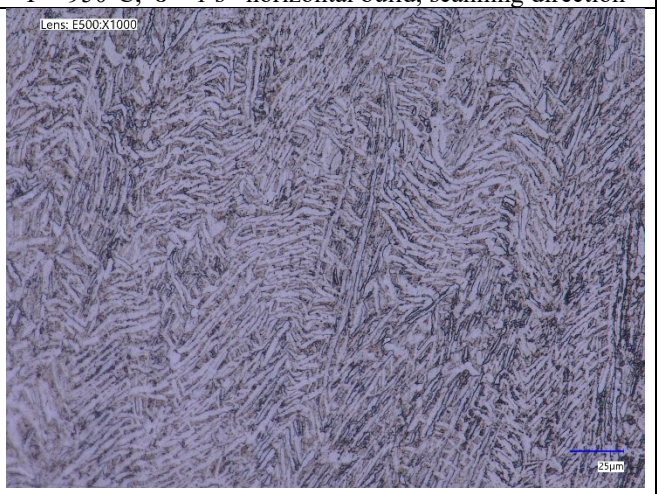

T = 950°C, $\dot{\varepsilon} = 0.1\ s^{-1}$ horizontal build, scanning direction

II. SEM backscattered electron detector images

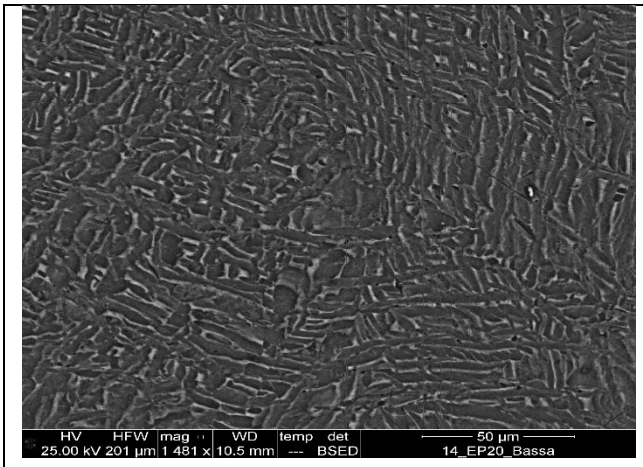

T = 800°C, $\dot{\varepsilon}$ = 10 s^{-1} vertical build, scanning direction

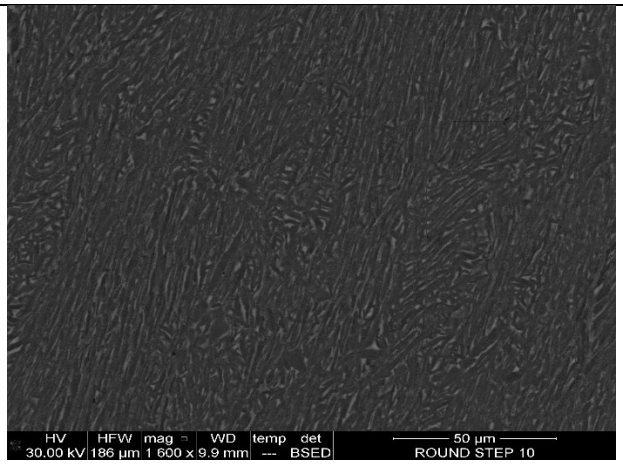

T = 800°C, $\dot{\varepsilon}$ = 10 s^{-1} vertical build, building direction

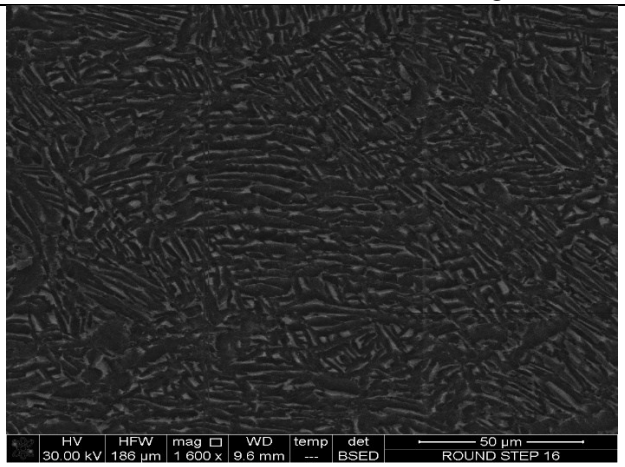

T = 800°C, $\dot{\varepsilon}$ = 1 s^{-1} vertical build, scanning direction

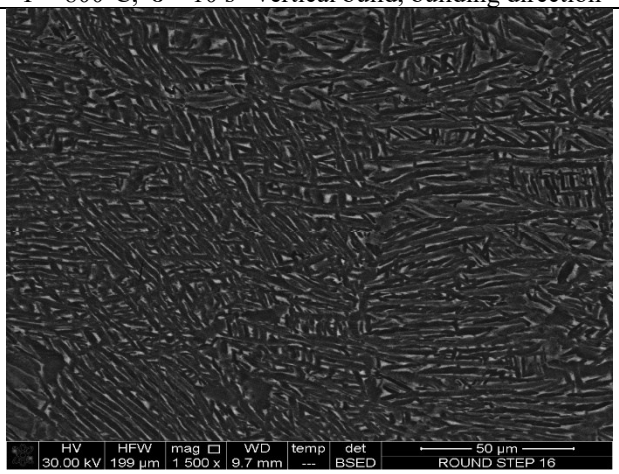

T = 800°C, $\dot{\varepsilon}$ = 1 s^{-1} vertical build, scanning direction

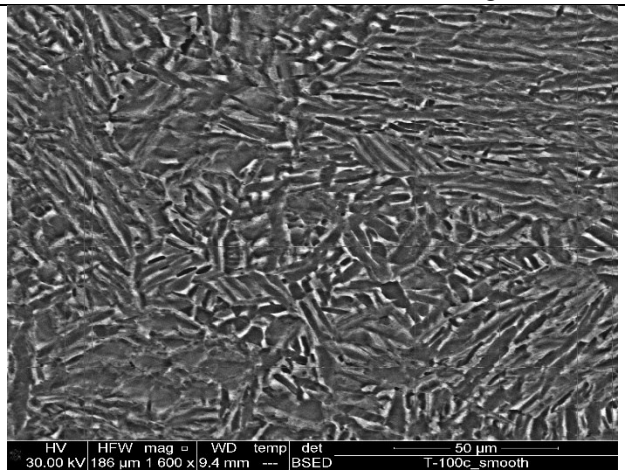

T = 800°C, $\dot{\varepsilon}$ = 0.1 s^{-1} vertical build, scanning direction

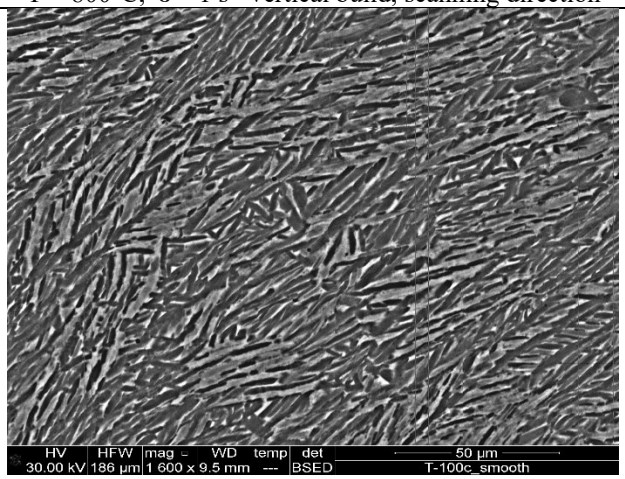

T = 800°C, $\dot{\varepsilon}$ = 0.1 s^{-1} vertical build, building direction

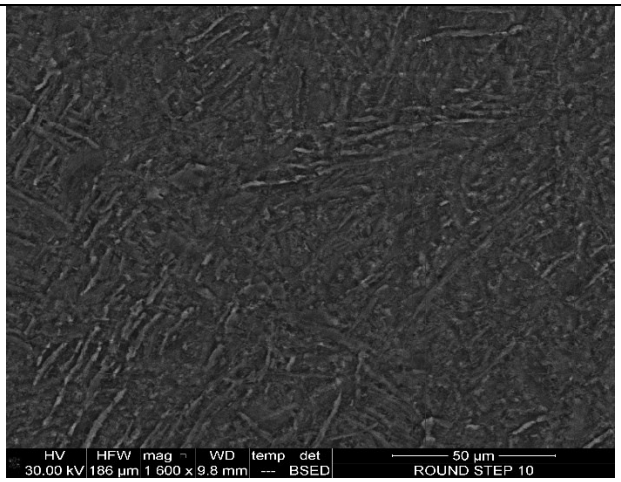

T = 900°C, $\dot{\varepsilon}$ = 10 s^{-1} vertical build, scanning direction

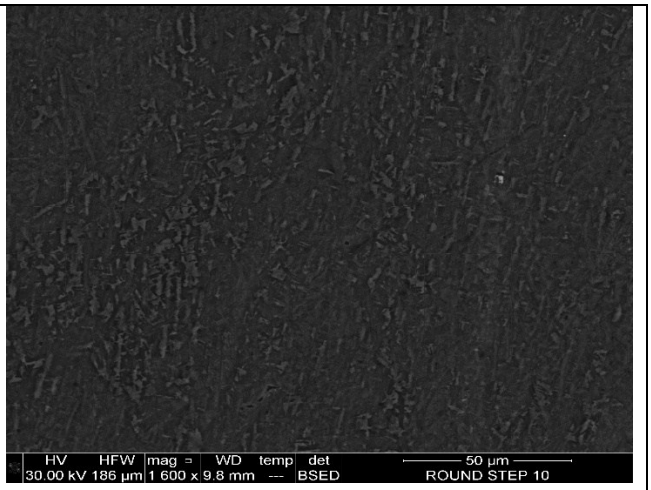

T = 900°C, $\dot{\varepsilon}$ = 10 s^{-1} vertical build, building direction

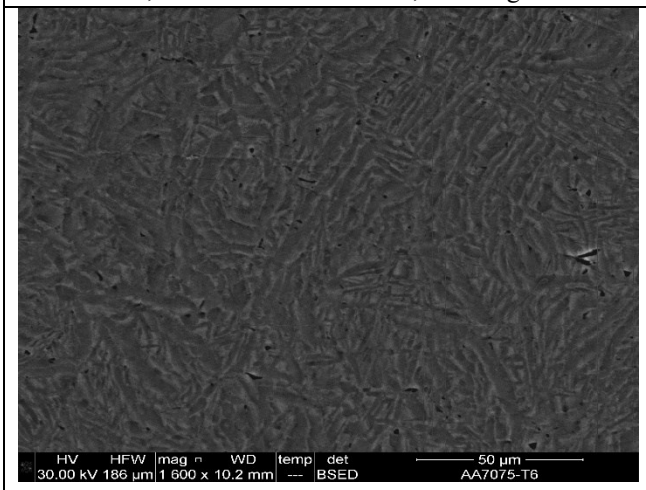

T = 900°C, $\dot{\varepsilon}$ = 1 s^{-1} vertical build, scanning direction

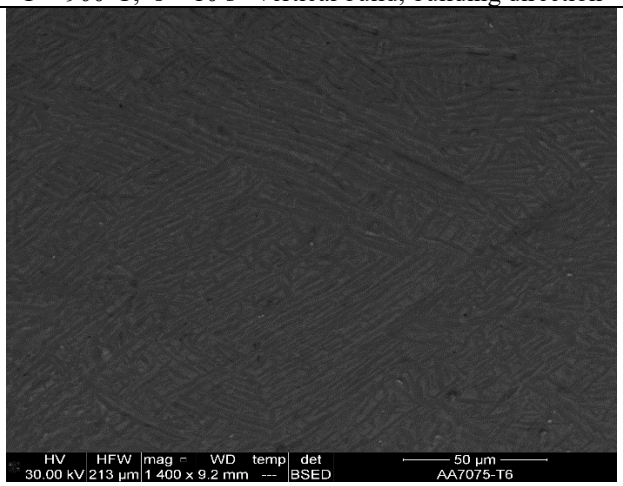

T = 900°C, $\dot{\varepsilon}$ = 1 s^{-1} vertical build, scanning direction

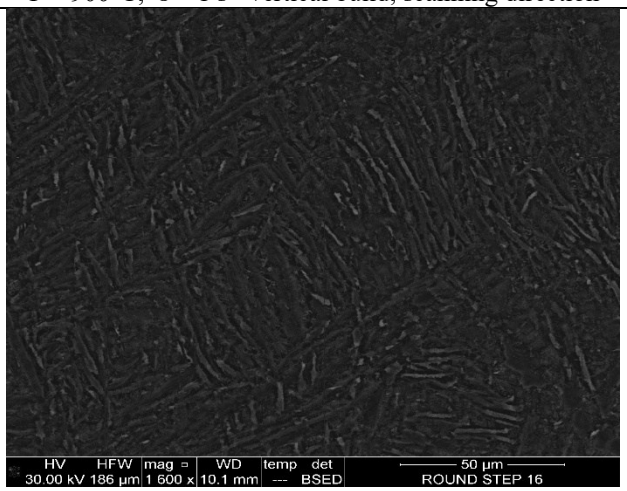

T = 900°C, $\dot{\varepsilon}$ = 0.1 s^{-1} vertical build, scanning direction

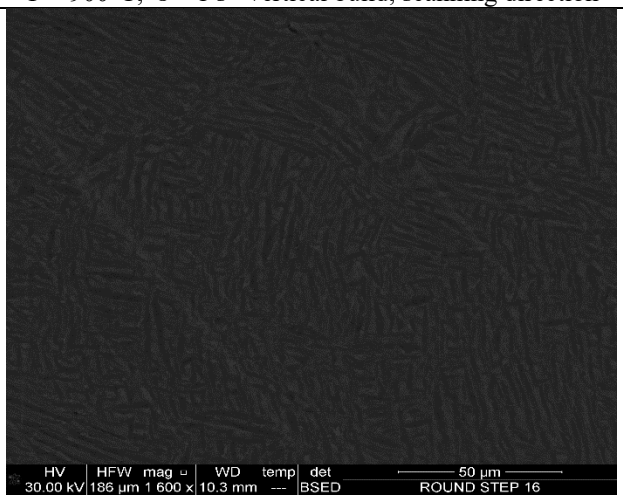

T = 900°C, $\dot{\varepsilon}$ = 0.1 s^{-1} vertical build, building direction

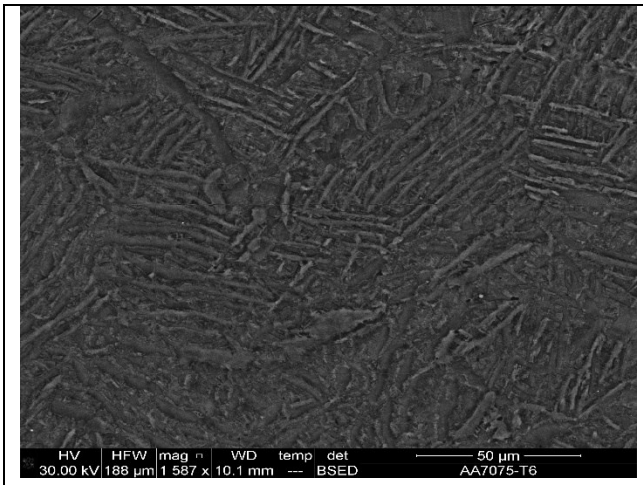	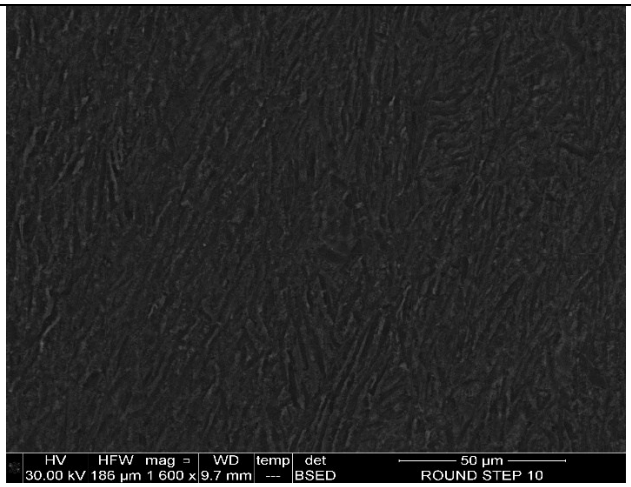
T = 950°C, $\dot{\varepsilon}$ = 10 s^{-1} vertical build, scanning direction	T = 950°C, $\dot{\varepsilon}$ = 10 s^{-1} vertical build, building direction
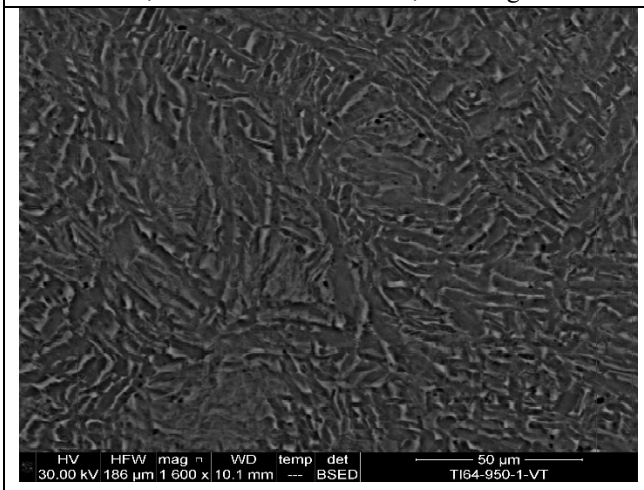	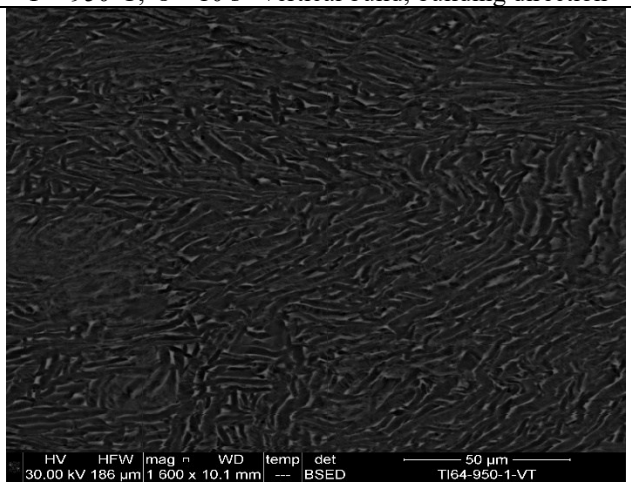
T = 950°C, $\dot{\varepsilon}$ = 1 s^{-1} vertical build, scanning direction	T = 950°C, $\dot{\varepsilon}$ = 1 s^{-1} vertical build, scanning direction
N/A T = 950°C, $\dot{\varepsilon}$ = 0.1 s^{-1} vertical build, scanning direction	**N/A** T = 950°C, $\dot{\varepsilon}$ = 0.1 s^{-1} vertical build, building direction

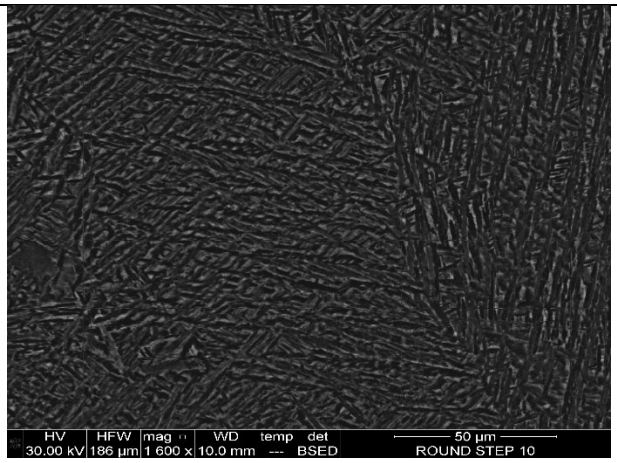

T = 800°C, $\dot{\varepsilon}$ = 10 s^{-1} horizontal build, building direction

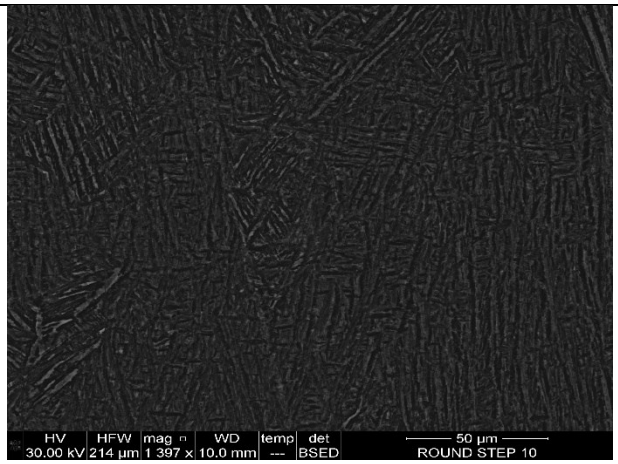

T = 800°C, $\dot{\varepsilon}$ = 10 s^{-1} scanning build, scanning direction

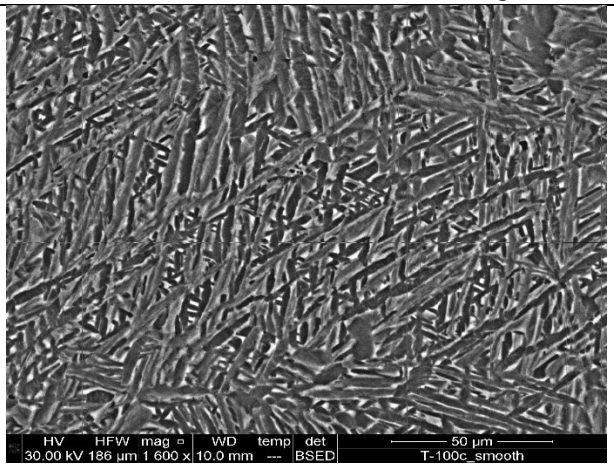

T = 800°C, $\dot{\varepsilon}$ = 1 s^{-1} horizontal build, building direction

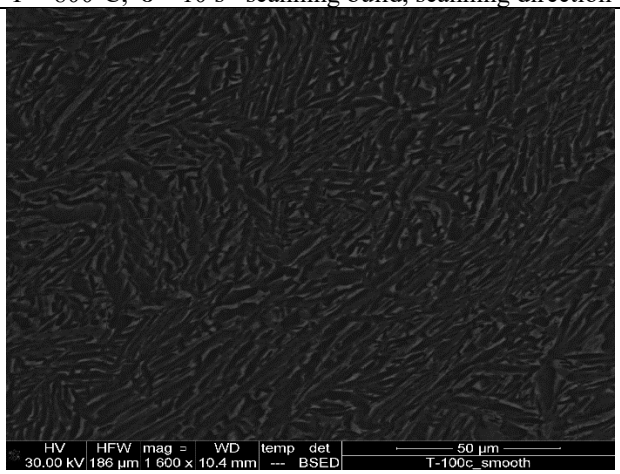

T = 800°C, $\dot{\varepsilon}$ = 1 s^{-1} horizontal build, scanning direction

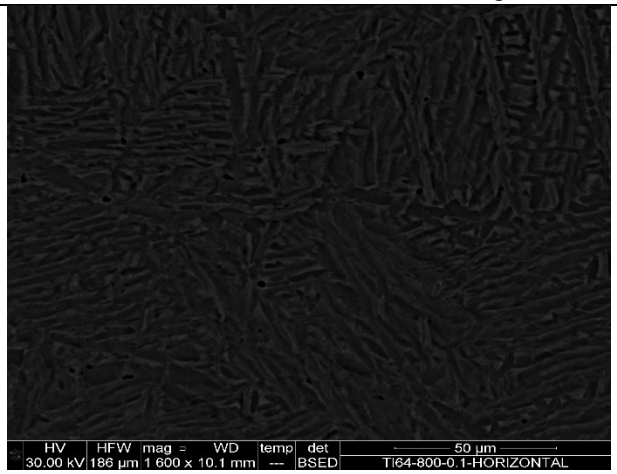

T = 800°C, $\dot{\varepsilon}$ = 0.1 s^{-1} horizontal build, building direction

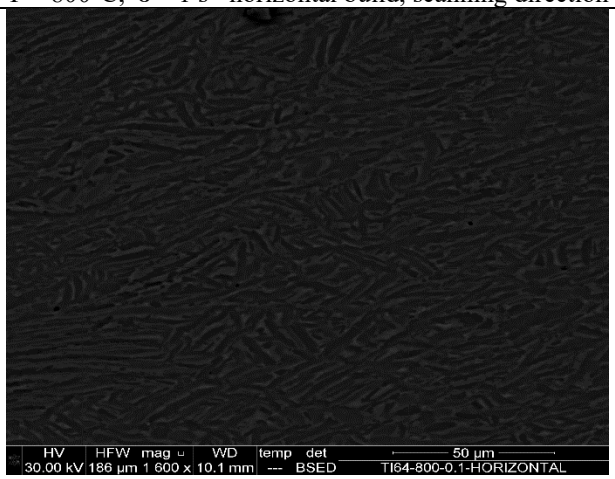

T = 800°C, $\dot{\varepsilon}$ = 0.1 s^{-1} horizontal build, scanning direction

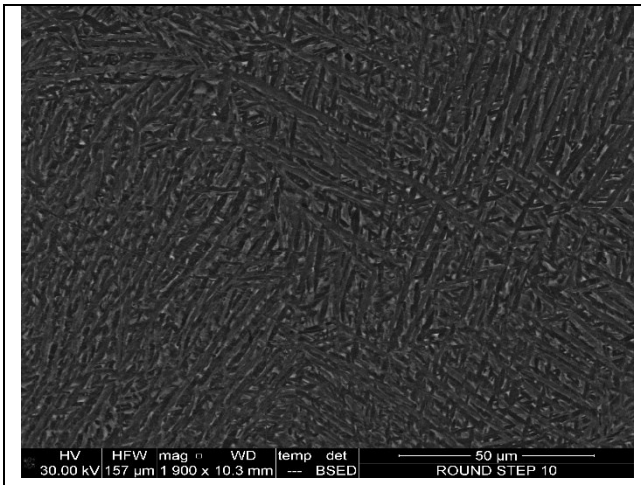

T = 900°C, $\dot{\varepsilon}$ = 10 s^{-1} horizontal build, building direction

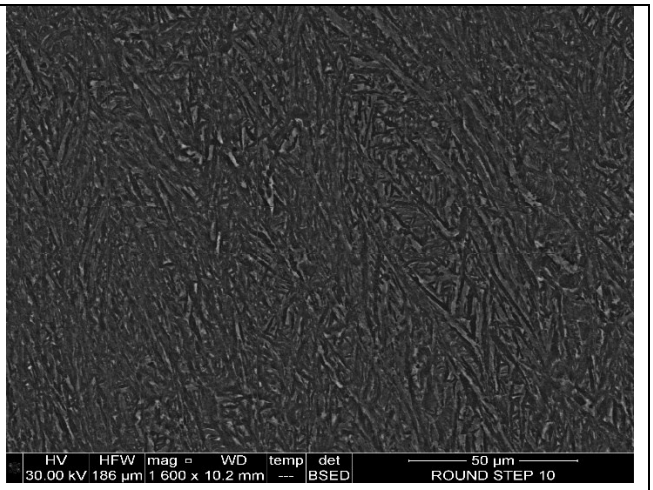

T = 900°C, $\dot{\varepsilon}$ = 10 s^{-1} horizontal build, scanning direction

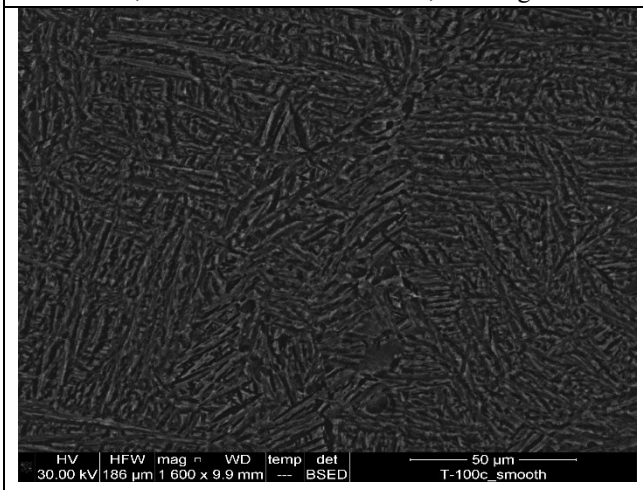

T = 900°C, $\dot{\varepsilon}$ = 1 s^{-1} horizontal build, building direction

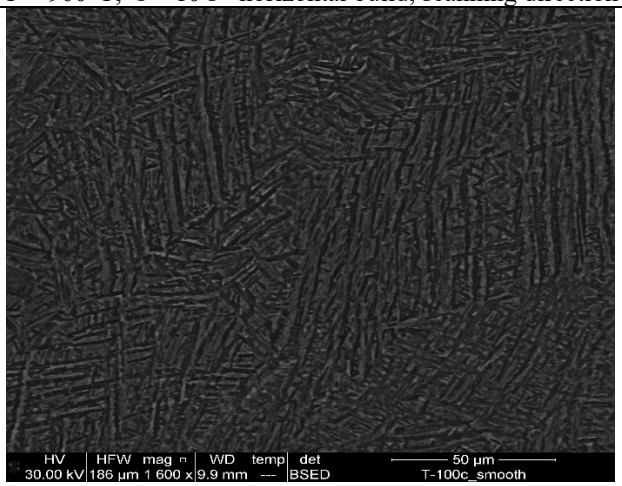

T = 900°C, $\dot{\varepsilon}$ = 1 s^{-1} horizontal build, scanning direction

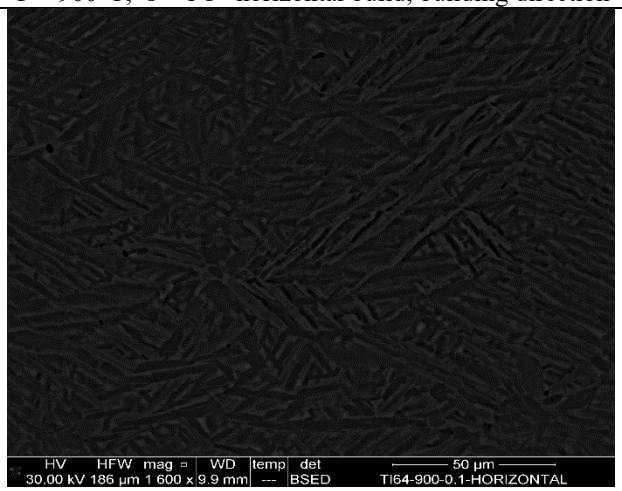

T = 900°C, $\dot{\varepsilon}$ = 0.1 s^{-1} horizontal build, building direction

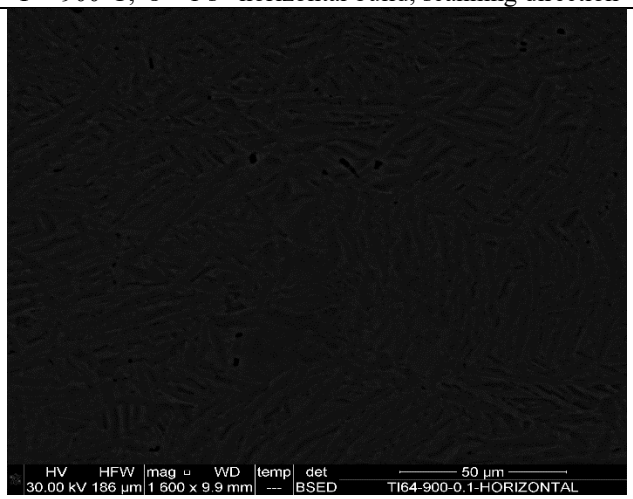

T = 900°C, $\dot{\varepsilon}$ = 0.1 s^{-1} horizontal build, scanning direction

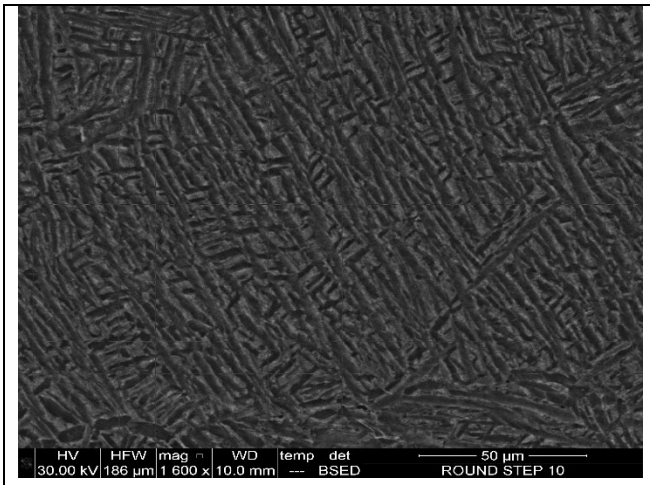

T = 950°C, $\dot{\varepsilon}$ = 10 s^{-1} horizontal build, building direction

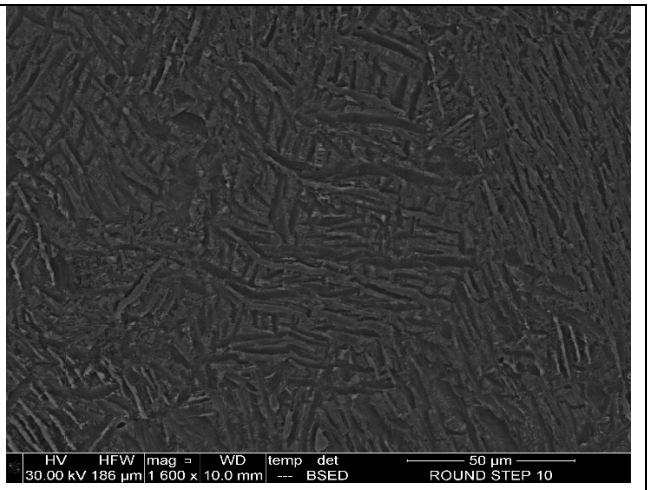

T = 950°C, $\dot{\varepsilon}$ = 10 s^{-1} horizontal build, scanning direction

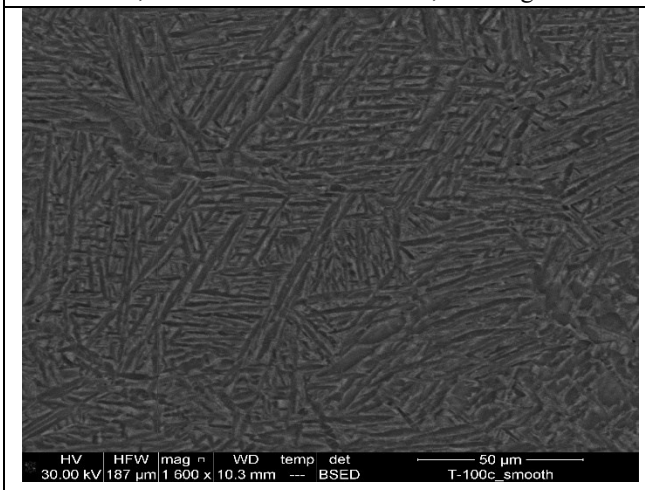

T = 950°C, $\dot{\varepsilon}$ = 1 s^{-1} horizontal build, building direction

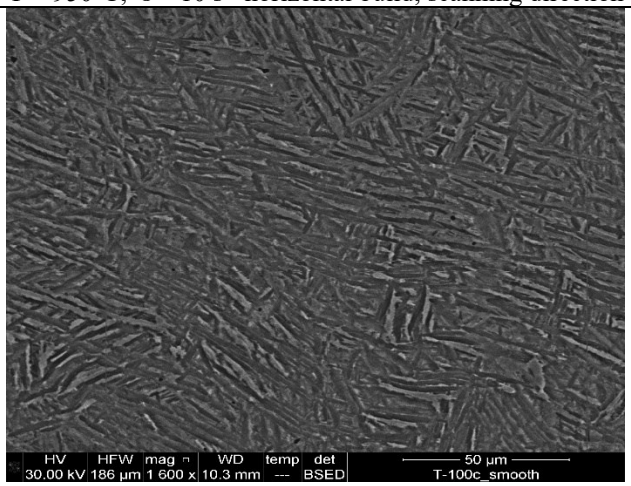

T = 950°C, $\dot{\varepsilon}$ = 1 s^{-1} horizontal build, scanning direction

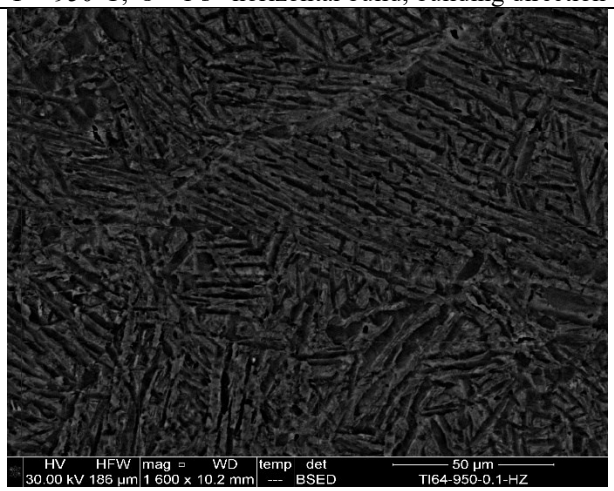

T = 950°C, $\dot{\varepsilon}$ = 0.1 s^{-1} horizontal build, building direction

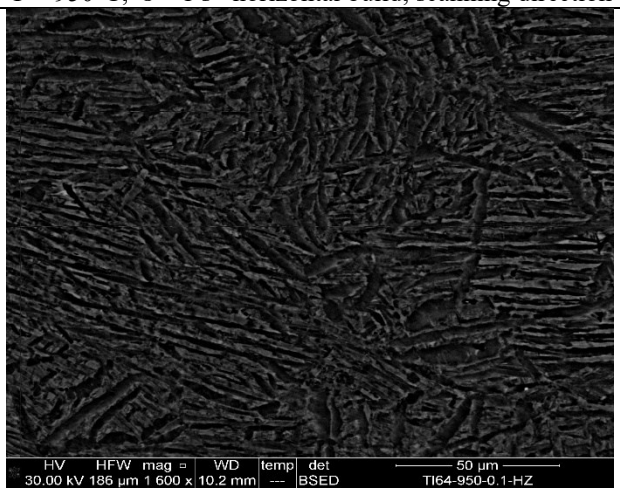

T = 950°C, $\dot{\varepsilon}$ = 0.1 s^{-1} horizontal build, scanning direction

III. Additional plots of α-lath thickness

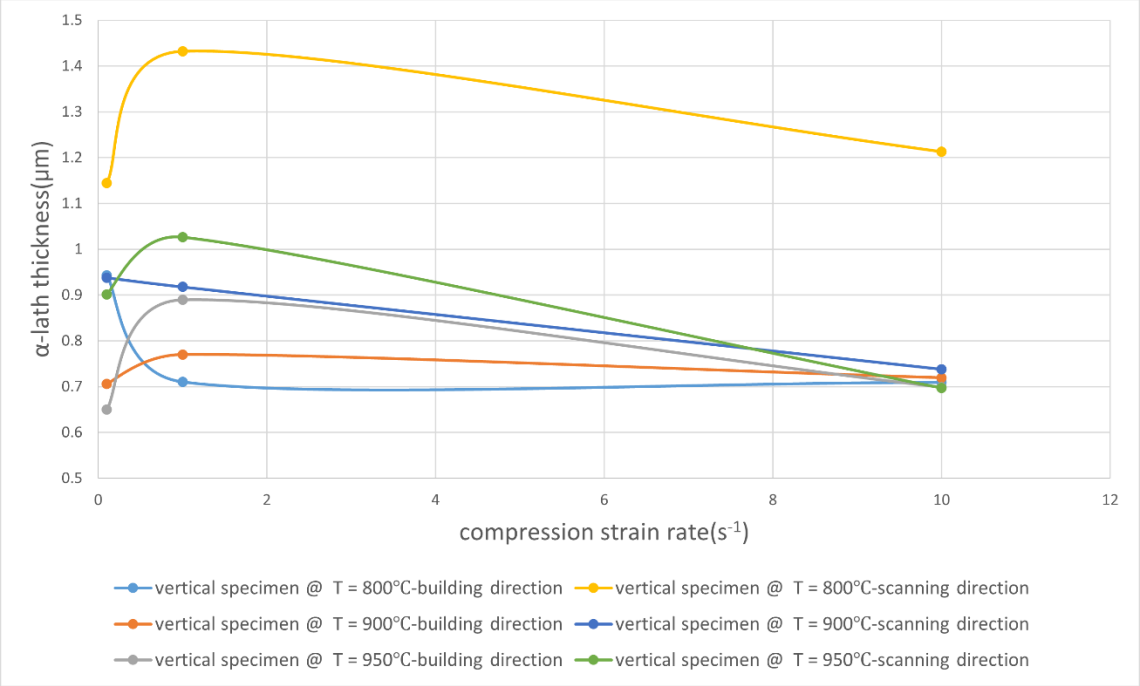

Fig. Variability of α-lath thickness between the vertical build specimens at a constant temperature

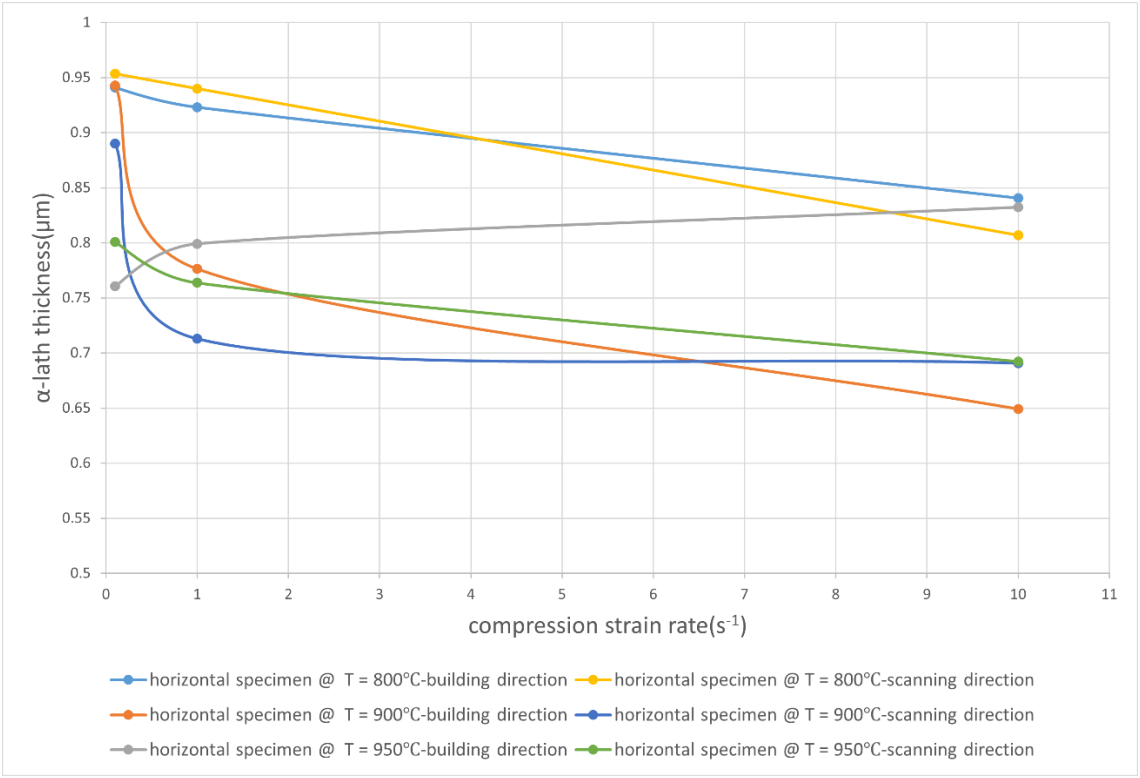

Fig. Variability of α-lath thickness between the horizontal build specimens at a constant temperature

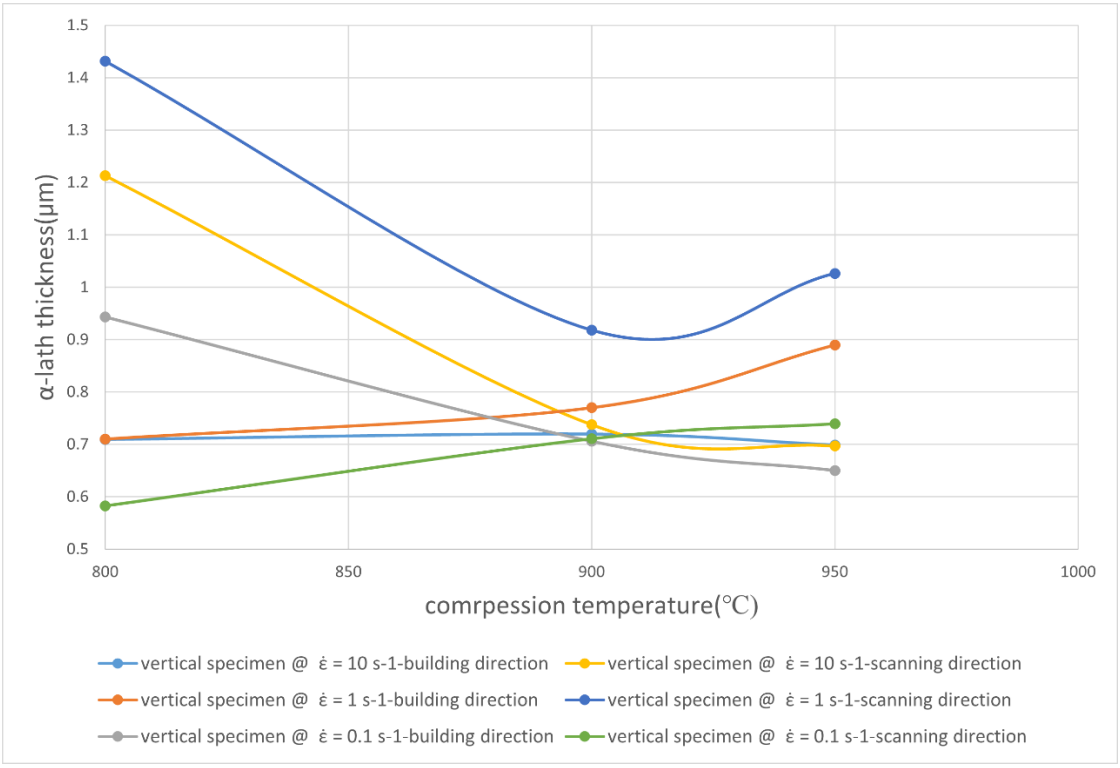

Fig. Variability of α-lath thickness between the vertical build specimens at a constant strain rate

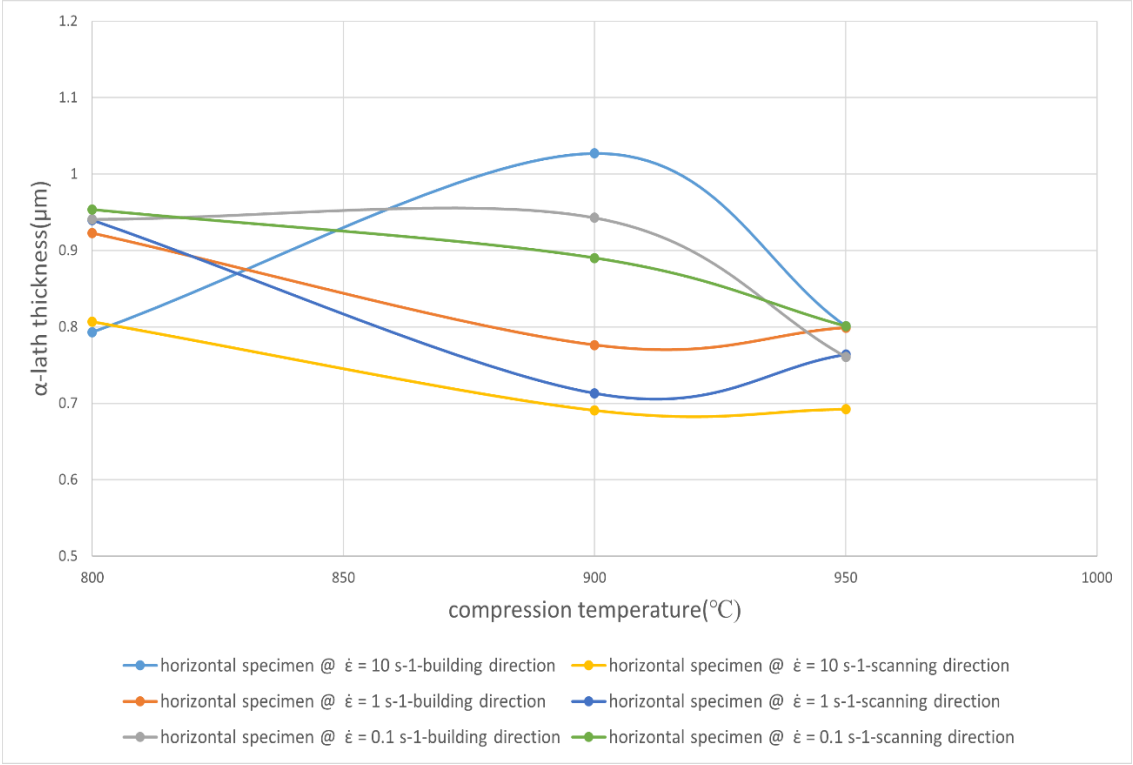

Fig. Variability of α-lath thickness between the horizontal build specimens at a constant strain rate

IV. Modified Arrhenius Model in Python

```
import pandas as pd
import numpy as np
import ast
from scipy.optimize import curve_fit
from sklearn.metrics import r2_score
import matplotlib.pyplot as plt # Import matplotlib for plotting

# Load the data
file_path = '/content/my_ti64_data.csv'
df = pd.read_csv(file_path)

# Convert string representations of lists to actual lists
df['True_Strain'] = df['True_Strain'].apply(ast.literal_eval)
df['True_Stress'] = df['True_Stress'].apply(ast.literal_eval)

# Gas constant in J/(mol*K)
R = 8.314

# Function to extract stress at a specific strain (0.80)
def get_stress_at_strain(strain_list, stress_list, target_strain):
    strain_array = np.array(strain_list)
    stress_array = np.array(stress_list)

    if target_strain < strain_array.min() or target_strain > strain_array.max():
        return np.nan # Or handle appropriately, e.g., extrapolation warning

    return np.interp(target_strain, strain_array, stress_array)

# Extract flow stress at strain 0.80
df['Flow_Stress_at_0_80_Strain'] = df.apply(
    lambda row: get_stress_at_strain(row['True_Strain'], row['True_Stress'], 0.80), axis=1
)

# Convert temperature from Celsius to Kelvin
df['Temp_K'] = df['Temp_C'] + 273.15

# Filter out rows where Flow_Stress_at_0_80_Strain is NaN (if any)
df_filtered = df.dropna(subset=['Flow_Stress_at_0_80_Strain']).copy()

# Define the hyperbolic sine Arrhenius equation function
# X is a tuple/array of (Temperature in Kelvin, Strain_Rate)
# Parameters to be fitted are Q, alpha, n, A
def arrhenius_model(X, Q, alpha, n, A):
    T, strain_rate = X
    T = np.array(T, dtype=float)
```

```
    strain_rate = np.array(strain_rate, dtype=float)

    # Ensure A and alpha are not zero to avoid division by zero or errors
    if A == 0 or alpha == 0:
        # Return a large value to penalize this parameter set during optimization
        return np.inf * np.ones_like(T)

    try:
        # Calculate Zener-Hollomon parameter (Z)
        Z = strain_rate * np.exp(Q / (R * T))

        # Calculate the argument for asinh
        # (Z / A) should be positive for real results from (Z/A)^(1/n)
        arg_asinh = (Z / A)**(1/n)

        # Calculate stress
        sigma = (1 / alpha) * np.arcsinh(arg_asinh)
        return sigma
    except Exception as e:
        # Catch any numerical errors (e.g., overflow) and return inf
        return np.inf * np.ones_like(T)

# Prepare data for curve_fit
X_data = np.array([df_filtered['Temp_K'].values, df_filtered['Strain_Rate'].values])
y_data = df_filtered['Flow_Stress_at_0_80_Strain'].values

# Initial guesses for the parameters [Q, alpha, n, A]
# These initial guesses are critical for successful convergence of curve_fit.
# Based on typical values for metallic alloys.
initial_guesses = [300000, 0.02, 5, 1e15]

# Bounds for the parameters [Q_min, alpha_min, n_min, A_min], [Q_max, alpha_max, n_max,
A_max]
# Setting reasonable bounds helps guide the optimization and prevent unphysical results.
bounds = ([100000, 0.001, 1, 1e5], [600000, 1.0, 20, 1e30])

try:
    # Perform the curve fitting
    # maxfev increased to allow more iterations for convergence
    popt, pcov = curve_fit(arrhenius_model, X_data, y_data, p0=initial_guesses, bounds=bounds,
maxfev=100000)

    # Extract optimized parameters
    Q_opt, alpha_opt, n_opt, A_opt = popt

    print(f"Optimized Parameters:")
    print(f"Q (Activation Energy): {Q_opt:.2f} J/mol")
```

```
    print(f"alpha: {alpha_opt:.6f} MPa^-1")
    print(f"n (Stress Exponent): {n_opt:.4f}")
    print(f"A (Material Constant): {A_opt:.2e} s^-1")

    # Predict flow stress using the optimized parameters
    y_predicted = arrhenius_model(X_data, Q_opt, alpha_opt, n_opt, A_opt)

    # Calculate R-squared
    r_squared = r2_score(y_data, y_predicted)
    print(f"\nOverall R-squared of the predicted vs actual flow stresses at strain 0.80: {r_squared:.4f}")

    # Create a DataFrame to save the results
    df_results = pd.DataFrame({
        'Actual_Flow_Stress_at_0_80_Strain': y_data,
        'Predicted_Flow_Stress_at_0_80_Strain': y_predicted,
        'Temp_C': df_filtered['Temp_C'],
        'Strain_Rate': df_filtered['Strain_Rate']
    })
    # Save the results to a CSV file
    df_results.to_csv('nonlinear_regression_results.csv', index=False)
    print("\nResults saved to 'nonlinear_regression_results.csv'")

except RuntimeError as e:
    print(f"Error during curve fitting: {e}")
    print("This often means the optimization algorithm could not find a good fit.")
    print("Consider adjusting initial guesses, bounds, or checking the data for suitability.")
except ValueError as e:
    print(f"Value Error during curve fitting: {e}")
    print("This typically indicates issues with input values (e.g., `inf` or `NaN` values, or incompatible shapes).")
    print("Ensure your data is clean and your initial guesses/bounds are reasonable.")

# Store the optimized parameters in a dictionary, separated by orientation if needed
# For this model fit on combined data, we'll store them as a single set
material_models = {
    'Overall': {
        'A': A_opt,
        'alpha': alpha_opt,
        'n': n_opt,
        'Q': Q_opt
    }
}

# Define the fixed strain used for parameter determination
fixed_true_strain = 0.80
```

```
# --- 6. Prediction of Flow Stress ---

def predict_flow_stress(strain_rate, temp_c, orientation, material_models_dict):
    """
    Predicts flow stress using the fixed-strain modified Arrhenius model.
    Note: 'strain' is implicitly fixed at `fixed_true_strain` for parameter determination.

    Args:
        strain_rate (float): Strain rate (s^-1).
        temp_c (float): Temperature in Celsius.
        orientation (str): Build orientation ('Vertical' or 'Horizontal').
        material_models_dict (dict): Dictionary containing the determined material constants.

    Returns:
        float: Predicted flow stress (MPa).
        None: If parameters for the given orientation are not available or invalid.
    """
    temp_k = temp_c + 273.15
    # For this model, we are using overall parameters, ignoring orientation in prediction
    model_params = material_models_dict.get('Overall')

    if model_params is None or any(v is None or np.isnan(v) for v in model_params.values()):
        return np.nan # Return NaN for invalid predictions

    A_val = model_params['A']
    alpha_val = model_params['alpha']
    n_val = model_params['n']
    Q_val = model_params['Q']

    # Ensure valid inputs for arsinh calculation (no division by zero or log of zero)
    if not all(isinstance(val, (int, float)) and np.isfinite(val) for val in [A_val, alpha_val, n_val,
Q_val]):
        return np.nan

    # Critical check: alpha and n must be positive for the model to be physically meaningful
    if A_val <= 0 or n_val <= 0 or alpha_val <= 0:
        # print(f"Warning: Calculated parameter is non-positive for {orientation}. A={A_val},
alpha={alpha_val}, n={n_val}")
        return np.nan

    try:
        Z_over_A = strain_rate / (A_val * np.exp(-Q_val / (R * temp_k)))
        arg_arsinh = Z_over_A**(1/n_val)
        predicted_sigma = (1 / alpha_val) * np.arcsinh(arg_arsinh)
        return predicted_sigma
    except Exception as e:
        # print(f"Prediction error for {orientation} at SR {strain_rate}, T {temp_c}: {e}")
```

```
        return np.nan

# --- 7. Validate and Visualize Predictions ---

print("\n--- Validating Model Predictions ---")
predicted_stresses_at_fixed_strain = []
actual_stresses_at_fixed_strain = []

# Use df_filtered instead of df_extracted
for index, row in df_filtered.iterrows():
    actual_stress = row['Flow_Stress_at_0_80_Strain'] # Use the extracted flow stress
    strain_rate = row['Strain_Rate']
    temp_c = row['Temp_C']
    orientation = row['Orientation']

    pred_stress = predict_flow_stress(strain_rate, temp_c, orientation, material_models)
    if not np.isnan(pred_stress):
        predicted_stresses_at_fixed_strain.append(pred_stress)
        actual_stresses_at_fixed_strain.append(actual_stress)

# Convert to numpy arrays for calculations
predicted_stresses_at_fixed_strain = np.array(predicted_stresses_at_fixed_strain)
actual_stresses_at_fixed_strain = np.array(actual_stresses_at_fixed_strain)

if len(actual_stresses_at_fixed_strain) > 1:
    r2 = r2_score(actual_stresses_at_fixed_strain, predicted_stresses_at_fixed_strain)
    print(f"\nOverall R-squared of the predicted vs actual flow stresses at strain {fixed_true_strain:.2f}: {r2:.4f}")

    # Plotting Predicted vs Actual Flow Stress
    plt.figure(figsize=(8, 6))
    plt.scatter(actual_stresses_at_fixed_strain, predicted_stresses_at_fixed_strain, alpha=0.6)

    # Ensure there's a range for plotting the ideal fit line
    if len(actual_stresses_at_fixed_strain) > 0:
        min_val = min(actual_stresses_at_fixed_strain.min(), predicted_stresses_at_fixed_strain.min())
        max_val = max(actual_stresses_at_fixed_strain.max(), predicted_stresses_at_fixed_strain.max())
        plt.plot([min_val, max_val], [min_val, max_val], 'r--', label='Ideal Fit (y=x)')

    plt.xlabel(f"Actual Flow Stress (MPa) at Strain {fixed_true_strain:.2f}")
    plt.ylabel(f"Predicted Flow Stress (MPa) at Strain {fixed_true_strain:.2f}")
    plt.title(f"Predicted vs Actual Flow Stress (R² = {r2:.4f})")
    plt.grid(True)
    plt.legend()
    plt.show()
```

```
else:
   print("\nNot enough valid data points to calculate R-squared or plot predicted vs actual stresses.")


# Plotting specific stress-strain curves: Actual vs Predicted (full curves)
print("\n--- Plotting Actual vs Predicted Full Stress-Strain Curves ---")
print("Note: Predictions for the full curve use constants determined at the FIXED_TRUE_STRAIN value.")
print("This is for visualization, not a full strain-compensated model across varying strains.")

# Use the original df for plotting full curves, as it contains all strain-stress data
df_exp = df.copy() # Use df_exp for plotting as it was used in the original code

for orientation in ['Vertical', 'Horizontal']:
   plt.figure(figsize=(15, 10))
   plt.suptitle(f'Actual vs Predicted Flow Stress for {orientation} Orientation (Constants from ε={fixed_true_strain:.2f})', fontsize=16)

   sub_df_orientation = df_exp[df_exp['Orientation'] == orientation]
   unique_temps = np.sort(sub_df_orientation['Temp_C'].unique())
   unique_srs = np.sort(sub_df_orientation['Strain_Rate'].unique())

   plot_idx = 1
   for temp_c in unique_temps:
      for sr in unique_srs:
         # Calculate the number of rows and columns needed for subplots
         num_rows = len(unique_temps)
         num_cols = len(unique_srs)

         ax = plt.subplot(num_rows, num_cols, plot_idx)

         # Find actual data for this condition
         actual_data_row = sub_df_orientation[
            (sub_df_orientation['Temp_C'] == temp_c) &
            (sub_df_orientation['Strain_Rate'] == sr)
         ]
         if not actual_data_row.empty:
            true_strain_actual = actual_data_row.iloc[0]['True_Strain']
            true_stress_actual = actual_data_row.iloc[0]['True_Stress']
            ax.plot(true_strain_actual, true_stress_actual, 'k-', label='Actual')

            # Predict stress for the same strain range using the fixed constants
            # We iterate through the actual strain points to get predictions for the curve
            predicted_stresses_curve = [predict_flow_stress(sr, temp_c, orientation, material_models)
```

```
                for s in true_strain_actual] # 's' is not used in predict_flow_stress, it's fixed
            ax.plot(true_strain_actual, predicted_stresses_curve, 'r--', label='Predicted (Fixed ε={:.2f})'.format(fixed_true_strain))

            ax.set_title(f'T={temp_c}°C, SR={sr}s⁻¹')
            ax.set_xlabel('True Strain')
            ax.set_ylabel('True Stress (MPa)')
            ax.legend()
            ax.grid(True)
            plot_idx += 1
    plt.tight_layout(rect=[0, 0.03, 1, 0.95]) # Adjust layout to prevent title overlap
    plt.show()
```

Additional plots from Modified Arrhenius Model

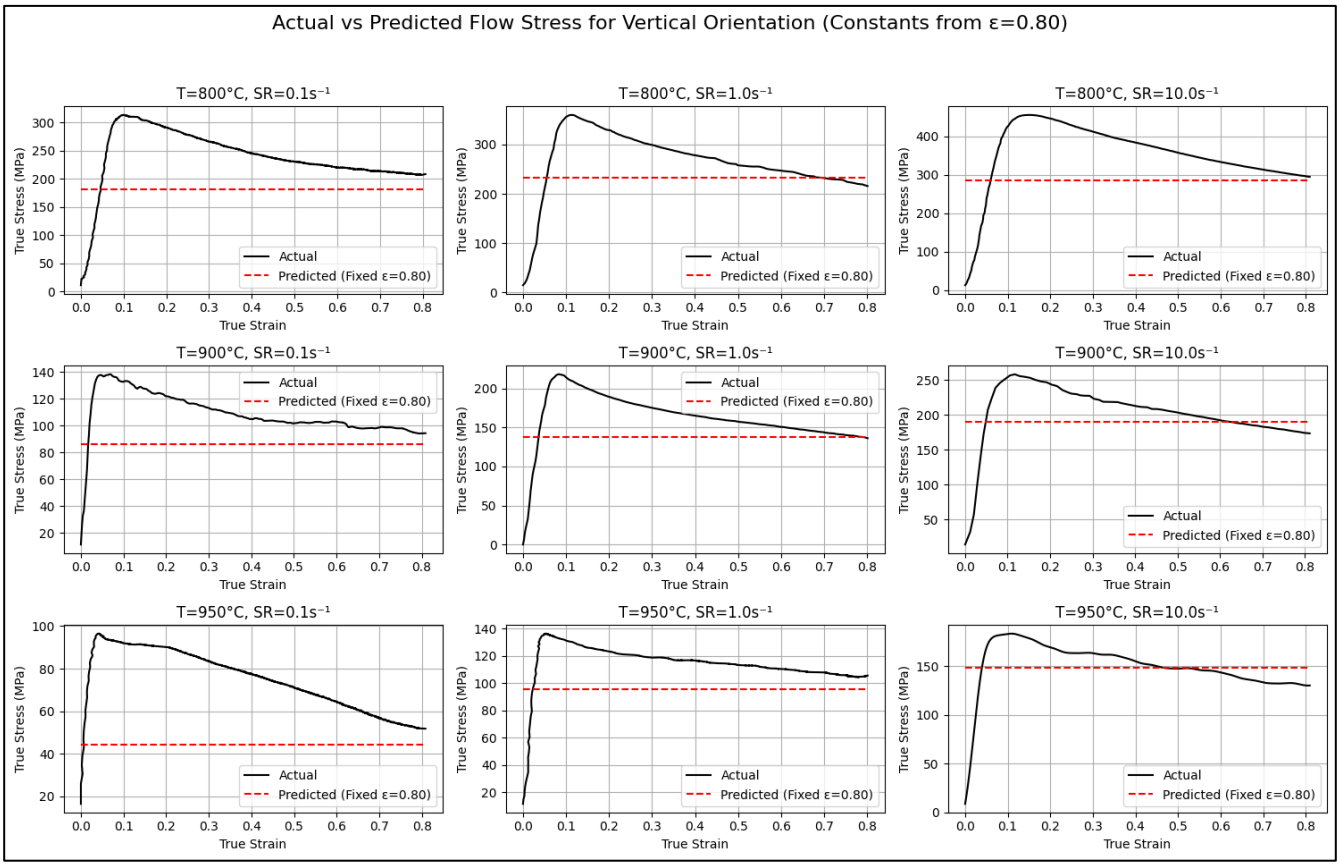

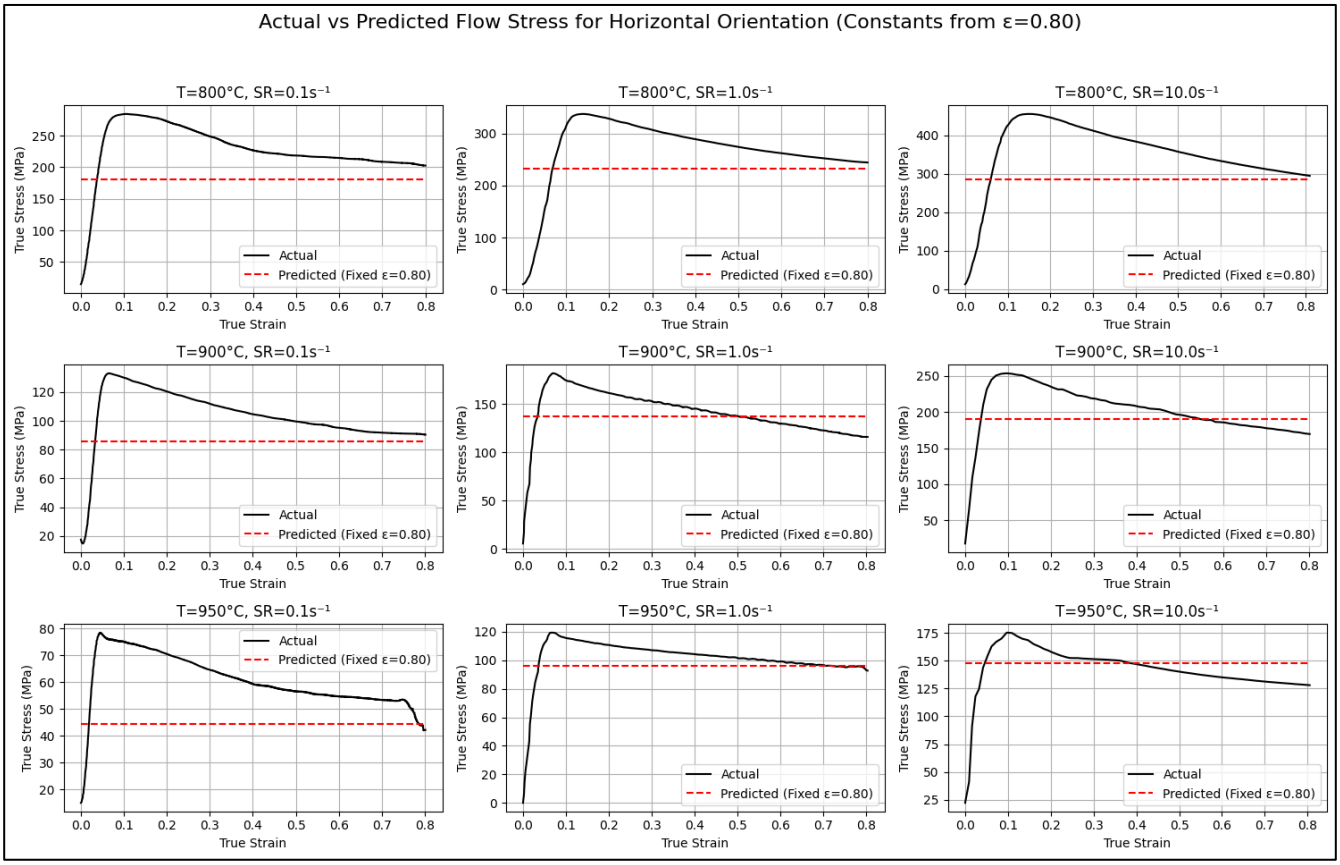

V. Microstructure quantification data with STD

Temperature	Strain rate	Alpha lath thickness	Standard Deviation	Build type	Viewing direction
800	10	1.678	0.438	Vertical	Building direction
900	10	1.699	0.530	Vertical	Building direction
950	10	1.451	0.357	Vertical	Building direction
800	1	2.214	0.437	Vertical	Building direction
900	1	1.875	0.667	Vertical	Building direction
950	1	1.654	0.386	Vertical	Building direction
800	0.1	2.21	0.543	Vertical	Building direction
900	0.1	1.658	0.379	Vertical	Building direction
950	0.1	1.504	0.438	Vertical	Building direction
800	10	1.585	0.406	Horizontal	Building direction
900	10	1.519	0.400	Horizontal	Building direction
950	10	1.811	0.610	Horizontal	Building direction
800	1	2.169	0.656	Horizontal	Building direction
900	1	1.805	0.451	Horizontal	Building direction
950	1	1.86	0.736	Horizontal	Building direction
800	0.1	2.232	0.643	Horizontal	Building direction
900	0.1	1.948	0.495	Horizontal	Building direction
950	0.1	1.892	0.641	Horizontal	Building direction

Table: Data obtained from ImageJ

Temperature	*Strain rate*	*α-lath thickness*	*Standard Deviations*	*Build type*	*Viewing direction*
800	*10*	*0.709437218*	*1.231874433*	*Vertical*	*Building direction*
900	*10*	*0.719601255*	*0.581440069*	*Vertical*	*Building direction*
950	*10*	*0.698799567*	*0.862568703*	*Vertical*	*Building direction*
800	*1*	*0.710529046*	*1.421262628*	*Vertical*	*Building direction*
900	*1*	*0.770281018*	*0.963570884*	*Vertical*	*Building direction*
950	*1*	*0.889719294*	*0.894104932*	*Vertical*	*Building direction*
800	*0.1*	*0.943042141*	*0.936578937*	*Vertical*	*Building direction*
900	*0.1*	*0.706029955*	*0.827677812*	*Vertical*	*Building direction*
950	*0.1*	*0.650164833*	*0.534346287*	*Vertical*	*Building direction*
800	*10*	*0.84043395*	*0.710371153*	*Horizontal*	*Building direction*
900	*10*	*0.649208161*	*0.727790859*	*Horizontal*	*Building direction*
950	*10*	*0.8322005*	*0.937215158*	*Horizontal*	*Building direction*
800	*1*	*0.922834431*	*1.006160485*	*Horizontal*	*Building direction*
900	*1*	*0.776234494*	*0.838062057*	*Horizontal*	*Building direction*
950	*1*	*0.798991673*	*0.862381595*	*Horizontal*	*Building direction*
800	*0.1*	*0.940720055*	*1.185469708*	*Horizontal*	*Building direction*
900	*0.1*	*0.942752753*	*1.307554168*	*Horizontal*	*Building direction*
950	*0.1*	*0.760528857*	*0.921986114*	*Horizontal*	*Building direction*

Table: Data obtained from MIPAR